Characterisation of cycling tumour hypoxia with magnetic resonance imaging

Miguel Rodrigues Gonçalves

Submitted for the degree of Doctor of Philosophy in Biophysics

Centre for Advanced Biomedical Imaging (CABI), Division of Medicine

and

Cancer Institute

University College London

Declaration

I, Miguel Rodrigues Gonçalves, confirm that the work presented in this thesis is my own. Where information has been derived from other sources, I confirm that this has been indicated in the thesis. This work is based on research which has been conducted by me during the period of September 2011 to December 2014 at University College London.

Miguel Rodrigues Gonçalves

4th February 2016

Abstract

Hypoxia is defined by a low oxygen concentration state in biological tissue, resulting from an imbalance between oxygen supply and demand. Greater understanding of hypoxia in tumours is essential, as it is associated with disease progression and resistance to therapy, leading therefore to a poorer prognosis. Tumour hypoxia can be classified into two types: chronic and cycling, and this thesis focuses on characterising cycling hypoxia in colorectal carcinoma tumours in mice. For that, magnetic resonance imaging (MRI) was used, as it provides a non-invasive method to dynamically map blood oxygenation changes due to the different magnetic properties of oxygenated and deoxygenated blood.

The first approach to characterise cycling tumour hypoxia consisted of a longitudinal study in which the influence of the tumour size on the occurrence, frequency and amplitude of cycling events was investigated. These observations were complemented with tumour vascular properties, inferred from applied vasoactive gas challenges, with blood sampling assessments, and with histological assessments.

The influence of systemic variations in blood oxygenation in cycling tumour hypoxia was demonstrated through simultaneous acquisition of MRI and blood oxygen saturation trends. In particular, the computational implementation of independent component analysis (ICA) allowed the identification of the tumour regions that were simultaneously suffering from systemic and tumour-specific effects, and revealed links to tumour pathophysiology.

The effect of a therapy on cycling tumour hypoxia was also assessed under the hypothesis of a "vascular normalisation" effect of the drug. In addition, the effects of the therapy on gas challenge response and on histological distributions were studied.

This dynamic MRI technique and the ICA protocol were ultimately adapted to a translational study, where cycling hypoxia was investigated as a biomarker for early detection of prostate tumours.

Overall, this thesis revealed that the stage of the tumour development can influence some aspects related to cycling hypoxia, and that its occurrence has a contribution of local and systemic effects. Also, it drew attention to the regional effects a therapy can have in tumours and provided a starting point to assess cycling tumour hypoxia in the clinic.

Acknowledgments

In first place, I would like to thank my primary supervisor, Dr. Simon Walker-Samuel, for his easy-going spirit whilst guiding me in such interesting directions throughout my PhD. I am also indebted to my supervisors, Professors R. Barbara Pedley and Mark F. Lythgoe, for their continued help and support, and to all for promoting my development as a scientist.

To past and current friends and colleagues at CABI and the Cancer Institute, for the interesting discussions, the willingness to help and the good times spent outside of work. Of these, I would like to especially thank Dr. Sean Peter Johnson, for teaching me the techniques of cell culture, injections, and histology, and Dr. Jack Wells, for introducing me to statistical parametric mapping, which were fundamental in this thesis.

To my friends in Portugal, Serbia, UK and scattered around Europe, who always make my time more enjoyable and, in their own way, contributed to the completion of this thesis. A very especial thanks to my capoeira friends, with whom I shared so many experiences and so much happiness, your presence had a huge positive impact during the time I spent in London.

To my family, who always gave me so much love and support. Although far away, you are the strongest foundation.

Publications, presentations, awards and grants arising from research involved in this thesis

Publications

Gonçalves MR, Johnson SP, Ramasawmy R, Pedley RB, Lythgoe MF, Walker-Samuel S. Decomposition of spontaneous fluctuations in tumour oxygenation using BOLD MRI and independent component analysis. *British Journal of Cancer* 2015; **113:** 1168-77

Oral presentations

Assessment of the response of colorectal tumours to imatinib mesylate therapy using carbogen and hypercapnia gas challenges. Joint Annual Meeting ISMRM-ESMRMB, Milan, Italy, 2014

Investigating tumour vascular connectivity with resting state MRI and independent component analysis (or variants thereof)

22nd British Chapter ISMRM Postgraduate Symposium, London, UK, 2013

20th ISMRM Annual Meeting & Exhibition, Melbourne, Australia, 2012

21st British Chapter ISMRM Postgraduate Symposium, Bristol, UK, 2012

Poster presentations

Investigating systemic and tumour-specific fluctuations in tumour R_2* measurement with independent component analysis and pulse oximetry (or variants thereof)

21st ISMRM Annual Meeting & Exhibition, Salt Lake City, USA, 2013

EACR-22 (The European Association for Cancer Research), Barcelona, Spain, 2012

Awards and grants

Magna Cum Laude Merit Award, Joint Annual Meeting ISMRM-ESMRMB, Milan, 2014 (top 15**%** abstracts)

Student Conference Funding, British Association for Cancer Research, 2013 (£720)

Summa Cum Laude Merit Award, 20th ISMRM Annual Meeting & Exhibition, Melbourne, 2012 (top 3% abstracts)

3-year Grand Challenges Scheme PhD Scholarship, University College London (£18000 p.a.)

Table of contents

Declaration 2
Abstract 3
Acknowledgments 4
Publications, presentations, awards and grants arising from research involved in this thesis 5
List of figures 10
List of tables 13
Acronyms and abbreviations 14
Introduction to the layout of contents 17
1. Introduction 18
1.1. Structural differences between tumour and normal tissues 18
1.2. Tumour hypoxia: chronic and cycling 19
1.2.1. Chronic hypoxia 19
1.2.2. Cycling hypoxia 20
1.2.3. Spatiotemporal characteristics of cycling hypoxia 22
1.3. Biological effects of tumour hypoxia 22
1.3.1. Tumour hypoxia is a source of treatment resistance 22
1.3.2. Tumour hypoxia promotes metastatic disease and tumour proliferation 23
1.3.3. The role of HIF-1 in tumour adaptation to hypoxia 24
1.4. Relative biological effects of chronic and cycling hypoxia 25
1.4.1. Cycling hypoxia and glycolysis 26
1.5. Methods to detect cycling hypoxia in tumours 27
1.6. Motivation and aim of this thesis 30
2. Magnetic resonance imaging 31
2.1. Basic principles of MRI 31
2.1.1. Angular momentum, magnetic moment and the hydrogen nucleus 31
2.1.2. Zeeman Effect, Boltzmann distribution and the Larmor frequency 32
2.1.3. Equilibrium magnetisation and the $B1$ magnetic field 33
2.1.4. Relaxation 35
2.1.5. Image formation 38
2.1.6. Basic MRI sequences: spin-echo and gradient-echo 39
2.2. Gradient-echo MRI as a method of detecting variations in blood flow and oxygenation 44

2.2.1. Assessment of cycling tumour hypoxia with gradient-echo MRI 45
3. Experimental protocols and image analysis 47
3.1. Xenografts 47
3.2. Cell culture and mouse model 47
3.3. *In vivo* MRI 48
3.3.1. Experimental setting 48
3.3.2. Imaging protocol 49
3.4. MRI data analysis 49
3.4.1. Relaxometry estimation and calculation of resting state and gas challenge maps 50
3.4.2. Noise estimation in resting state maps 51
3.4.3. Correction of gas challenge maps 52
3.5. Histology and immunostaining 53
3.5.1. Dye administration and sectioning 53
3.5.2. Immunostaining 53
4. Characterisation of spontaneous temporal fluctuations in tumour $R2*$ and relationship with gas challenge responsiveness.....55
4.1. Introduction 55
4.2. Materials and methods 56
4.2.1. Cell culture and imaging protocol 56
4.2.2. Analysis of resting state maps 56
4.2.3. Analysis of gas challenge maps 58
4.2.4. Relationship between resting state and gas challenge maps 59
4.2.5. Histological assessment 59
4.2.6. Analysis of oxygenation and pH of systemic blood 60
4.3. Results 60
4.3.1. Spontaneous fluctuations at rest 60
4.3.2. Response to hyperoxia challenges 67
4.3.3. Response to hypercapnia challenge 71
4.3.4. Relationship between spontaneous fluctuations and gas challenge responsiveness 73
4.3.5. Histological markers and their relationship with spontaneous fluctuations 75
4.3.6. Oxygenation and pH of systemic blood 78

4.4. Discussion 80
4.4.1. Detection of spontaneous fluctuations at rest 80
4.4.2. Tumour response to hyperoxia 82
4.4.3. Tumour response to hypercapnia 85
4.4.4. Spontaneous fluctuations *versus* gas challenge responsiveness 85
4.4.5. Influence of blood pH on $R2*$ measurements 86
4.5. Conclusions 87
5. Influence of systemic variations on cycling hypoxia patterns in tumours 89
5.1. Introduction 89
5.2. Materials and methods 90
5.2.1. Animal models and imaging protocol 90
5.2.2. *In vivo* pulse oximetry 90
5.2.3. Tumour MRI data analysis and relationship with systemic blood oxygenation 91
5.2.4. Frequency analysis of thresholded $R2*$ maps and O_2sat curves 95
5.2.5. Histological assessment and whole-tumour statistical relationships 95
5.3. Results 96
5.3.1. Relationships between sources of $R2*$ oscillation and between tumour lines 96
5.3.2. Physiological basis of tumour fluctuations 102
5.4. Discussion 104
5.4.1. Discrimination between the sources of $R2*$ fluctuation in tumours and between tumour types 104
5.4.2. Relationships between $R2*$ fluctuations and pathophysiological measurements in tumours 106
5.4.3. Limitations of the method 107
5.5. Conclusions 108
6. Effect of imatinib therapy on $R2*$ spontaneous fluctuations and gas challenge responsiveness in tumours .. 109
6.1. Introduction 109
6.2. Materials and methods 110
6.2.1. Animal models and *in vivo* MRI 110
6.2.2. Therapy protocol 111
6.2.3. MRI data analysis 111

6.2.4. Histological assessment 114
6.2.5. Statistical analysis 114
6.3. Results 115
6.3.1. Imatinib therapy did not impact on tumour growth rate or on spontaneous $R2*$ fluctuations 115
6.3.2. Imatinib therapy promoted gas challenge response heterogeneity 116
6.3.3. Imatinib therapy did not normalise the tumour vasculature 120
6.4. Discussion 123
6.4.1. Effect of imatinib therapy on the vascular and cellular characteristics of LS174T tumours 124
6.4.2. Effect of imatinib therapy on spontaneous $R2*$ fluctuations 125
6.4.3. Effect of imatinib therapy on the tumour response to applied gases 126
6.5. Conclusions 127
7. Resting state $R2*$ as a biomarker for prostate tumours: a clinical study 129
7.1. Introduction 129
7.2. Materials and methods 130
7.2.1. Patient cohort 130
7.2.2. MRI imaging protocol 130
7.2.3. MRI data analysis 131
7.3. Results and Discussion 133
8. Conclusions and future directions 136
References 142
Supplementary data 157

List of figures

Figure 2.1 - Microscopic (A) and macroscopic (B) representations of a population of proton magnetic moments, μ, in the presence of a static magnetic field, $B0$ 33

Figure 2.2 - Mechanism of resonance absorption 35

Figure 2.3 – Free induction decay (FID) 38

Figure 2.4 – Spin-echo imaging sequence 42

Figure 2.5 – Spoiled gradient-echo imaging sequence 43

Figure 4.1 – Dynamic $R2*$ estimates, at rest, in an example LS174T tumour xenograft 61

Figure 4.2 – Evolution of the percentage of the tumour volume experiencing $R2*$ fluctuations with the tumour growth 62

Figure 4.3 – Evolution of the mean standard deviation (SD) of $R2*$ fluctuations with the tumour growth 63

Figure 4.4 - Comparison between FFT (magenta) and the Lomb method (blue) in identifying the oscillatory frequencies of a generated signal 63

Figure 4.5 – Frequencies of $R2*$ oscillation at rest for SW1222 and LS174T tumours 65

Figure 4.6 – Frequencies of $R2*$ oscillation at rest for SW1222 (n=5) and LS174T (n=6) tumours during 3-hour long acquisitions 66

Figure 4.7 – Hyperoxia gas challenge in an example LS174T tumour 67

Figure 4.8 – Evolution of the percentage of the tumour volume responsive to carbogen (A) and 100% oxygen (B) gas challenges with the tumour growth 69

Figure 4.9 - Evolution of the magnitude of tumour response ($|\Delta R2*|$) to carbogen (A) and 100% oxygen (B) gas challenges with the tumour growth 70

Figure 4.10 – Hypercapnia gas challenge in an example LS174T tumour 71

Figure 4.11 – Evolution of the percentage of the tumour volume responsive to the hypercapnia challenge with the tumour growth 72

Figure 4.12 - Evolution of the magnitude of tumour response (|ΔSI|) to the hypercapnia challenge with the tumour growth 72

Figure 4.13 – Voxel-wise correlation between resting state $R2*$ standard deviation (SD) and carbogen $\Delta R2*$, at day 0, in SW1222 (left) and LS174T (right) tumours 73

Figure 4.14 – Quantitative fluorescence histology in SW1222 (n = 5) and LS174T (n = 4) tumour xenografts 76

Figure 4.15 – Histology in example SW1222 and LS174T tumour xenografts and comparison with MRI data 77

Figure 4.16 – Blood gas analysis and pulse oximetry 79

Figure 5.1 – Schematic diagram of the systemic influence on the tumour oxygenation. 91

Figure 5.2 – Data acquisition and post-processing for the direct correlation approach and the ICA approach 94

Figure 5.3 - Systemic and tumour-specific influences on tumour $R2*$ spontaneous fluctuations in an example SW1222 tumour, following the direct correlation or the ICA approach 97

Figure 5.4 – Relative influence of systemic (Sys) and tumour-specific (T-sp) fluctuations in SW1222 and LS174T tumours, following the direct correlation or the ICA approach 98

Figure 5.5 – Spatial distribution of high amplitude systemic $R2*$ fluctuations, following the direct correlation ($R2\ sys*$) or the ICA approach ($R2\ ICA\ sys*$) 99

Figure 5.6 – Frequency analysis of tumour $R2*$ oscillations, for the direct correlation or the ICA approach, organised by tumour line and systemic or tumour-specific influence 101

Figure 5.7 – Frequency analysis of the O_2sat curves in SW1222 or LS174T tumour-bearing mice 102

Figure 5.8 – Relationship between tumour size, $R2*$ fluctuations and mature vasculature, for the direct correlation or the ICA approach 103

Figure 6.1 – MAP thresholding and PCA/ICA filtering on an imatinib-treated tumour at day 5 112

Figure 6.2 – Tumour growth in treated (imatinib) and control (saline) tumours assessed with MRI (left) and calliper (right) measurements 115

Figure 6.3 – Percentage of the tumour voxels experiencing spontaneous $R2*$ oscillations (A) and corresponding mean standard deviation (SD) of such variations (B) 116

Figure 6.4 – Tumour $R2*$ response to the carbogen challenge at baseline (day 0) and day 5 117

Figure 6.5 – Tumour $R1$ response to the carbogen challenge at days 0, 3 and 5 in treated (imatinib, n = 8) and control (saline, n = 3) groups 118

Figure 6.6 – Voxel-wise correlation between $\Delta R2*$ and $\Delta R1$ responses to carbogen breathing in treated tumours (n = 8) at days 0, 3 and 5 of the therapy study 119

Figure 6.7 – Tumour signal intensity (SI) response to air + 5% CO_2 breathing challenge (hypercapnia) at days 0 (baseline), 3 and 5 120

Figure 6.8 – Histology in treated (A, C) and control tumours (B) 122

Figure 6.9 – Quantitative fluorescence histology in control and treated LS174T tumours 123

Figure 7.1 – Post-processing strategy 132

Figure 7.2 – Mean standard deviation (SD) of $R2*$ time-courses in healthy and tumour regions of the prostate (n = 16) 133

Figure 7.3 – Frequencies of $R2*$ variation in healthy (n = 24) and tumour (n = 16) regions 134

Figure S6.4 – Treated (imatinib) and control (saline) tumour response to carbogen at days 0 (baseline), 3 and 5 157

List of tables

Table 4.1 – Pearson's linear correlation (r^2, *P*-value) between resting state $R2*$ standard deviation and carbogen $\Delta R2*$ in SW1222 and LS174T tumours 74

Table 4.2 – Pearson's linear correlation (r^2, *P*-value) between resting state $R2*$ standard deviation and 100% O_2 $\Delta R2*$ in SW1222 and LS174T tumours 74

Table 4.3 – Pearson's linear correlation (r^2, *P*-value) between resting state $R2*$ standard deviation and hypercapnia ΔSI in SW1222 and LS174T tumours 75

Table S7.1 – Age, PSA level and biopsy results for the cohort of patients 158

Acronyms and abbreviations

2D	Two-dimensional
3D	Three-dimensional
ADC	Apparent diffusion coefficient
ALFF	Amplitude of low-frequency fluctuation
fALFF	Fractional amplitude of low-frequency fluctuation
ANOVA	Analysis of variance
ASL	Arterial spin labelling
ATP	Adenosine triphosphate
BOLD	Blood oxygenation level-dependent (contrast)
BST	Blood supply time
CO_2	Carbon dioxide
CSI	Chemical shift imaging
DCE	Dynamic contrast-enhanced
DNA	Deoxyribonucleic acid
DNP	Dynamic nuclear polarisation
Ec	Euler characteristic
EC	Endothelial cell
ECM	Extracellular matrix
EPRI	Electron paramagnetic resonance imaging
FFT	Fast Fourier transform
FID	Free induction decay
FSE	Fast spin-echo

FT	Fourier transform
FWE	Family-wise error
GE	Gradient-echo
GEMS	Gradient-echo multi-slice
G_{FE}	Frequency encoding gradient
GLM	General Linear Model
GLUT1	Glucose transporter 1
GLUT3	Glucose transporter 3
G_{PE}	Phase encoding gradient
G_{SS}	Slice selection gradient
H&E	Haematoxylin and eosin
HIF-1	Hypoxia-inducible factor-1
IC	Independent component
ICA	Independent component analysis
IFP	Interstitial fluid pressure
MAP	Maximum *a posteriori*
MR	Magnetic resonance
MRI	Magnetic resonance imaging
NMR	Nuclear magnetic resonance
O_2	Oxygen
O_2sat	Blood systemic arterial oxyhaemoglobin saturation
PCA	Principal component analysis
PDGF	Platelet-derived growth factor

PDGFR	Platelet-derived growth factor receptor
PET	Positron emission tomography
pO_2	Partial pressure of oxygen
PSA	Prostate-specific antigen
RF	Radiofrequency
RFT	Random field theory
ROI	Region of interest
RS	Resting state
SD	Standard deviation
SE	Spin-echo
SI	Signal intensity
SMA	Smooth muscle actin
SPM	Statistical parametric mapping
TE	Echo time
TGF	Transforming growth factor
TR	Repetition time
VD	Vascular maturation
VEGF	Vascular endothelial growth factor
VF	Vascular functionality (carbogen breathing)
VO	Vascular functionality (100% oxygen breathing)

Introduction to the layout of contents

This thesis consists of 8 chapters. The first two chapters give some theoretical background and motivation for the conducted work. The methodology implemented which is common to most experimental procedures is described in Chapter 3. The structure of experimental Chapters 4 to 7 consists of a brief introduction, where additional background information is given and where the aims and hypotheses are stated, relevant materials and methods to that chapter, results, discussion and a brief conclusion. General conclusions and future directions are given in Chapter 8.

1. Introduction

Hypoxia is a condition characterised by low concentration of oxygen in the tissues (below 10 mmHg), resulting from an imbalance between oxygen supply and demand. Cancer and vascular diseases are amongst the leading causes of death worldwide [1], both being influenced by hypoxia. In the latter, the condition usually derives from the obstruction of a blood vessel, depriving the tissues of an adequate oxygen supply, consequently leading to infarction. In tumours however, the occurrence of hypoxia is a much more complex mechanism with several associated causes. Tumour hypoxia is of great importance, as it is associated with disease progression and resistance to conventional anticancer therapies, leading therefore to a poorer prognosis [2]. This chapter provides an overview of tumour hypoxia, with emphasis on cycling hypoxia, which is the subject of this thesis. Fundamental differences between tumours and normal tissues are highlighted, which are followed by an explanation of the different types of tumour hypoxia and their biological effects. Next, a description of the methods used so far to detect cycling hypoxia in tumours is presented. At the end of the chapter, the motivation for this thesis and its aim are summarised.

1.1. Structural differences between tumour and normal tissues

Tumour tissues exhibit a number of characteristics that are altered when compared to normal tissues. In the latter, vascular networks are well organised and possess linear blood vessels lined by a smooth layer of endothelial cells, with contractile pericytes enveloping the surface of the vessel to strengthen the vascular structure and regulate the microvascular blood flow. The extracellular matrix (ECM) is composed of a loose network of collagen and other fibres, and contains a limited number of fibroblasts (connective tissue cells that produce collagen) and macrophages (cells involved in the immune response). Lymph vessels are also present in normal tissues [3]. Conversely, tumour tissues contain disorganised vascular networks with abnormal blood vessels that are leaky and irregularly shaped, with varying diameters and many sac-like and dead-end formations, as well as being loosely covered by abnormal pericytes [3-6]. These characteristics are the result of an imbalance in the elaborate collaboration between the factors involved in different stages of the angiogenic process, i.e., the process by which new blood vessels are formed, and contribute to inefficient blood flow and decreased

vessel stability and function [3-6]. Tumours also contain more fibroblasts and macrophages, as well as a denser network of collagen fibres, the action of which contributes to interstitial hypertension [3;7]. Furthermore, many tumours lack or have non-functional lymph vessels, hence interstitial fluid and soluble proteins are inefficiently removed and there is raised interstitial fluid pressure (IFP) [3;4]. These structural defects in tumours, and their associated impairments, represent serious barriers to capillary blood flow, thus compromising oxygen supply to the tissues [4].

1.2. Tumour hypoxia: chronic and cycling

The previous section summarised the structural impairments of tumour tissues that cause regions of tumour hypoxia. Classically, hypoxia in tumours can be classified into two types: chronic or cycling (acute) hypoxia. Although there might not be a complete distinction between both forms of hypoxia in given tumour regions, chronic hypoxia is generally found in cells at a distance from the blood supply, and is caused by limitations in oxygen diffusion from tumour microvessels into the surrounding tissue, whereas cycling hypoxia occurs closer to the blood vessels, and is mainly a result of temporary, local disturbances in perfusion [2;8-10].

1.2.1. Chronic hypoxia

Chronic hypoxia (also known as long-term or diffusion-limited hypoxia) is characterised by constant low partial pressure of oxygen (low pO_2) as the result of chronic deficiencies of oxygen supply via the tumour vasculature [8;11;12]. Another factor that is possible to contribute to long-term hypoxia is the oxygen consumption rate of tumour cells. A few published studies have suggested that the most efficient method to reduce hypoxia is via a reduction in the oxygen consumption rate [13-15]. However, this is yet a debatable matter, as measurements of oxygen consumption rates of tumours were found to be in the midrange between normal tissues with high and low metabolic rates, thus opposing the claim that tumour hypoxia is the result of abnormally high oxygen consumption rates [8;16-18]. Several effects are associated with impaired oxygen supply to the tumour cells:

Solid tumours suffer from relatively high intervascular spacing when compared with the diffusion distance of oxygen [19], causing inadequate oxygen delivery to the cells most distant from the capillaries (the range of oxygen diffusion varies within the same tumour line and between tumour lines, with values between 40μm and 200μm being reported [8;19]).

Intravascular hypoxia has also been reported, and is probably caused by steep longitudinal gradients in oxygen tension, i.e., declines in pO_2 along the afferent path of blood flow, as opposed to the radial diffusion of oxygen [8;20]. This effect results from the lack of arteriolar supply (arterioles typically do not enter the tumour parenchyma), which may cause erythrocytes to be depleted of oxygen as they travel relatively long distances through the capillary network, combined with the fact that the blood in the tumour-feeding arterioles already suffers from partial deoxygenation before it enters the tumour parenchyma [8;20].

Additionally, hypoxic red blood cells shrink and become denser and stiffer than normally oxygenated red blood cells, causing increased blood viscosity and consequently contributing to sluggish blood flow [8;21].

Another important factor influencing chronic hypoxia is the disorganised geometry of tumour vascular networks [22]. Simulations performed by Secomb *et al.* [15] revealed impairments in the capacity of oxygen transport when considering the geometry of the tumour vasculature, even with adequate vascular density, leading to substantial regions of hypoxia. The tumour's chaotic capillary geometry also leads to plasma channels, which do not carry red blood cells, and are thus an additional source of chronic hypoxia [8;23].

1.2.2. Cycling hypoxia

Cycling hypoxia (also known as acute, transient, intermittent, fluctuating or perfusion-limited hypoxia) is characterised by cycles of low oxygen tension with subsequent reoxygenation, and is the result of transient changes in oxygen delivery due to microregional instabilities in blood and red blood cell flow, including vascular stasis [8-10;24-26]. Total vascular stasis was observed in mammary tumours, although its low incidence (4%) suggests it is not a major cause of cycling hypoxia [23]. In contrast,

flow instabilities are a rather common phenomenon [25] and may result from a combination of several factors:

Dewhirst *et al.* [23] observed temporal changes in the arteriolar diameter in mammary tumours which were coordinated with red cell flow oscillations. The investigators concluded that this vascular physiological motion (vasomotion) must be the factor causing the flow variations.

Hemodynamic factors may also cause flow oscillations. Kiani *et al.* [27] developed a mathematical model accounting for several hemodynamic effects of microvascular network blood flow. They found that the effects of non-linear flow properties of blood, non-uniform axial distribution of red blood cells within the vessel, and disproportionate cell partitioning at bifurcations relative to the blood flow partition can cause oscillations in flow parameters independent of other factors. Schmidt-Schönbein *et al*. [28] also developed a mathematical model of capillary network blood flow that accounted for the non-linear blood cell distributions and non-uniform flow rates. Similarly to Kiani *et al*. [27], they concluded that flow fluctuations could be the consequence of hemodynamic effects in capillaries without active changes in their diameters.

Additionally, the rapid vascular remodelling observed in human colon adenocarcinomas was also suggested to contribute to oscillating tumour blood flow [29].

Furthermore, the high permeability of tumour vessels causes high efflux into the tumour interstitium. The effect of this increased leakiness combined with poor lymphatic drainage, increased fibroblast-mediated tension in the fibres of the ECM, and cytokine release due to macrophage infiltration, leads to raised IFP in solid tumours [3;7;30]. In normal tissues, high IFP is usually compensated by the formation of oedema. Such mechanism is more restricted in tumours, probably due to the high density of collagen fibres that increases tissue rigidity [3]. It was demonstrated theoretically that high tumour IFP exerts a compressive force on the blood vessels, causing their partial or complete occlusion. This will, in turn, lead to an increase in pressure at the intravascular site of constriction, which will ultimately end in the reopening of the vessel. Blood flow assumes therefore an oscillatory behaviour [31] and contributes in this fashion to the observed cycling patterns of hypoxia. Solid stress generated by high cell density might also compress the capillaries, compounding the effects of high IFP [32;33].

1.2.3. Spatiotemporal characteristics of cycling hypoxia

Cycling hypoxia is a complex process with at least two characteristic time scales: one has fluctuating periods ranging from < 2 cycles/min to a few cycles per hour, and is due primarily to the rapid components of varying red blood cell flow, such as vasomotion, the differences in the distribution of red blood cells within the vessel and at vessel bifurcations, and the vessel occlusion/reopening cycling behaviour [9;10;27;34-37]. The second exhibits variations on a timescale of hours to days, and is possibly associated with vascular remodelling [9;10;38;39].

The complexity and heterogeneity of the tumour microenvironment additionally means that cycling tumour hypoxia is heterogeneously distributed across the tumour, with patterns that are tumour type-dependent [40]. Factors such as vessel immaturity and functionality can also play an important role [34;41].

1.3. Biological effects of tumour hypoxia

1.3.1. Tumour hypoxia is a source of treatment resistance

It has become evident that tumour oxygen deficiency has significant therapeutic implications. From levels of extreme tissue hypoxia up to a level of 2.6% oxygen (20 mmHg), cellular radiosensitivity is markedly dependent on oxygen tension [42], which makes tumour hypoxia a major cause of resistance to radiation therapy [24;42-44]. In normal tissues, oxygen levels range from 3.4% to 6.8% oxygen (26.0 – 51.6 mmHg) [42]. In tumours, however, tissue oxygenation falls to values between 0.3% and 4.2% oxygen (2.0 – 32.0 mmHg), with almost all exhibiting oxygenation below 2%, and where a marked skewing towards the lower end of this distribution is observed (under 1.3% oxygen (10 mmHg)) [42]. Oxygen sensitization is accepted as resulting from the interaction of oxygen with free radical species. Ionising radiation causes an increase in the production of free radicals due to the radiolysis of water. In the presence of oxygen, free radicals form highly reactive peroxy radicals which produce DNA damage, leading therefore to cell death. In the absence of oxygen, however, free radicals can be neutralised by interacting with hydrogen or by electron donation, consequently minimising radiation damage [45-47]. The reported measurable consequence of hypoxia in radiotherapy is that hypoxic cells are usually 2.5 to 3 times more radioresistant than

normally oxygenated cells [43], but can be up to 12 times more radioresistant in relation to fully oxygenated cells [48].

Tumour hypoxia also impacts negatively on the efficacy of systemically administered chemotherapeutic agents. One factor that contributes to this effect is the distance of cells from the blood supply, as drug penetration is limited and its toxicity decreases with distance from a functional vessel [49;50]. Additionally, hypoxic and nutrient-deprived cells can divide at slower rates, and so the effect of chemotherapeutic agents targeted at rapidly dividing cell populations is impaired [49]. Furthermore, the activity of many chemotherapeutic drugs is altered at low oxygen concentrations (e.g. cyclophosphamide, carboplatin, doxorubicin and bleomycin), thus further protecting hypoxic tumour populations [9;49;50]. Finally, tumour resistance to chemotherapy is probably enhanced by blood flow fluctuations, which hinder drug delivery [49-51]. The efficacy of some cytotoxic therapies is enhanced under hypoxic conditions, although these are exceptions to the more frequent effect of increased drug resistance [52].

Tumour hypoxia has additionally been shown to impair the efficacy of alternative anticancer therapies, such as immunotherapy and photodynamic therapy [50]. The latter has further (self) limitations regarding the induction of hypoxia by the therapy mechanism itself [50].

1.3.2. Tumour hypoxia promotes metastatic disease and tumour proliferation

Tumour hypoxia is associated with the mechanisms involved in increased malignancy and proliferative advantage of tumour cells, including the development of metastatic disease [2;53-55]. Hypoxia-induced tumour progression may occur as the result of alterations in gene expression or due to clonal selection [2;50]. Alterations in gene expression, namely the genes involved in the metastatic pathway, subsequently lead to changes in the proteome and/or in the genome, with a strong impact on tumour aggressiveness and proliferation [2;49;50]. Clonal selection, in turn, subjects tumour cells and proteins to a selection pressure, in which the populations that are better adapted to the hypoxic conditions thrive, further enhancing a malignant phenotype and the metastatic potential [49;50;56].

The selective pressure generated by hypoxia additionally generates tumour populations with reduced apoptotic potential, a mark of aggressiveness [57;58], and a more angiogenic phenotype. Enhanced angiogenesis is the result of hypoxia-mediated upregulation of growth factors, like vascular endothelial growth factor (VEGF), and is essential for tumour expansion and metastatic spread through the vasculature [49;50].

These factors involved in metastasis formation and tumour proliferation are additionally important because they can further impair the efficacy of antitumour therapies [50].

1.3.3. The role of HIF-1 in tumour adaptation to hypoxia

Of paramount importance to the processes mentioned above is the action of the transcription factor hypoxia-inducible factor-1 (HIF-1). HIF-1 is a key facilitator of cellular adaptation to hypoxic environments, being composed of two subunits: HIF-1α and HIF-1β [59]. Although the subunit HIF-1β is constitutively expressed, the presence of HIF-1α is dependent on growth factors [60] and cellular oxygenation [59]. In normoxia, the HIF-1α proteins are rapidly degraded. During hypoxia, however, HIF-1α becomes stabilised and translocates from the cell cytoplasm to the nucleus, where it dimerises with HIF-1β, making HIF-1 active and ready for transcription of genetic information [59]. HIF-1 activity on hypoxic tumour populations will then promote metabolic adaptation by switching to glycolytic metabolism, in which oxygen is not needed for the production of energy (ATP), and increasing glucose uptake ability, thus maintaining cell viability under hypoxic conditions [9;10;59;61;62]. Additionally, HIF-1 overexpression promotes the upregulation of pro-angiogenic factors, like VEGF, leading to increased vascular density and tumour growth, and is also associated with increased metastatic potential [9;10;59;61;62]. HIF-1 was also found to induce resistance to cytotoxic therapy, by promoting endothelial and tumour cell survival, as well as impacting on resistance to oxidative stress (i.e., cellular damage due to the accumulation of reactive oxygen species) [9;10;59;61]. Consequently, HIF-1 overexpression is associated with poorer survival in many tumour types [2].

1.4. Relative biological effects of chronic and cycling hypoxia

The oldest model proposed to explain tumour oxygen deficiency is that of chronic hypoxia [19]. However, it is now widely accepted that acute changes in tumour oxygen delivery are of similar or perhaps even greater importance [10-12]. Examples of this come from different studies:

A number of studies comprising different tumour cell lines reported the fraction of acutely hypoxic cells to be significantly higher than the fraction of chronically hypoxic cells [63-66].

Cycling hypoxic cells were also found to have increased resistance to both radiotherapy [36;37;67-69] and chemotherapy [70] treatments, when compared to chronically hypoxic tumour regions. One of the reasons for this observation is probably due to the oscillatory nature of cycling hypoxia itself. Expanding on the concept introduced in section 1.3.1, if blood flow fluctuations are of sufficient magnitude and rapidity, regions of a tumour actively proliferating at one point in time can soon after become quiescent and hypoxic. Subsequently, fluctuating tumour perfusion may exert a protective effect in tumour subpopulations during chemotherapy and radiotherapy, leaving them ready to regrow and proliferate once adequate blood flow and nutrient supply is restored [51].

Another possible factor for increased resistance to therapy is reported by Martinive *et al.* [69]. In their study, they observed that *in vitro* enforcement of cycles of hypoxia-reoxygenation to vascular endothelial cells resulted in increasing accumulation of HIF-1α after each cycle. When chronic hypoxia was enforced, subsequent reoxygenation rapidly degraded HIF-1α. Accumulation of HIF-1α during cycling hypoxia is possibly the reason why cycling, but not chronic, hypoxia was observed to promote endothelial cell survival and angiogenesis after radiotherapy, even if radiotherapy was administered in normoxic conditions. In the same study, the investigators additionally found that *in vivo* preconditioning of cycling hypoxia in tumour-bearing mice enhanced tumour regrowth and reduced apoptosis in endothelial and tumour cells after irradiation, relative to chronic hypoxic conditions. Upregulation of HIF-1 during cycling hypoxia to higher levels than those achieved by chronic hypoxia has also been observed in other studies [9;67].

Furthermore, cycling hypoxic cells were found to have greater influence on tumour progression, and higher metastatic potential, than chronically hypoxic cells [66;71;72], which once more is in agreement with the observations that HIF-1 (or HIF-1α) has higher expression during cycling hypoxia. Exposure of endothelial cells to cycling hypoxia was also shown to promote tumour inflammation amplification to a greater extent than chronic hypoxia [73].

The ability for DNA replication in different tumour cell lines after exposure to chronic and cycling hypoxia was also investigated [74]. The investigators found that chronic hypoxia prevented initiation of DNA replication following reoxygenation. Conversely, cells acutely exposed to hypoxia were able to restart DNA replication, despite the occurrence of reoxygenation-induced DNA damage. Replication restart under these conditions leads to increased genomic instability, probably due to an accumulation of unrepaired lesions [75].

1.4.1. Cycling hypoxia and glycolysis

Glycolysis is the anaerobic cellular process by which glucose is converted into pyruvate and then lactic acid, generating 2 ATP of energy per glucose molecule. Gatenby and Gillies [76] suggested that the switch to the glycolytic pathway, a near-universal property of primary and metastatic tumours, is an adaptation to cycling hypoxia, so that cells can better survive the hypoxic episodes. In fact, this theory is in agreement with the observations that cycling hypoxia upregulates HIF-1, and that HIF-1 subsequently regulates the expression of all the enzymes in the glycolytic pathway as well as the expression of the glucose transporters GLUT1 and GLUT3 [77]. At the cellular level this represents a pitfall, however, as the end product of glycolysis is lactic acid. Consequently, increased glycolytic metabolism results in microenvironmental acidosis, which ultimately leads to necrosis or apoptosis. These negative consequences of glycolysis therefore require further cellular adaptation, inducing phenotypes that are resistant to acid-induced toxicity. The most likely consequence of this cycling hypoxia-induced upregulated glycolysis is the emergence of cell populations that have both proliferative advantage and increased invasive potential [76]. Indeed, increased glucose uptake was observed to coincide with the transition of pre-malignant lesions to invasive cancer [78;79]. Furthermore, and similarly to cycling hypoxia, upregulated glycolysis

has been associated with increased occurrence of metastasis in cervical and head and neck cancers [80;81].

1.5. Methods to detect cycling hypoxia in tumours

Investigations on the detection of temporal fluctuations in tumour blood flow and tissue oxygen tension (pO_2) have been done over the years with a number of different methods:

Chaplin and co-workers [37] performed an *in vivo* study in murine SCCVII squamous cell carcinomas, in which they used a combination of radiation and a fluorescent perfusion dye (Hoechst 33342), administered either simultaneously or 20 minutes apart, to assess the relationship between radiosensitivity and oxygenation. They observed that separate, but not simultaneous, administration of Hoechst 33342 and radiation resulted in radiation resistance of brightly stained cells. This result indicated that changes in tumour blood perfusion were occurring within a 20-minute interval, which resulted in acute radiological hypoxia. They went on to confirm this observation using a 'double labelling' fluorescence technique [24].

Laser-Doppler flowmetry was also applied to study tumour haemodynamic instabilities. More precisely, microregional fluctuations in red blood cell flux were observed in two murine cell lines (sarcoma F and adenocarcinoma NT), with periodicities of 6 to 45 minutes [82]. Encouraged by these results, the same group then applied this method to 3 different human tumours (breast carcinoma, metastatic adenocarcinoma deposits and metastatic lymph node carcinoma and lymphoma), where they found fluctuations with frequencies of 1 cycle/4-44 minutes [83].

Cárdenas-Navia and colleagues [84] used recessed-tip oxygen microelectrodes to directly measure tumour pO_2 fluctuations, which were observed to occur between 2 and 5 cycles/hour in fibrosarcoma and 9L glioma rat tumours.

Braun *et al.* [35] combined laser-Doppler flowmetry with recessed-tip oxygen microelectrodes to simultaneously measure tumour blood flow and tissue pO_2 in R3230 rat mammary adenocarcinomas. Upon Fourier analysis, pO_2 and blood flow showed dominant frequencies of oscillation at < 2 cycles/minute.

Dewhirst *et al.* [23] and Kimura *et al.* [25] combined intravital microscopy and recessed-tip oxygen microelectrodes to simultaneously measure capillary red cell flux and perivascular oxygenation, also in R3230 rat mammary adenocarcinomas. They observed that fluctuant red cell flux occurs in isolated vessels and in groups of contiguous vessels, with frequencies of oscillation of 1 cycle/15-60 minutes, and that such variations were coherent with changes in perivascular oxygenation.

Skala *et al.* [85] detected blood flow fluctuations in 4T1 mouse mammary tumours, and found that these were correlated with haemoglobin saturation variations, by combining optical coherence tomography with hyperspectral imaging.

Yasui *et al.* [86] used pulsed electron paramagnetic resonance imaging (EPRI) to directly monitor pO_2 in SCCVII and HT29 mouse tumour models. They observed pO_2 fluctuations in both tumour types over a period of 28 minutes.

Magnetic resonance imaging (MRI) was also employed in the study of cycling tumour hypoxia. Baudelet and colleagues used a gradient-echo (GE) technique to investigate spontaneous fluctuations in an MRI parameter related to tumour blood flow/oxygenation [34;41]. They found significant fluctuations at frequencies ranging from a less than 1 cycle/minute to 1 cycle/hour in syngeneic fibrosarcoma tumours in mice. More recently, the same group used a MRI-sensitive fluorine compound to map tumour tissue pO_2 spontaneous fluctuations, which were observed at a rate of 1 cycle/12-47 minutes in syngeneic transplantable mouse liver tumours [87].

In addition, dynamic contrast-enhanced MRI (DCE-MRI) was used to investigate blood flow variations in A-07 human melanoma xenografts [88]. Blood flow differences were found between DCE-MRI acquisitions separated by 1 hour.

A first-pass imaging microscopy technique was also applied to the study of blood flow temporal patterns in A-07 human melanoma xenografts growing in window chambers[1] [90]. This technique estimates blood flow based on the time blood takes to travel from the main supplying artery to a given vessel site in the tumour – blood supply time (BST). Tumour maps of BST revealed it to be heterogeneous across the tumour. Additionally, BST measurements separated by 20 minutes revealed differences in

[1] The dorsal window chamber technique involves surgically implanting a titanium frame, a transparent window, and tumour cells, so as to allow microscopy imaging of the tumour. For a complete description see ref [89].

individual vessels and in groups of vessels. Homogeneous changes in BST across the whole tumour were identified when there was only one supplying artery.

Brurberg *et al.* [91;92] used OxyLite fibre-optic oxygen-sensing probes to investigate about the temporal heterogeneity in tissue pO_2 in two human melanoma xenograft lines (A-07 and R-18). They found that pO_2 fluctuated at frequencies lower than 12 cycles/hour in R-18 tumours and lower than 20 cycles/hour in A-07 tumours. The same group later used OxyLite in head and neck canine tumours, where pO_2 fluctuations were detected in untreated (1.5 – 4.3 cycles/hour) and irradiated (2.2 – 8.8 cycles/hour) tumours, regardless of their overall oxygenation status [93].

Head and neck tumours in humans were also studied using an injectable fluorine tracer (^{18}F-fluoromisonidazole (FMISO)) revealed with positron emission tomography (PET). In a first study, the investigators found that significant restructuring of tissue hypoxia regions occurred across a period of 3 days [94]. In a following study, acute hypoxia was confirmed to occur over a 3-day interval by using a mathematical approach to separate the fractions of chronic and acute hypoxia [95]. However, the slow kinetics of PET tracer retention does not allow the mapping of the fastest modes of cycling hypoxia [96;97]. The estimated influence of cycling hypoxia is that of enhancing the retention of FMISO tracer, whereas the separation between chronic and cycling contributions presents a greater challenge [96].

In summary, cycling hypoxia in solid tumours is a phenomenon that results from a combination of structural and functional abnormalities characteristic of the tumour microenvironment. It has important implications regarding patient survival, as it is associated with disease progression and malignancy, including metastatic spread, alongside resistance to different forms of therapy. So far, a range of oxygen or flow probes, cellular biomarkers and imaging techniques have been used to study the dynamics and spatial distribution of cycling hypoxia in tumours, both in mouse, rat and canine models, with few studies applied to humans.

1.6. Motivation and aim of this thesis

Although cycling tumour hypoxia has been investigated for decades [24;36;37], there still remains a need to counteract the pathological processes involved. The better we understand the cycling hypoxic processes occurring in the tumour microenvironment, the more likely we are of reversing its harmful effects; and it is this premise that gives the motivation for this thesis.

Given this, the principal aim of this thesis is to characterise the temporal and spatial aspects related to cycling hypoxia in solid tumours, using a non-invasive MRI technique, and assess its relationship with the biological characteristics of the tumour microenvironment.

2. Magnetic resonance imaging

Chapter one described the problem of tumour hypoxia and particularly cycling hypoxia, its biological effects and methods of detection. As previously mentioned, magnetic resonance imaging (MRI) is a useful method to detect and characterise cycling hypoxia in tumours. This chapter will therefore outline the basic principles of MRI, which will be followed by an overview of the biological characteristics that allow the use of MRI to non-invasively detect oscillatory patterns in blood flow and oxygenation.

2.1. Basic principles of MRI

Magnetic resonance imaging (MRI) is based on the phenomenon of 'nuclear induction' or 'nuclear magnetic resonance absorption' discovered by Bloch and Purcell in 1946. They observed that atomic nuclei which are under the influence of a constant magnetic field can absorb the energy of a weaker alternating magnetic field through a mechanism of resonance. The signal from these excited nuclei can then be detected, which will ultimately lead to the formation of an image. Resonance is thus key in MRI and this concept will be further developed in this section at a later point. Firstly however, in order to understand the interactions occurring in a magnetic resonance experiment, one should start by considering the quantum mechanical properties of atomic nuclei. A more complete description of MRI and nuclear magnetic resonance (NMR) can be found in standard textbooks [98-100].

2.1.1. Angular momentum, magnetic moment and the hydrogen nucleus

An intrinsic property of an atomic nucleus is spin or intrinsic spin angular momentum, $\boldsymbol{J}$, which can be pictured as a constant rotation of the nucleus about its own axis. Based on quantum mechanics, in the presence of an external magnetic field, the angular momentum can only take $2I + 1$ possible states, where I is the spin angular momentum quantum number. If a nucleus has either an odd atomic weight or an even atomic weight, but an odd atomic number, it has a non-zero I, which means it interacts with an external magnetic field and can, therefore, be studied using magnetic resonance. The mechanism of interaction is summarised in section 2.1.2.

The nucleus of hydrogen, consisting of a single proton, is the most common choice for MRI studies due to several reasons: it has a large natural abundance; I equal to ½; a large response to an applied magnetic field; and the fact that the human body is composed of tissues containing primarily water and fat, both of which contain hydrogen.

A nucleus that is spinning and is positively charged creates a small local magnetic field, the magnetic moment, $\boldsymbol{\mu}$:

$$\boldsymbol{\mu} = \gamma \boldsymbol{J} = \gamma \hbar I \quad , \qquad \text{Eq. 2.1}$$

where γ is the gyromagnetic ratio and $\hbar$ is the Planck's constant divided by 2π. In the presence of an applied magnetic field, the magnetic moments align with that field and revolve around this direction in a motion called precession.

2.1.2. Zeeman Effect, Boltzmann distribution and the Larmor frequency

Given that $I = ½$ for the proton, it results that there are only two possible states for $\boldsymbol{J}$, and its projection along the orientation of the applied field can take the values $\pm ½$. Consequently, the magnetic moments of the protons can only precess in two energy levels: parallel to the field (lower energy level) or antiparallel (higher energy level) (see figure 2.1A). Concepts of classical mechanics can now be applied to simplify the description of the magnetic resonance (MR) processes. This splitting of energy under the effect of a static magnetic field, B_0, is named the Zeeman effect, and the energy difference between both levels is

$$\Delta E = \gamma \hbar B_0 \quad . \qquad \text{Eq. 2.2}$$

For a collection of protons, more will normally be in the lower energy level, where the exact number of protons in each level is governed by the Boltzmann distribution:

$$\frac{N_{up}}{N_{down}} = e^{-\frac{\Delta E}{k_B T}} \quad , \qquad \text{Eq. 2.3}$$

with N_{up} and N_{down} being the number of protons in the higher and lower energy levels, respectively, k_B is the Boltzmann constant and T is the absolute temperature.

To excite the protons from the lower to the higher energy level, photons with energy ΔE and a specific frequency are needed. This frequency is the characteristic precessional frequency or Larmor frequency, ω_0, and is proportional to the strength of the magnetic field:

$$\omega_0 = \gamma B_0 \quad . \qquad \text{Eq. 2.4}$$

2.1.3. Equilibrium magnetisation and the B_1 magnetic field

The effect of a larger population of proton magnetic moments precessing in the lower energy level (parallel to $\boldsymbol{B_0}$) is the formation of a non-zero net magnetisation, the equilibrium magnetisation, $\boldsymbol{M_0}$, which is parallel to $\boldsymbol{B_0}$ (see figure 2.1B). Considering that $\boldsymbol{B_0}$ is oriented longitudinally (*z* axis), the precessional nature of magnetic moments, which are randomly oriented in the plane perpendicular to $\boldsymbol{B_0}$ but have a constant longitudinal component, means that $\boldsymbol{M_0}$ has constant magnitude in the longitudinal axis and is zero in the transverse plane (*x*-*y* plane, formed by *x* and *y* axes). Because $\boldsymbol{M_0}$ represents a large collection of nuclei, it can be treated as a macroscopic entity by classical mechanics.

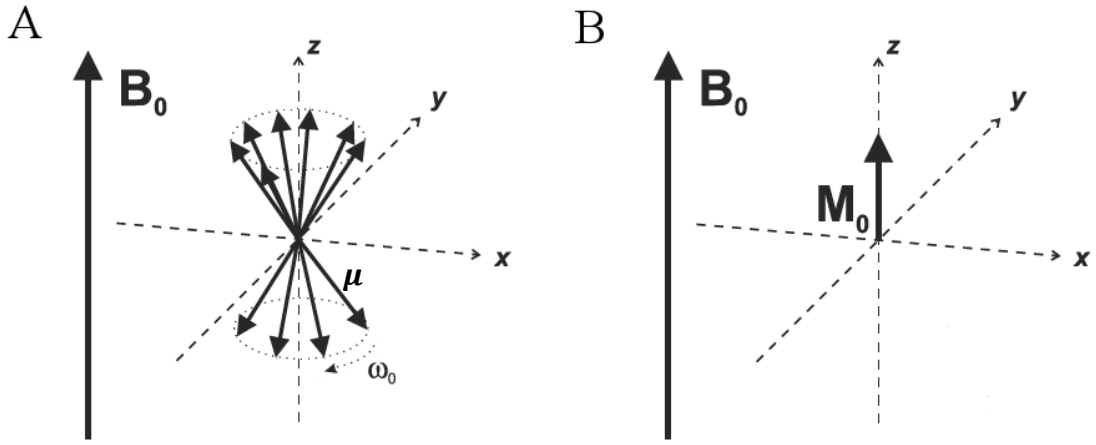

Figure 2.1 - Microscopic (A) and macroscopic (B) representations of a population of proton magnetic moments, $\boldsymbol{\mu}$, in the presence of a static magnetic field, $\boldsymbol{B_0}$. In equilibrium, the magnetic moments of protons precess out of phase about the magnetic field, but with a constant *z* component, either parallel or antiparallel to $\boldsymbol{B_0}$. Consequently, the net magnetisation in the transverse plane is zero, as the magnetic moments cancel each other, whereas longitudinally a positive net magnetisation, $\boldsymbol{M_0}$, emerges as the result of an excess of magnetic moments aligned parallel to $\boldsymbol{B_0}$. Adapted from [98].

For an MR signal to be generated, the orientation of $\boldsymbol{M_0}$ needs first to be perturbed away from equilibrium towards the transverse plane. Following this perturbation, the resultant transverse magnetisation rotates at the Larmor frequency in the *x*-y plane, which induces a current in a receiver coil tuned to the Larmor frequency and oriented perpendicularly to $\boldsymbol{B_0}$. This current is the source of the signal used to generate MR images.

The motion of the magnetisation away from its equilibrium position is achieved by applying a temporary magnetic field, $\boldsymbol{B_1}$, which is circularly polarised in the transverse plane with a frequency at (or near) the Larmor frequency. The magnetisation interacts with $\boldsymbol{B_1}$ by resonance causing it to rotate about $\boldsymbol{B_1}$ towards the transverse plane. To simplify the understanding of this mechanism and its effects, a rotating frame at the Larmor frequency and about the *z* axis is usually considered, thus making $\boldsymbol{B_1}$ appear as a fixed magnetic field (see figure 2.2). In this rotating frame, the motion of $\boldsymbol{M_0}$ is given by:

$$\left(\frac{d\boldsymbol{M_0}}{dt}\right)_{rot} = \gamma \boldsymbol{M_0} \times \left(\boldsymbol{B_0} - \frac{\boldsymbol{\omega_0}}{\gamma} + \boldsymbol{B_1}\right) = \gamma \boldsymbol{M_0} \times \boldsymbol{B_1} \quad , \qquad \text{Eq. 2.5}$$

where the minus sign of $\boldsymbol{\omega_0}$ defines a clockwise rotation of the frame. The angle formed by $\boldsymbol{M_0}$ and $\boldsymbol{B_0}$ is called the flip angle, α (see figure 2.2B). If the magnetisation vector ends up exactly in the transverse plane by the time $\boldsymbol{B_1}$ is turned off, then $\alpha = 90°$ and it is called a $90°$ radiofrequency (RF) pulse.

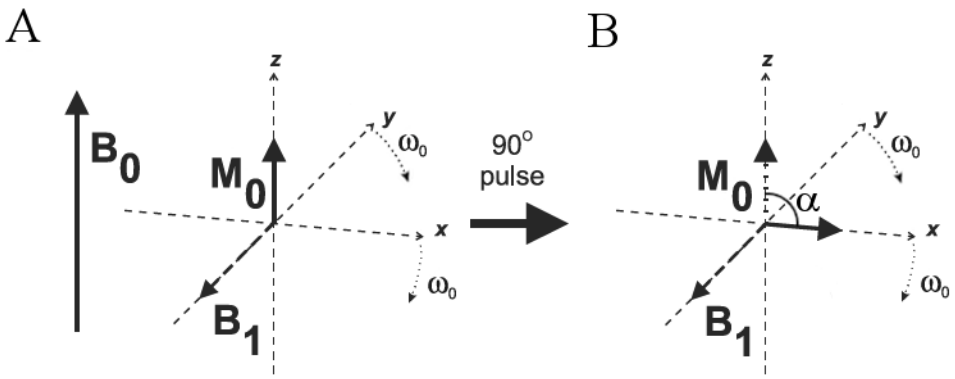

Figure 2.2 - Mechanism of resonance absorption. A: the radiofrequency pulse induces a magnetic field $\boldsymbol{B_1}$ perpendicular to $\boldsymbol{B_0}$, which appears stationary in the rotating frame. **B:** $\boldsymbol{M_0}$ precesses about $\boldsymbol{B_1}$ towards the transverse plane with a flip angle, α. Adapted from [98].

2.1.4. Relaxation

2.1.4.1. Longitudinal relaxation (T_1 relaxation)

After the $\boldsymbol{B_1}$ field is turned off, and in the case of a 90° pulse, the magnetisation vector remains rotating in the *x*-*y* plane. This is, however, a temporary state as the longitudinal component of the magnetisation vector, $\boldsymbol{M_z}$, returns to equilibrium ($\boldsymbol{M_0}$). This recovery is named longitudinal relaxation, spin-lattice relaxation, or T_1 relaxation, and evolves exponentially with a tissue-characteristic time constant T_1:

$$\boldsymbol{M_z}(t) = \boldsymbol{M_0}\left(1 - e^{-t/T_1}\right) \quad . \qquad \text{Eq. 2.6}$$

Longitudinal relaxation reflects the transfer of excess heat, previously acquired with the RF excitation ($\boldsymbol{B_1}$ field), from the spin system into nearby atoms and molecules, allowing protons to return to thermal equilibrium with its surroundings. This process is stimulated by local magnetic fields fluctuating near the Larmor frequency, which originate from molecular tumbling.

2.1.4.2. Transverse relaxation (T_2 and T_2^* relaxation)

In addition to longitudinal relaxation, the magnetisation that is rotating in the *x*-*y* plane, $\boldsymbol{M_{xy}}$, also evolves by decaying due to phenomena that disrupt the transverse

phase coherence of individual proton magnetic moments. Transverse relaxation, or spin-spin relaxation, reflects the rate at which $\boldsymbol{M_{xy}}$ is lost, decaying exponentially with a tissue-specific time constant T_2:

$$\boldsymbol{M_{xy}}(t) = \boldsymbol{M_0} e^{-t/T_2} \quad . \qquad \text{Eq. 2.7}$$

Dipolar interactions between proton magnetic moments contribute to T_2 relaxation. When two protons come close together, a slight positive or negative variation in the magnetic field is experienced by each of them, as the magnetic moment of the other proton adds or subtracts from the main field. This interaction leads to differences in their precessional frequencies and, consequently, loss of transverse phase coherence occurs, which causes a decay of $\boldsymbol{M_{xy}}$.

Surrounding magnetic molecules also influence transverse relaxation because they introduce local static field disturbances. This effect can occur when, for example, a water molecule is diffusing through an iron-containing media, which adds or subtracts from $\boldsymbol{B_0}$, making the spins experience a range of $\boldsymbol{B_0}$ fields and, consequently, a range of precessional frequencies. Consequently, this effect also causes a reduction in the magnitude of $\boldsymbol{M_{xy}}$ as the spins dephase relative to each other.

In addition to these T_2-only relaxation mechanisms, transverse relaxation also occurs accompanying T_1 relaxation. This happens due to the loss of transverse phase coherence associated with dissipation of energy to the tissues.

Because it depends on a combination of mechanisms, transverse relaxation evolves faster than longitudinal relaxation, and T_2 is usually shorter than T_1. Where T_2-only effects are minimised, T_2 approaches T_1.

Magnetic moments experience yet another source of dephasing, that of magnetic field inhomogeneities in $\boldsymbol{B_0}$, either due to magnet design inaccuracies or due to the presence of a biological sample with non-zero magnetic susceptibility. This effect causes the spins to dephase actually faster than at the T_2 rate, and transverse relaxation evolves with a shorter time constant T_2^*:

$$\frac{1}{T_2^*} = \frac{1}{T_2} + \frac{1}{T_2'} \quad , \qquad \text{Eq. 2.8}$$

where T_2' is the parameter related to magnetic field inhomogeneities in $\boldsymbol{B_0}$. In reality, the effects of microscopic diffusion of the protons also have an effect on T_2^* decay, and so a term $1/T_{2d}$ should be included in eq. 2.8. Therefore, the signal measured in the receiver coil, named free induction decay (FID), decays with time constant T_2^* (figure 2.3). An MRI sequence conceptually similar to the one implemented in this thesis at 9.4 T to estimate the relaxation rate R_2^* $(= 1/T_2^*)$ can be observed in figure 2.5, with its description in section 2.1.5.

The fact that the rate of signal decay depends on the local physiological state is an important observation for functional studies. Particularly, the state of blood oxygenation influences the local magnetic field, which allows indirect measurements of local changes in blood oxygenation [101;102]. An explanation of how these endogenous magnetic properties of blood are interpreted in functional MRI is in section 2.2.

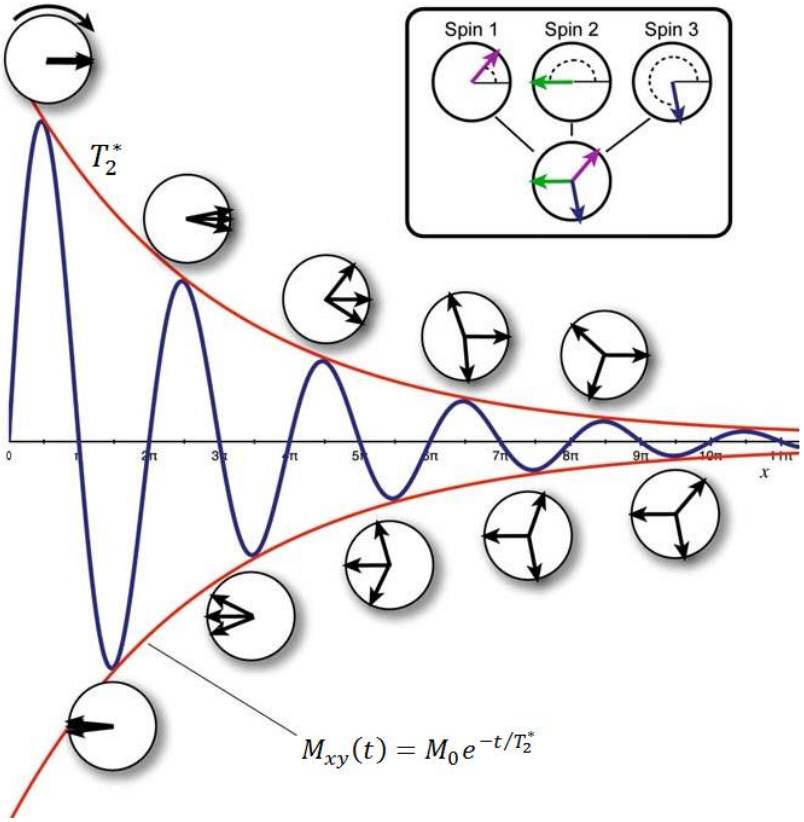

Figure 2.3 – Free induction decay (FID). The amplitude of the measured signal in the receiver coil (red curve) decays exponentially with time constant T_2^*. The magnetization in the *x-y* plane oscillates at the resonance frequency (blue curve) and becomes progressively smaller due to spin dephasing (represented in the circles by three superimposed spins (see inset)). T_2^* inherently depends on the quality of the magnet, where a poor magnet generates a more inhomogeneous field than a good magnet, thus further shortening the FID. Adapted from [100].

2.1.5. Image formation

In MRI, images are obtained via the implementation of pulse sequences. Pulse sequences consist of temporal protocols in which RF pulses and magnetic field gradients are applied, which allow the detection of MR signals. Magnetic field gradients consist of small magnetic perturbations (~1%) superimposed on the static magnetic field $\boldsymbol{B_0}$ and linearly varying in one spatial direction. They are essential in the process of image formation because they allow the spatial localisation of MR signals. This section describes the principles of a 2D pulse sequence, as implemented in this thesis. Comparatively, 3D or more complex sequences present slight or considerable differences, respectively. A 2D pulse sequence can employ three fundamental processes: slice selection, frequency encoding and phase encoding.

Slice selection consists of the application of a RF pulse of desired frequency and bandwidth simultaneous with a gradient, the slice selection gradient, G_{SS}. The gradient causes protons to precess at different frequencies depending on their position along the gradient direction. Only the protons located in the slice at resonant frequency will be excited. This means slice position is determined by the central frequency of the pulse and the amplitude of G_{SS} and slice thickness depends on the bandwidth of the RF pulse and the amplitude of G_{SS}. Upon slice selection, which includes a rephrasing (negative) G_{SS} lobe to realign the spins in the *x*-*y* plane, G_{SS} is turned off.

Within the excited slice, spatial information is further encoded by applying two additional gradients, orthogonal between themselves and to G_{SS}. The frequency encoding gradient, G_{FE}, is applied at the time of signal acquisition (readout), causing a linear variation of the precessional frequency along that spatial direction. The phase encoding gradient, G_{PE}, is turned on and off before the readout starts. It has the effect of causing a phase shift in the precessing nuclei that is dependent on their position along the direction of G_{PE}. The pulse sequence is repeated with different strengths of G_{PE}, allowing all positions within the slice to have a unique combination of frequency and phase. For examples of basic MRI sequences see section 2.1.6.

An alternative way of looking at this process is by considering the acquired data is arranged in a 'raw data space' two-dimensional matrix called *k*-space, with frequency-encode and phase-encode directions. With each sequence repetition, a full line of *k*-space is acquired in the frequency-encode direction at the time G_{FE} is applied. Each line of *k*-space has a different position in the phase-encode direction, which results from a change in G_{PE} between repetitions. *K*-space is thus filled line by line with each sequence repetition. The information in the centre of *k*-space contains the signal-to-noise and contrast information for the image, whereas the information around the outside contains the information about the resolution of the image, important for edge detection. A two-dimensional image can then be obtained by applying a two-dimensional Fourier transform (2D FT) to *k*-space.

2.1.6. Basic MRI sequences: spin-echo and gradient-echo

The rate at which spins dephase in the *x*-y plane depends on random effects as well as fixed effects. T_2 decay due to spin-spin interactions is a random effect, and is

therefore irreversible. Conversely, static $\boldsymbol{B_0}$ inhomogeneities are often constant, hence fully reversible by application of a 180° RF 'refocusing' pulse.

Spin-echo (SE) pulse sequences explore the effect of spin dephase reversibility as a means to retrieve the characteristic T_2 of tissues. Figure 2.4 illustrates a spin-echo sequence, with the evolution of the magnetisation vector in the top two rows. The initial 90° RF pulse is applied simultaneously with G_{SS} to excite a slice of the sample, causing the magnetisation vector to rotate into the *x*-*y* plane. A negative lobe of G_{SS} is applied to rephase the spins that started to dephase during slice selection. Spins then start to dephase in the transverse plane due to spin-spin interactions and off resonance effects (e.g. magnetic field inhomogeneities). A phase encoding gradient is applied together with a frequency encoding gradient, which causes further spin dephasing and describes a *k*-space trajectory from the centre of *k*-space towards a corner edge. A slice selective 180° RF pulse is then applied (on the *x* axis) which reverses the effect of spin dephasing occurring due to off resonance effects, it does not reverse the random spin-spin decay, and describes a *k*-space trajectory to the opposite corner edge location. A frequency encoding gradient of the same polarity is applied and an echo is formed when the gradient moment (duration × gradient amplitude) equals that before the 180° 'refocusing' pulse, at the echo time, *TE*. This frequency encoding gradient reverses the initial gradient-driven dephase and allows one line of *k*-space to be filled. The echo height depends on T_2 relaxation, effectively minimising local field inhomogeneity effects. The time between successive excitation pulses is the repetition time, *TR*. The signal obtained by a spin-echo sequence is T_2-weighted and is given by:

$$S_{SE} = k\rho\left(1 - e^{-TR/T_1}\right)e^{-TE/T_2} \quad , \qquad \text{Eq. 2.9}$$

where k contains constants and terms based on extrinsic parameters (like the number of signal averages and the slice thickness) and ρ is the proton density of the excited volume.

Conversely, gradient-echo (GE) sequences are commonly used to obtain measurements of T_2^*. Figure 2.5 illustrates a gradient-echo sequence with spoiler gradients. The slice selective excitation pulse is initially applied, which moves the magnetisation vector towards the *x*-*y* plane with a flip angle usually inferior to 90°. A negative G_{FE} is then applied, causing rapid dephasing of the transverse magnetisation component. At the same time, phase encoding is performed along the remaining axis.

Together, G_{FE} and G_{PE} cause a *k*-space trajectory towards the corner edge of *k*-space. Next, a positive G_{FE} is applied, acting as a spin refocusing mechanism. One line of *k*-space starts then to be filled. When the positive gradient moment equals the negative moment an echo is produced. The height of this gradient-echo depends on T_2^* relaxation because the positive gradient lobe only compensates for the previous dephasing caused by the negative lobe; it does not refocus the loss of precessional coherence caused by field inhomogeneities or spin-spin interactions. If G_{FE} is left on, the spins get out of phase again. At the end of the acquisition, spoiler gradients are used to destroy any left-over transverse signal coherence before the next RF excitation pulse is applied. The signal obtained by a spoiled gradient-echo sequence is T_2^*-weighted and is given by:

$$S_{GE} = k\rho \frac{\sin\alpha \left(1 - e^{-TR/T_1}\right) e^{-TE/T_2^*}}{1 - \cos\alpha \, e^{-TR/T_1}} \quad , \qquad \text{Eq. 2.10}$$

where α is the flip angle.

As noted above, single-echo GE images depend on several factors (e.g. T_1, T_2^*, proton density) which is sometimes undesirable as it may produce confounding effects. Multi-echo GE sequences address this issue by implementing continuous G_{FE} reversal, which produces multiple echoes at the echo times TE_1, TE_2, TE_3 ... The height of the echoes depends on the parameters k and ρ as well as the T_2^* decay, but the envelope of these echoes follows an exponential decay which only depends on T_2^* relaxation, thus eliminating the influence of T_1 and proton density:

$$S_{GE}^{multi-echo} = k\rho \, e^{-TE/T_2^*} \quad . \qquad \text{Eq. 2.11}$$

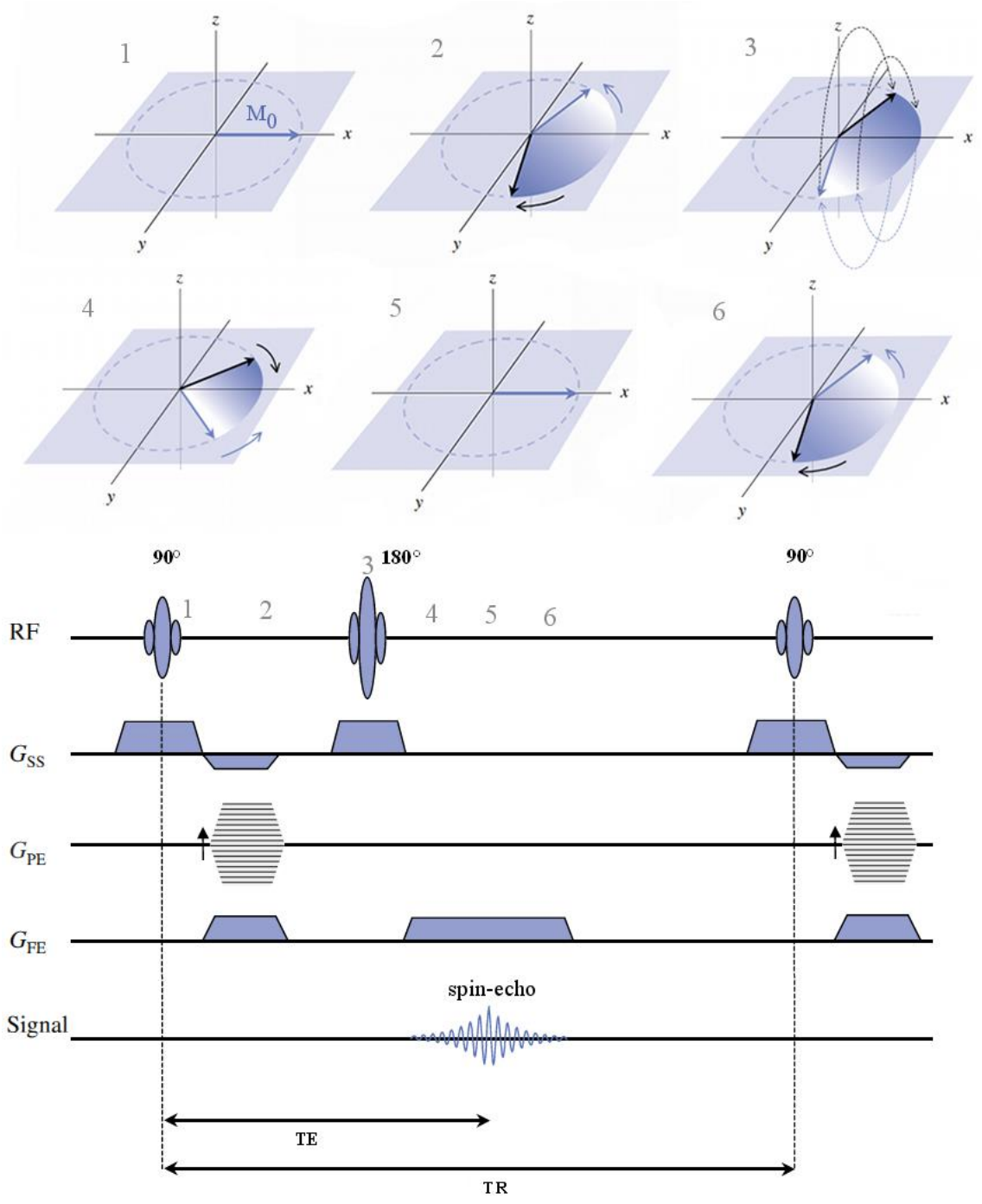

Figure 2.4 – Spin-echo imaging sequence. The evolution of the magnetisation vector, $\boldsymbol{M_0}$, is represented in the first two rows. RF pulses and gradient application are shown in the bottom. The 90° excitation pulse is made slice selective (G_{SS}) and rotates $\boldsymbol{M_0}$ to the *x*-*y* plane (1). Spins start to dephase in the *x*-*y* plane (2). A 180° RF pulse is applied (3), which reverses the spin dephasing (4). The re-phased spins generate an echo at time TE (5). After *TE*, the spins start again to dephase (6). Adapted from [99].

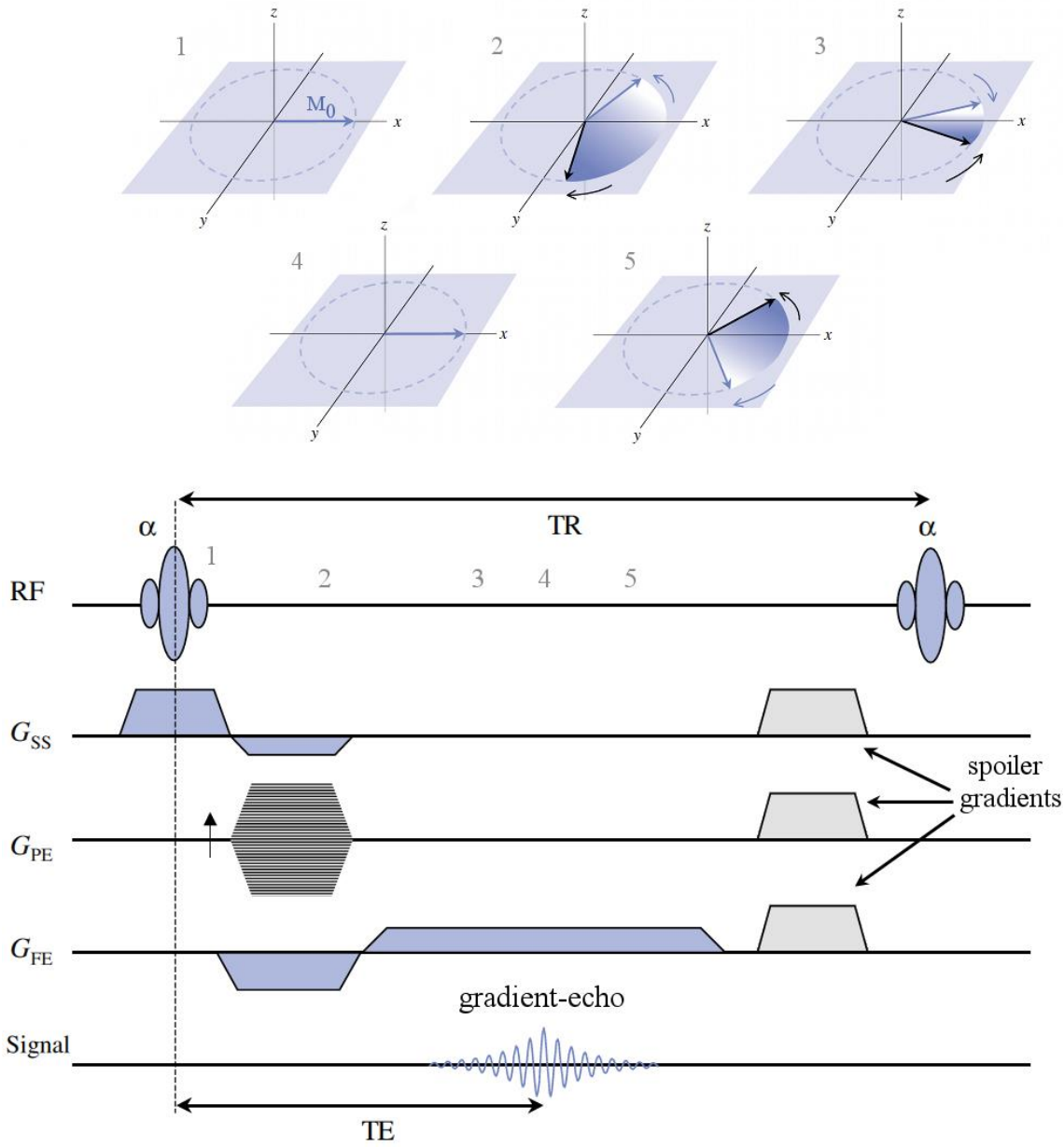

Figure 2.5 – Spoiled gradient-echo imaging sequence. The evolution of the magnetisation vector, $\boldsymbol{M_0}$, is represented in the first two rows. The fact that $\boldsymbol{M_0}$ is in the transverse plane is a simplification, given that the flip angle, α, is usually < 90° in gradient-echo sequences. RF pulses and gradient application are shown in the bottom. The excitation pulse is made slice selective (G_{SS}) and rotates $\boldsymbol{M_0}$ towards the *x*-*y* plane (α < 90°) (1). Negative G_{FE} causes extra spin dephasing (2). Positive G_{FE} reverses spin dephasing (3) and a gradient-echo is produced at time *TE* (4). Spins return to dephase due to the continuous effect of G_{FE} (5). Spoiler gradients are applied before a new excitation pulse with the objective of dephasing the transverse magnetisation. Adapted from [99].

2.2. Gradient-echo MRI as a method of detecting variations in blood flow and oxygenation

The multitude of dependencies affecting the gradient-echo signal decay allows the monitoring of haemodynamic changes in two ways: variations in blood oxygenation or in blood flow [103;104]. In the first case, blood oxygenation level-dependent (BOLD) contrast is commonly employed [101;102]. This method uses the endogenous magnetic properties of haemoglobin to estimate changes in blood oxygen saturation. Oxyhaemoglobin is weakly diamagnetic, which means the magnetic susceptibility of oxygenated blood is similar to that of surrounding tissues, therefore causing minimal distortion to the local magnetic field [102;105]. Conversely, deoxyhaemoglobin is paramagnetic, meaning the magnetic susceptibility of deoxygenated blood is considerably different from that of the surroundings. This difference generates local field inhomogeneities that are large enough to cause rapid dephasing of the local magnetic moments of the water protons in the blood and surrounding tissues [102;106]. In fact, the measure MR signal change between oxy- and deoxygenated blood is composed of an intravascular contribution (water molecules in the blood itself) and an extravascular contribution (water molecules in the tissue surrounding the vessels) [105]. Since the volume of a voxel is usually large when compared to individual vessels, especially tumour capillaries, the observed BOLD signal will be a volume-weighted average of intra- and extravascular water signals [105]. Although the majority of the water molecules reside in the extravascular compartment, the intravascular contribution can be quite significant, especially at lower field strengths (e.g. 1.5 T). At higher field strengths the intravascular contribution is decreased, however, due to the decrease of the intrinsic T_2 and T_2^* of deoxygenated blood [105]. A detailed review of the intra- and extravascular effects of water on the BOLD signal can be found in ref. [105]. Regardless of the field strength, increased deoxyhaemoglobin concentration impairs the phase coherence of the local magnetic moments, which manifests as a faster T_2^* decay and results in a less intense GE signal (eq. 2.10).

Blood flow variations also have an effect on the measured gradient-echo signal. Considering a vessel with static or slow flowing blood, if no complete relaxation occurs between excitation pulses[2] (i.e., $TR < T_1$) the longitudinal magnetisation reaches a low-recovery equilibrium state after a few repetitions (saturation). Consequently, the GE

[2] At 9.4 T, a GE sequence usually has *TR* no longer than a few hundreds of milliseconds whereas $T_{1\ blood\ (9.4T)} \sim 2430$ ms [107].

signal produced is lower than in the case of complete relaxation. Conversely, in the case of high blood flow, the water in fresh blood flowing into the imaging slice is fast enough not to be subject to magnetic saturation from previous RF pulses, therefore producing a stronger GE signal. This observation is known as the 'in-flow effect' [103;104]. Also, an increase in blood flow potentially results in an increase in the concentration of saturated haemoglobin [108], further intensifying the generated GE signal.

As mentioned in section 2.1.6, single-echo GE signal intensity changes can be hard to interpret and multi-echo GE is alternatively used to isolate the T_2^* of tissues and make data interpretation more straightforward. In-flow effects can additionally be minimised by using low flip angles. In multi-echo GE, the transverse relaxation constant R_2^* $(= 1/T_2^*)$ is commonly used. It should be mentioned, however, that multi-echo GE can also have confounding effects, given that a change in R_2^* can additionally reflect changes in blood volume, blood pH, haematocrit or in the fraction of oxygen extraction by the tissue [108]. Consequently, R_2^* (or T_2^*) estimates were found not to provide a quantitative measurement of tumour pO_2, showing only a good qualitative agreement [109]. The sensitivity of R_2^* estimates to a given pO_2 change was also observed to vary from one tumour to another [109].

2.2.1. Assessment of cycling tumour hypoxia with gradient-echo MRI

Temporal variations in T_2^*-weighted GE images in tumour measurements have been suggested to be related to spontaneous fluctuations in blood flow and oxygenation, associated with the pathophysiology of acute hypoxia in tumours, in a study using FSa fibrosarcomas [34].

Following this demonstration, the same group investigated the relationship between tumour vessel properties, such as maturation and functionality, and T_2^*-weighted GE signal fluctuations [41]. Mature vessels, coated with pericytes and smooth muscle cells, dilate in response to a hypercapnia challenge (elevated CO_2 breathing), causing an increase in blood flow [110]. Conversely, immature endothelial capillaries show no reactivity to hypercapnia [110]. Functional blood vessels can be identified by an increase in haemoglobin saturation in response to hyperoxia (elevated O_2 breathing), revealing blood is being perfused throughout these vessels [110]. Carbogen (95% O_2 +

5% CO_2), as opposed to 100% oxygen, has preferentially been used in a number of studies [41;104;111-113] because, in addition to high concentration of oxygen, it also has a high concentration of carbon dioxide. The vasodilatory effect of CO_2 is expected to counteract the vasoconstrictory effect of oxygen, preventing vessel closure [49]. Results indicated the majority of spontaneous T_2^*-weighted fluctuations were in regions of functional and immature vasculature [41]. Vessel functionality, however, does not guarantee the presence of fluctuations. Also, the few regions of mature vasculature presented high incidence of signal fluctuations, potentially revealing the effect of vasomotion (i.e., temporal changes in the diameter of blood vessels) in generating cycling hypoxia.

More recently, Nielsen and colleagues [114] used a ultra-high magnetic field system (16.4 T) to assess the occurrence of cycling hypoxia and the effect of nicotinamide administration, a blood flow enhancing drug, in C3H mouse mammary carcinomas. They implemented a multi-echo GE sequence and observed temporal variations in T_2^* across a 20-minute period. However, nicotinamide did not reveal significant effects on these tumours. Conversely, when administered together with carbogen, nicotinamide was observed to reduce the percentage of the tumour experiencing T_2^*-w fluctuations in FSa fibrosarcomas [34]. The anticipated physiological effect of administrating nicotinamide is that of reducing cycling hypoxia [108], although its effect is likely to vary between different tumour types [115].

3. Experimental protocols and image analysis

The aim of this thesis is to adapt and develop methodology to further characterise cycling hypoxia in tumours and assess its relationship with microenvironmental biological characteristics. This chapter describes the methodology implemented to that end and which is common to the majority of pre-clinical studies comprised in this thesis. Details of specific methods will be given in the corresponding chapters. All animal experiments were performed in accordance with the local ethical review panel, the UK Home Office Animals Scientific Procedures Act 1986, and United Kingdom Co-ordinating Committee on Cancer Research guidelines [116].

3.1. Xenografts

Two human colorectal adenocarcinoma cell lines were used: SW1222 and LS174T. These tumour lines were chosen for several reasons: they develop into xenografts with differing morphology and vascular architecture, they are readily available in the department and they have been well characterised due to previous work. SW1222 tumours are well-differentiated with clearly defined glandular structures and an extensive and well perfused vascular network. Conversely, LS174T tumours show moderate-to-poor differentiation and are comparatively less well vascularised and perfused, with larger hypoxic and necrotic regions [117-120].

3.2. Cell culture and mouse model

All cell work was performed at the UCL Cancer Institute. Cells of SW1222 or LS174T tumour lines were thawed from a stock of aliquots stored in liquid nitrogen. Cells were grown for 2 weeks prior to injection in complete media (Minimum Essential Medium Eagle with L-Glutamine (EMEM) (Lonza, Belgium) + 10% fetal bovine serum (Invitrogen, UK)) in a ratio 1:20 (v/v) and incubated at 37 °C and 5% CO_2. Media was changed every 2 days.

To prevent excessive confluence, cells were split twice per week, in which cells were washed with Dulbecco's Phosphate Buffered Saline (DPBS) (Lonza, Belgium) and detached with trypsin-EDTA (0.05% trypsin, 0.02% EDTA in Hank's Balanced Salt

Solution, Sigma-Aldrich, USA) for 7-8 minutes at 37 °C and 5% CO_2. Complete media was then added to prevent detrimental effects of trypsin-EDTA, and cells were mixed with a pipette to prevent major clustering, being finally divided into new flasks containing complete media.

To prepare injections, cells were washed with DPBS and detached with trypsin-EDTA (7-8 min, 37 °C, 5% CO_2). Complete media was added to annul trypsin-EDTA and the total volume was transferred to a falcon tube where cells were mixed to promote separation. The falcon tube was placed in a centrifuge for 5 minutes at 259 g (= 1200 rpm). The resulting pellet of cells was separated from the media and re-suspended in DPBS. Cells were again centrifuged and the pellet re-suspended in EMEM. Cell concentration and viability was estimated by mixing 50 µl of the suspension with 50 µl of trypan blue (Life Technologies, USA) and using a haemocytometer. Final volumes of EMEM were calculated to obtain a concentration of 5×10^6 cells per 100 µl.

To propagate tumours, 5×10^6 cells (SW1222 or LS174T) were injected subcutaneously in the flank of immunocompromised (dysfunctional thymus and T-cell deficient) CD1 female nude mice (6-9 weeks age, 20-30 g) and MR imaging took place approximately after 2 weeks of tumour growth.

3.3. *In vivo* MRI

3.3.1. Experimental setting

Prior to MR imaging, anaesthesia was induced in mice by 5% isoflurane in medical air (78% N_2 + 21% O_2 + traces of Ar, CO_2, H_2, water vapour and others) and subsequently maintained in the scanner by 1.25% isoflurane in medical air, oxygen, or other gas mixtures, at 1 L/min., using a nose cone. The anaesthetised mice were placed in a purpose-built cradle and secured using adhesive tape and dental paste (CharmFlex Light LV, Dentkist Inc., South Korea) to minimise motion [111;121]. Warm air and water were used to maintain normothermia. Core temperature and respiratory rate were monitored using a rectal thermometer and respiratory bellows, respectively (SA Instruments Inc., NY, USA).

3.3.2. Imaging protocol

All pre-clinical MRI data were acquired using a 9.4 T (400MHz, ^{1}H) VNMRS 20 cm horizontal-bore system (Agilent Technologies Inc., CA, USA) with a 39 mm transmit/receive birdcage coil (Rapid Biomedical, Germany). Fast spin-echo (FSE) images were initially acquired for anatomical reference. Dynamic gradient-echo multi-slice (GEMS) images were subsequently acquired in order to map the temporal variation of the tumour relaxation rate, R_2^*. Two 60-minute spoiled GEMS scans were acquired for each subject. The first, a dynamic 'resting state' scan, was used to evaluate R_2^* spontaneous fluctuations at rest, i.e., with no additional external influences. The second, a 'gas challenge' scan, included 6 interleaved gas challenges: air, carbogen (95% O_2 + 5% CO_2), air, 100% O_2, air, air + 5% CO_2. Each gas challenge lasted 10 minutes. Carbogen and 100% O_2 challenges were aimed at studying the regional effect of hyperoxia on R_2^*. Hypercapnia (air +5% CO_2) was used to map in-flow effects on signal intensity images. Imaging parameters for the FSE acquisition were: *TR = 1500 ms, effective TE = 32.9 ms, echo spacing = 8.2 ms, echo train length = 4, in-plane field of view 40×40 mm^2, matrix size 128×128, slice thickness 1 mm, 20 slices, flip angle = 90°*. GEMS sequence parameters were: *TR = 59.62 ms, 5 echoes, TE_1 = 2 ms, echo spacing = 2 ms, in-plane field of view 20×20 mm^2, matrix size 64×64, slice thickness 1.5 mm, 5 slices, flip angle = 20°, 3.8 s/image*.

3.4. MRI data analysis

Post-processing of the acquired MRI data was carried out using routines written in Matlab (v. 7.11, The MathWorks Inc., USA) and Interactive Data Language (IDL, v. 8.0, Exelis Visual Information Solutions, USA). The majority of datasets presented time-varying susceptibility artifacts in the imaging slices positioned closer to the gut, as assessed by observation of dynamic signal intensity images at *TE* = 2 ms and *TE = 6* ms. Such imaging slices were excluded from analysis. Statistical analysis was carried out using GraphPad Prism (v. 6.01, GraphPad Software Inc., USA). $P < 0.05$ was considered to be significant, unless otherwise stated.

3.4.1. Relaxometry estimation and calculation of resting state and gas challenge maps

Estimation of R_2^* relaxation rate was performed on a voxel-by-voxel basis by least-squares fitting of a single exponential decay to signal intensity curves as a function of echo time, as described by eq. 2.11. Tumour areas were selected by drawing regions of interest (ROIs) in each MRI slice. The amplitude of resting state (RS) spontaneous oscillations was assessed by creating voxel-wise standard deviation (SD) maps of R_2^* time courses:

$$R_2^* SD = \left(\frac{1}{n-1} \sum_{i=1}^{n} (x_i - \bar{x})^2 \right)^{1/2} \quad . \qquad \text{Eq. 3.1}$$

The standard deviation calculation was considered to be an appropriate method to assess the resting state cycling events' characteristics of interest in this thesis. Nevertheless, the effect of cycling hypoxia is effectively a frequency-specific characteristic, and an alternative method, named amplitude of low-frequency fluctuation (ALFF) [122] could have been employed instead to account for that. Also, noise is here considered to be characterised only by the image background, which constitutes a limitation if physiological noise is present, which could be best accounted for with fractional ALFF (fALFF) [123].

Gas challenge time courses were used to create voxel-wise maps of vessel functionality with carbogen (VF) [41] and with 100% O_2 (VO) as well as of vessel maturation (VD) [41]. VF and VO maps were created from the difference between the mean R_2^* values during carbogen or 100% O_2 breathing and air breathing. VD maps were created from the difference between the mean signal intensity (SI) values during hypercapnia and air breathing:

$$\begin{aligned} VF &= \Delta R_{2\,Carb}^* = \overline{R_2^*(carbogen)} - \overline{R_2^*(air)} \\ VO &= \Delta R_{2\,O_2}^* = \overline{R_2^*(O_2)} - \overline{R_2^*(air)} \\ VD &= \Delta SI_{CO_2} = \overline{SI(air + 5\%\, CO_2)} - \overline{SI(air)} \quad . \end{aligned} \qquad \text{Eq. 3.2}$$

The times at which R_2^* or SI exhibited an increase or decrease as the result of changing the breathing gas were assessed individually for each tumour by observing the respective time courses. The transition phase observed after the gas change and until reaching a new plateau (see Figs. 4.7A and 4.10A – Chapter 4) was not included in the calculations of eq. 3.2.

3.4.2. Noise estimation in resting state maps

Estimates of R_2^* will always have an associated uncertainty due to the influence of measurement noise [124]. The approach implemented here to account for uncertainty in R_2^* due to background noise was adapted from the work of Walker-Samuel *et al*. [124]. A Bayesian maximum *a posteriori* (MAP) approach was used, considering Rice-distributed data, allowing a robust voxel-wise determination of the uncertainty in R_2^* in all time points. In these conditions, the cost function to be maximised is the log-likelihood, l_R, which reflects the probability distribution for the Rice-distributed MRI data :

$$l_R(\theta; P) = \sum_{i=1}^{n} \left(\ln P_i - 2 \ln \sigma_R - \frac{P_i^2 + S_i^2}{2\sigma_R^2} + \ln I_0 \left(\frac{P_i S_i}{\sigma_R^2} \right) \right) \quad , \qquad \text{Eq. 3.3}$$

where θ are the parameters to be optimised (i.e., R_2^* and S_0 (signal intensity at echo-time = 0)), S is the signal intensity in transverse relaxation, P are the n measured data points, σ_R^2 is the variance of the noise in the raw MR data and I_0 is the zeroth-order modified Bessel function [124].

The (two-dimensional) joint posterior distribution for R_2^* and S_0 is directly proportional to the likelihood function: $p(S_0, R_2^* | P) \propto L(\theta; P) = e^{l(\theta;P)}$. Estimation of the posterior distribution of R_2^* is done through integration of the joint posterior distribution with respect to S_0:

$$p_{R_2^*}(R_2^* | P) = \int p(S_0, R_2^* | P) dS_0 \quad . \qquad \text{Eq. 3.4}$$

The peak value and "spread" of R_2^* are used as the point estimate and uncertainty [124]. A region of background noise, completely excluding tissue voxels, was selected to provide an estimate of σ_R. To assess if R_2^* spontaneous fluctuations were above the uncertainty associated to background noise, maps of standard deviation over the uncertainty were computed (SD/uncertainty). Voxels with a value of SD/uncertainty > 1 were taken to reflect an uncertainty lower than amplitude of fluctuations and were thus selected for further analysis.

3.4.3. Correction of gas challenge maps

In order to identify significant effects in gas challenge maps, a voxel-wise statistical analysis should be performed. Calculating a statistic for each voxel results in a large volume, or family, of statistic values. A t-statistic is commonly employed, where each supra threshold voxel has an associated small probability of having survived by chance alone, i.e., when the null hypothesis is true. However, in a family of voxel statistics, these type I errors multiply, so that the number of surviving voxels when in fact there is no effect is larger than desired. This constitutes the multiple comparison problem [125].

The Bonferroni correction could be used to circumvent this problem and set a new (higher) statistic threshold for the whole family of voxel statistics: the family-wise error rate (P^{FWE}) [125]. Unfortunately, this method is often too conservative to be applied to MRI functional imaging data due to the inherent degree of spatial correlation between neighbouring voxels, which reduces the number of independent observations.

Statistical parametric mapping (SPM), as implemented in the software package SPM8 (http://www.fil.ion.ucl.ac.uk/spm/), was used to address these issues. SPM uses random field theory (RFT) to find the height threshold which gives the required P^{FWE}. RFT relies on the concept of the Euler characteristic (Ec) of an image, which can be thought as the number of clusters above a given statistic threshold [126]. At high thresholds, the expected Ec is considered to be a good approximation of the probability of observing one or more clusters at that threshold by chance alone, that is, E[Ec] ≈ P^{FWE} [126]. In this thesis, the family-wise error rate was set to 0.05 ($P^{\mathrm{FWE}} < 0.05$), from which the associated t-values were used to threshold the gas challenge maps. A clustering threshold of 5 voxels was additionally employed for added robustness. The surviving voxels were then re-assigned their respective VF, VO or VD values.

3.5. Histology and immunostaining

3.5.1. Dye administration and sectioning

After imaging, animals were allowed to recover (~ 20 min.) before an intraperitoneal injection (60 mg/kg) of the hypoxia marker pimonidazole (Hypoxyprobe, USA) was administered. Pimonidazole is an exogenous marker that acts by forming protein adducts in viable hypoxic cells. Twenty nine minutes after, animals received an intravenous injection (12.5 mg/kg) of the fluorescent perfusion marker Hoechst 33342 (Cambridge Bioscience, UK), and were sacrificed 1 minute later. Immediately after, LS174T or SW1222 tumours were excised and snap frozen in isopentane (cooled with liquid nitrogen) and stored at -80 °C, prior to cryosectioning. Care was taken to preserve tumour orientation. Sections of tumour of 10 μm were cut in the same plane as the MRI image acquisition.

3.5.2. Immunostaining

Fluorescence distributions of vascular perfusion, vascular endothelial cells, pericytes and hypoxic regions were obtained. Perfused areas were directly observed via emission of blue fluorescence from Hoechst 33342. Endothelial cells were stained with a rat monoclonal antibody against CD31 (Abcam, UK), revealed with Alexa Fluor-488 (Life Technologies, UK). Pericytes were detected by α-smooth muscle actin (α-SMA) staining with a mouse monoclonal anti-α-SMA (Sigma-Aldrich, UK), revealed with Alexa Fluor-546 (Life Technologies, UK). Staining of hypoxic regions involved the detection of the *in vivo* administered pimonidazole with a rabbit polyclonal anti-pimonidazole (Hypoxyprobe, USA), in turn revealed with Alexa Fluor-488 (Life Technologies, UK). Additionally, haematoxylin and eosin (H&E) staining was performed in immediately adjacent frozen sections to assess tumour morphology.

Fluorescence images were taken on an Axio Imager microscope (Carl Zeiss, UK), using an AxioCam digital colour camera. Images of H&E were collected on a bright-field Zeiss Axioskop2 microscope (Carl Zeiss, UK). Both microscopes were fitted with a motorized stage and used AxioVision software (v. 4.8, Carl Zeiss, UK).

Quantification of immunofluorescence was performed in Matlab software (v. 7.11, The MathWorks, Inc., USA). ROIs were drawn around the total area of the tumour and

images were thresholded to exclude background fluorescence signal. Tumour coverage of each of the fluorescent markers was calculated as the ratio between fluorescent pixels and the total number of pixels within the ROI. Additionally, the percentage of capillaries covered with pericytes was calculated as the ratio between co-localised α-SMA and CD31 fluorescent pixels and the total number of CD31 fluorescent pixels to assess vascular maturation.

4. Characterisation of spontaneous temporal fluctuations in tumour R_2^* and relationship with gas challenge responsiveness

The first study in this thesis investigates the spontaneous oscillatory characteristics of blood oxygenation estimates in SW1222 and LS174T tumours. This chapter first describes a longitudinal study on the dynamics of tumour R_2^* fluctuations at rest, complemented by its relationship with vascular properties inferred from applied gas challenges. Histological assessment of both tumour lines then follows. Finally, the evolution of systemic blood oxygenation, pH, metabolites and dissolved gases as a function of the steps in the experimental protocol is assessed.

4.1. Introduction

The realisation of the potential to reverse the deleterious effects of tumour cycling hypoxia necessarily needs the prior understanding of the hypoxia-related dynamic processes occurring in the tumour microenvironment, which can only be achieved through dedicated research. Cycling hypoxia was described several decades ago [24;36;37], although the pathological sources that result in its manifestation still lack effective treatment strategies.

The protocol of the study described in this chapter was adapted from previous studies [34;41]. However, here it was performed longitudinally and in the SW1222 and LS174T colorectal tumour lines for the first time. Briefly, gradient-echo MRI sequences have been used to estimate variations in blood oxygenation and flow due to the endogenous magnetic properties of haemoglobin and in-flow effects. Additionally, gas mixtures with elevated concentrations of oxygen and/or carbon dioxide (relative to medical air) were used to infer information about tumour vascular functionality and maturation. Please see section 2.2 for a more in depth review.

The initial aim of this study was to investigate the feasibility of using a dynamic GE-MRI sequence to map spontaneous fluctuations in blood oxygenation in SW1222 and LS174T tumours. Comparison of tumour and muscle frequencies of R_2^* oscillation was attempted in order to infer about systemic influences in the tumour. Longitudinal scans were aimed at assessing the evolution of spontaneous fluctuations (dynamics and

distribution) and gas challenge responsiveness with the growing tumour. Moreover, this study aimed to assess if tumour R_2^* spontaneous fluctuations were related to vascular properties, assessed with vasoactive gas challenges, and to histological markers of structure and vascular function and maturation. Finally, the relationship between breathing of air, or other gas mixtures, and variations in systemic blood oxygen saturation, pH, metabolites and dissolved gases was investigated.

This study was conducted in an exploratory fashion, with basis on the aims described above, and where interpretation of the results was predominantly derived from their observation, rather than confirming or rejecting a set of pre-defined hypotheses.

4.2. Materials and methods

4.2.1. Cell culture and imaging protocol

Cells of SW1222 or LS174T tumour lines were grown and injected as described in section 3.2. The relatively rapid growth rate of these tumours (doubling time is 3 to 4 days), combined with the fact that this was a longitudinal study (8 days length), led MR imaging to be initiated at 10 days post injection, instead of the usual 2 weeks in this thesis, to prevent overly large tumours at the end of the study. Each SW1222 (n = 8) or LS174T (n = 8) tumour bearing mouse underwent a 60-minute resting state scan followed by a 60-minute gas challenge scan, as described in section 3.3. One mouse bearing a SW1222 tumour died in the scanner at day 4 but this animal's previous datasets were considered for analysis.

4.2.2. Analysis of resting state maps

4.2.2.1. Percentage and amplitude of resting state fluctuations

Resting state maps were calculated and thresholded following the procedures detailed in section 3.4. For each tumour, quantification of resting state maps was performed for both the percentage of voxels exhibiting R_2^* fluctuations with amplitudes above the uncertainty associated to background noise (standard deviation/uncertainty > 1) and the mean standard deviation (SD) of R_2^* fluctuations corresponding to those voxel locations. A two-way ANOVA followed by Holm-Šídák's multiple comparisons test

was used to assess significance between days of study in the same tumour line and between tumour lines in the same day of the longitudinal study [127].

4.2.2.2. Frequency analysis

Frequencies of R_2^* oscillation of supra-threshold voxels (SD/uncertainty > 1) were assessed with the Lomb method (also known as Lomb-Scargle, Gauss-Vaníček or Least-Squares spectrum) [128;129]. The Lomb method computes the Lomb normalised periodogram (spectral power as a function of angular frequency) of a dataset, h, containing N data points sampled at times t_j using the relation

$$P_N(\omega) = \frac{1}{2\sigma^2}\left(\frac{\left[\sum_j (h_j - \bar{h})\cos\omega(t_j - \tau)\right]^2}{\sum_j \cos^2\omega\,(t_j - \tau)} + \frac{\left[\sum_j (h_j - \bar{h})\sin\omega(t_j - \tau)\right]^2}{\sum_j \sin^2\omega(\,t_j - \tau)}\right) \quad , \qquad \text{Eq. 4.1}$$

where ω is the angular frequency, σ^2 and $\bar{h}$ are the variance and mean of the data, respectively, and τ is an offset constant that allows eq. 4.1 to be invariant to time translation and is defined by [128;129]:

$$\tan 2\omega\tau = \frac{\sum_j \sin 2\omega t_j}{\sum_j \cos 2\omega t_j} \quad . \qquad \text{Eq. 4.2}$$

One of the advantages of the Lomb method over other methods of frequency analysis (e.g. fast Fourier transform (FFT)) is the possibility to easily calculate the statistical significance associated with the power of each frequency. In this context, the null hypothesis is that the data values are independent Gaussian random values. A useful result for the statistical analysis is that the probability distribution of the power at a given frequency is exponentially distributed [129]. Considering $Z = P_N(\omega)$, if M independent frequencies are considered, the probability of obtaining a significant frequency peak, given the null hypothesis is [128;129]:

$$P(Z > z) = 1 - (1 - e^{-z})^M \quad . \qquad \text{Eq. 4.3}$$

The Lomb method has another important advantage relative to FFT methods. If T is the span of the input data $\left(T = \max(t_j) - \min(t_j)\right)$, the sampling frequencies in an FFT are integer multiples of $1/T$. The Lomb method, however, has the ability to (over-) sample more finely than at $1/T$ in order to more accurately identify any frequency peak. This oversampling parameter is typically ≥ 4, and was set to 4 in this study, which means the number of frequency points obtained were 4 times the amount that would have been obtained with an FFT method, in the same range of frequencies.

For each tumour, the Lomb method was applied to individual voxel R_2^* time courses and the resulting spectra were combined into a single average frequency spectrum. The spectral mean and standard deviation of the cohort of SW1222 or LS174T tumours was then computed, independently for each day of study.

To compare tumour and muscle frequencies of R_2^* oscillation, a second cohort of SW1222 (n = 5) or LS174T (n = 3) tumours were used. MR imaging was performed in an orientation encompassing the tumour and the hind leg muscle of the mouse. Imaging and map thresholding were performed as before.

In order to attempt to further resolve frequency peaks, a third group of mice were injected with SW1222 (n = 5) or LS174T (n = 6) tumour cells and imaged at rest (resting state) for 3 hours. With the exception of the length of scan, the imaging parameters were kept constant and the post processing analysis was performed as before.

4.2.3. Analysis of gas challenge maps

Gas challenge maps were calculated and thresholded as detailed in section 3.4. For each tumour, quantification of VF, VO and VD maps was performed for both the percentage of voxels exhibiting a significant ΔR_2^* or ΔSI (positive or negative) and the corresponding mean magnitude values of those voxel locations (absolute values of ΔR_2^* or ΔSI were used to directly compare positive and negative magnitudes). Three different types of group-wise statistical assessments were performed in each of these two quantities:

- Between positive and negative ΔR_2^* or ΔSI (e.g. SW1222 $-\Delta R_2^*$ day 0 vs. SW1222 $+\Delta R_2^*$ day 0), to infer the functionality or maturation state of the perfused vasculature in that tumour type;

- Between different tumour types (e.g. SW1222 $-\Delta R_2^*$ day 0 vs. LS174T $-\Delta R_2^*$ day 0), in which the primary goal was to identify differences in functional or mature vasculature between tumour types, assessed by considering $-\Delta R_2^*$ or $+\Delta SI$ responses. Additionally, it aimed to study the relative occurrence of $+\Delta R_2^*$ or $-\Delta SI$ responses in each tumour type;

- Between 2 different days of the longitudinal study, consecutive or not (e.g. SW1222 $-\Delta R_2^*$ day 0 vs. SW1222 $-\Delta R_2^*$ day 2), aiming to assess the evolution of the response (positive or negative) with the growing tumour.

Differences between groups were assessed with a two-way ANOVA followed by Holm-Šídák's multiple comparisons test. Maps without supra-threshold voxels were defined as having 0% responsive voxels and were considered for analysis of percentage responsiveness. Consequently, in such cases, the ΔR_2^* or ΔSI response was inexistent, and was therefore not considered for analysis of magnitude response.

4.2.4. Relationship between resting state and gas challenge maps

Resting state R_2^* standard deviation maps were correlated with VF, VO and VD gas challenge maps, on a voxel-by-voxel basis, in order to investigate the relationship between resting state fluctuations and vascular properties in SW1222 and LS174T tumours. The values of individual voxels surviving the thresholds in both maps were plotted against each other. One plot was created for each tumour line, each gas challenge and each day of the longitudinal study. In each plot, voxels of all respective tumours were grouped. Pearson's linear correlation was then used to assess the strength and significance of the relationships.

4.2.5. Histological assessment

To compare tumour spontaneous fluctuations with histological markers, a fourth cohort of SW1222 (n = 5) or LS174T (n = 5) tumours were imaged at rest. MR imaging

and post processing were performed as previously described. Upon MR imaging, histology was performed following the protocol detailed in section 3.5. Histology could not be performed on one LS174T tumour due to sample degradation following excision.

4.2.6. Analysis of oxygenation and pH of systemic blood

This part of the experimental protocol was performed in collaboration with Dr. Richard Ong (UCL Department of Neuroscience, Physiology and Pharmacology). Blood samples and pulse oximetry readings were taken to investigate the systemic effects of the MR imaging protocol on blood pH, blood metabolites, dissolved gases and blood oxygen saturation. MRI experimental conditions were reproduced outside of the scanner regarding anaesthesia and normothermia. The resting state and gas challenge protocols were also reproduced as described in section 3.3. Some gas challenge breathing phases lasted a few minutes longer than the proposed 10 minutes due to small delays in changing the gas mixtures. CD1 mice (n = 6, 7 weeks age, 23-27 g) were used instead of CD1 nude mice. Both mouse strains were assumed to exhibit comparable physiological responses to the applied changes. The right common carotid artery was cannulated for arterial blood sampling and arterial blood pressure monitoring. Blood samples were taken at the end of the resting state period and during the course of the gas challenge period to measure pH, metabolites, dissolved gases and oxygen saturation. Simultaneously, arterial haemoglobin saturation was continuously measured using a MouseOx pulse oximeter sensor (Starr Life Sciences Corp., USA) clamped to the right thigh of the animal.

4.3. Results

4.3.1. Spontaneous fluctuations at rest

Figure 4.1 shows, in an example LS174T tumour slice, resting state R_2^* time courses at all voxel locations (Fig. 4.1A) and the corresponding, noise thresholded, standard deviation (SD) map (Fig. 4.1B). Resting state SD maps reflect the degree of R_2^* amplitude of variations with time at each voxel location. Clear temporal variations in R_2^* can be observed, which are heterogeneously distributed within the tumour.

Throughout the longitudinal study, the percentage of voxels spontaneously fluctuating above the noise uncertainty did not significantly change in either tumour line (Fig. 4.2). Between tumour lines, a significant difference was observed at day 4, with LS174T tumours revealing higher percentages of spontaneous fluctuations.

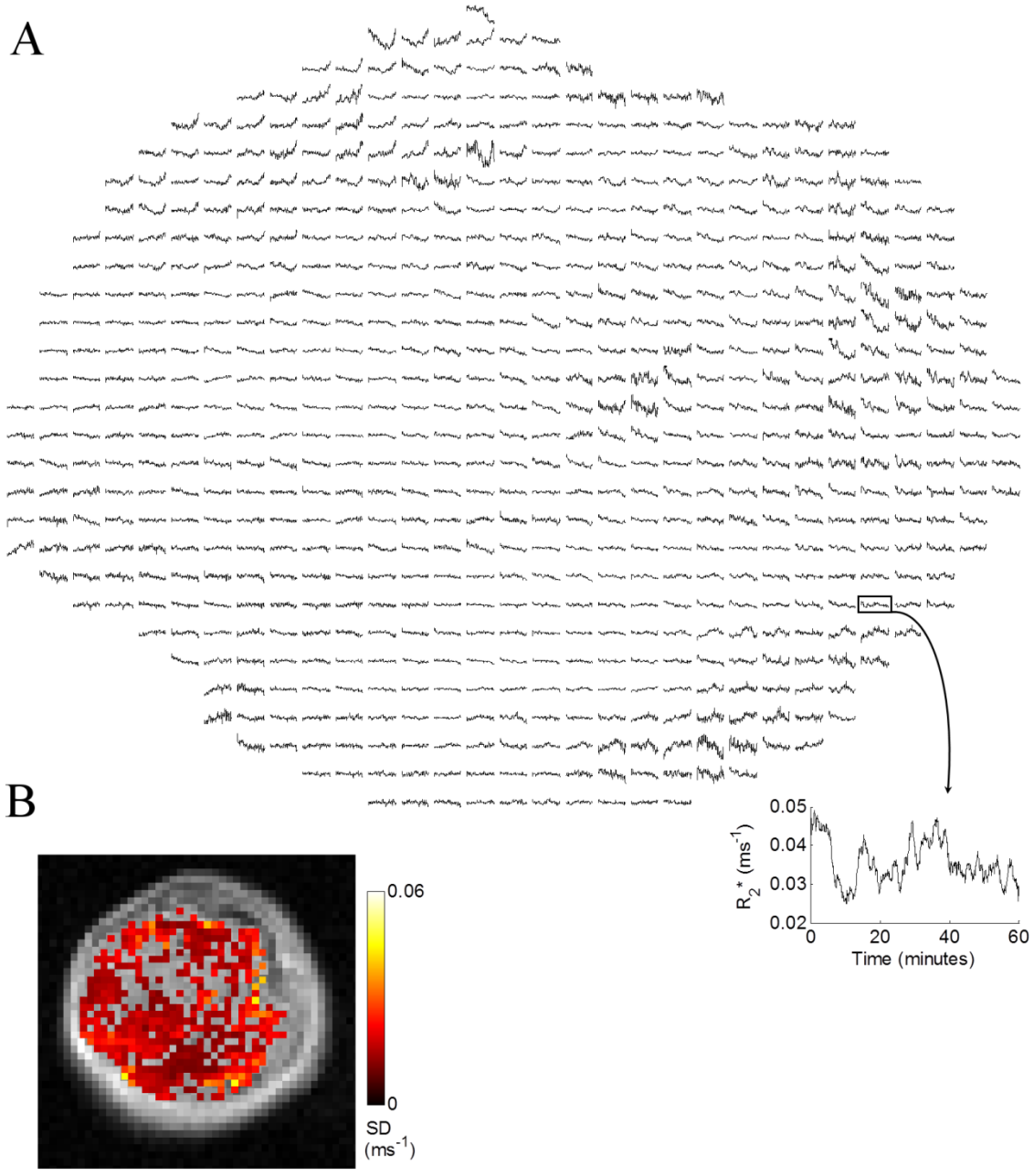

Figure 4.1 – Dynamic R_2^* estimates, at rest, in an example LS174T tumour xenograft. A: 60-minute R_2^* voxel time courses. **B:** Corresponding standard deviation (SD) map of the R_2^* time courses, thresholded to the voxel locations exhibiting fluctuations with amplitudes above the uncertainty associated to background noise. SD values reflect the amplitude of R_2^* fluctuations.

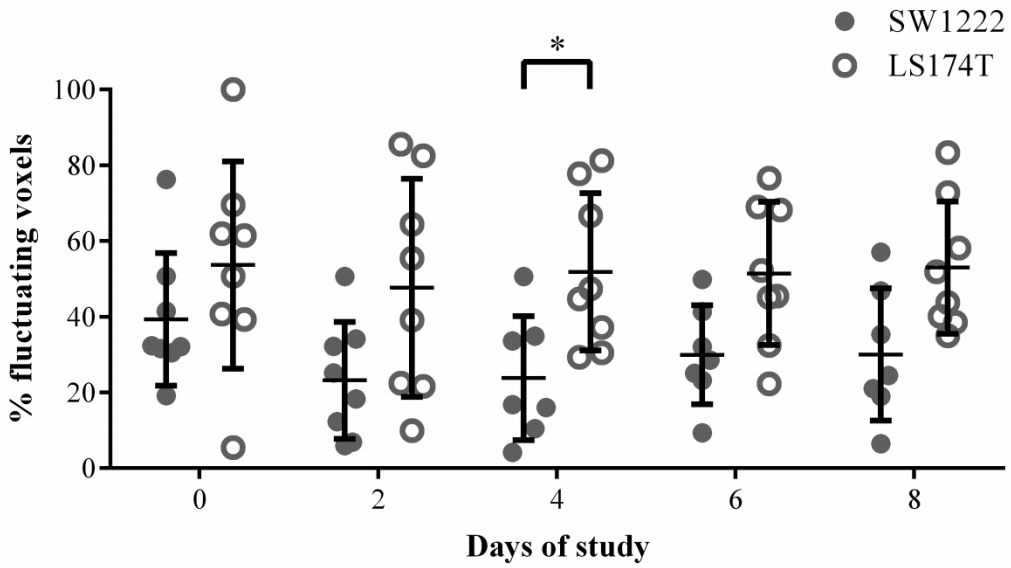

Figure 4.2 – Evolution of the percentage of the tumour volume experiencing R_2^* fluctuations with the tumour growth. Bars represent mean ± SD. A significant difference between tumour lines was identified at day 4 (two-way ANOVA followed by Holm-Šídák's multiple comparisons test). *, $P < 0.05$.

Figure 4.3 illustrates the longitudinal evolution of $SD(R_2^*)$ mean values. As opposed to figure 4.2, no significant differences between tumour lines were observed, although a decrease in the amplitude of R_2^* fluctuations was detected between days 0 and 8 in LS174T tumours. Together, these observations suggest that the percentage of the tumour experiencing spontaneous fluctuations is not coupled with the amplitude of such fluctuations. Additionally, spontaneous fluctuations in SW1222 tumours appear not to depend on the size/stage of the tumour, whereas in LS174T tumours the amplitude of fluctuations was observed to evolve with time.

Figure 4.4 shows the result of a simulation performed to compare the performance of two different methods of frequency analysis: the Lomb method and fast Fourier transform (FFT). A signal composed of six sinusoids at different frequencies and with different amplitudes of oscillation was generated (see Figure 4.4), to which normally distributed random noise was added (noise amplitude = 2 a.u.). With the exception of the lowest frequency (2×10^{-4} Hz), the Lomb method accurately identified all frequency peaks, all being significant ($P < 0.01$).

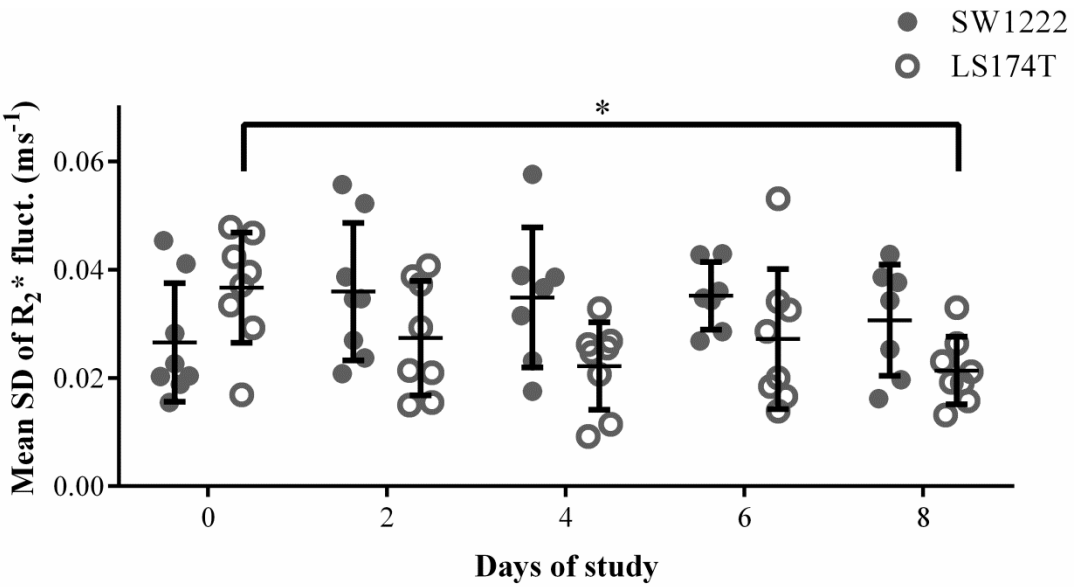

Figure 4.3 – Evolution of the mean standard deviation (SD) of R_2^* fluctuations with the tumour growth. Bars represent mean ± SD. A significant difference was found between days 0 and 8 in LS174T tumours (two-way ANOVA followed by Holm-Šídák's multiple comparisons test). *, $P < 0.05$.

Conversely, the FFT algorithm was considerably less accurate in its estimations, and failed to identify some peaks. The Lomb method also performed better in preserving the inter-peak ratio, meaning it better reflects the true relative amplitudes of the individual sinusoids. Given its superior performance, the Lomb method was chosen to analyse the frequencies of spontaneous R_2^* oscillations.

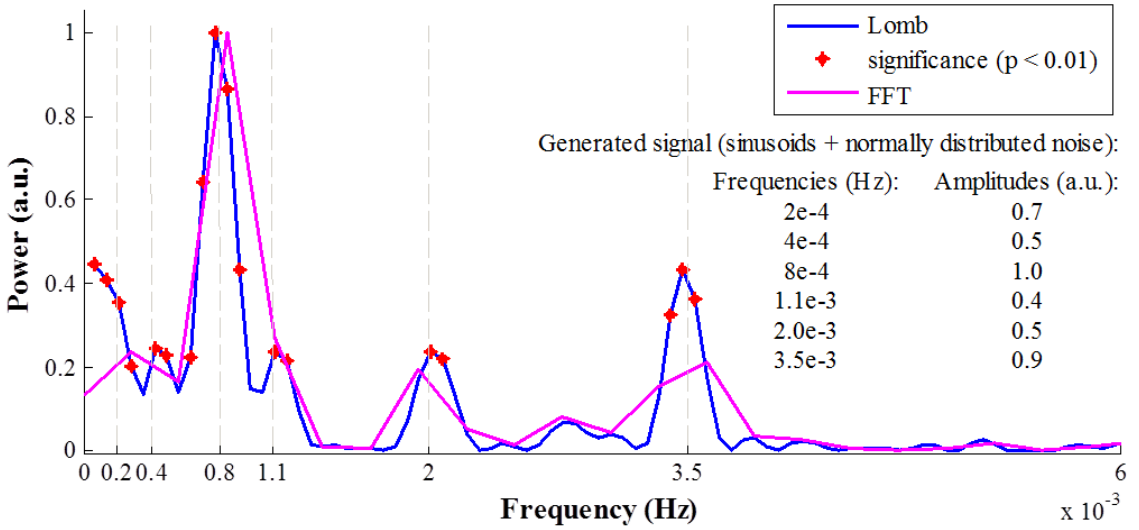

Figure 4.4 - Comparison between FFT (magenta) and the Lomb method (blue) in identifying the oscillatory frequencies of a generated signal. Grey vertical dashed lines represent the generated frequencies. The Lomb method performed better in identifying the frequency peaks of oscillation relative to FFT.

Figure 4.5 illustrates the dominant (peak) frequencies of R_2^* oscillation for all study days and for both tumour lines. Although some variations in the frequency power were observed longitudinally and between tumour types, the dominant frequencies were usually contained in similar [$f_{low} - f_{high}$] low-frequency bands. Frequency peaks were found between f_{low} = 2.1×10^{-4} Hz (≈ 0.76 cycles/hour) and f_{high} = 1.8×10^{-3} Hz to 2.3×10^{-3} Hz (= 6.48 to 8.28 cycles/hour) throughout the study days and between tumour types. However, on two occasions, f_{high} was higher: at day 4 in LS174T tumours (f_{high} = 3.5×10^{-3} Hz = 12.6 cycles/hour) and at day 8 in SW1222 tumours (f_{high} = 2.7×10^{-3} Hz = 9.72 cycles/hour). These results suggest that, in LS174T tumours, the range of dominant frequencies of oscillation is not related to the tumour stage, at least in the time scale studied here. In SW1222 tumours, the same is true until day 6, although at a later stage (day 8) higher frequency peaks were observed.

Comparison between frequencies of R_2^* oscillation between tumour and muscle was equally attempted. Unfortunately, the percentage of muscle voxels exhibiting R_2^* dynamic variations above the noise uncertainty was too low for a comparison to be possible (mean percentage = 0.5%). This is indicative of the low amplitude fluctuations in muscle tissue.

Figure 4.6 shows the frequency spectra for the 3 hour-long resting state scans. SW1222 tumours revealed dominant frequencies between 7×10^{-5} Hz and 1.9×10^{-3} Hz (≈ 0.25 to 6.84 cycles/hour). LS174T tumour frequency peaks ranged from 7×10^{-5} Hz to 1.8×10^{-3} Hz (≈ 0.25 to 6.48 cycles/hour). Scanning for longer periods revealed slower oscillating patterns in both tumour types (≈ 0.25 cycles/hour), whereas the higher frequency peaks are in the range previously observed in figure 4.5.

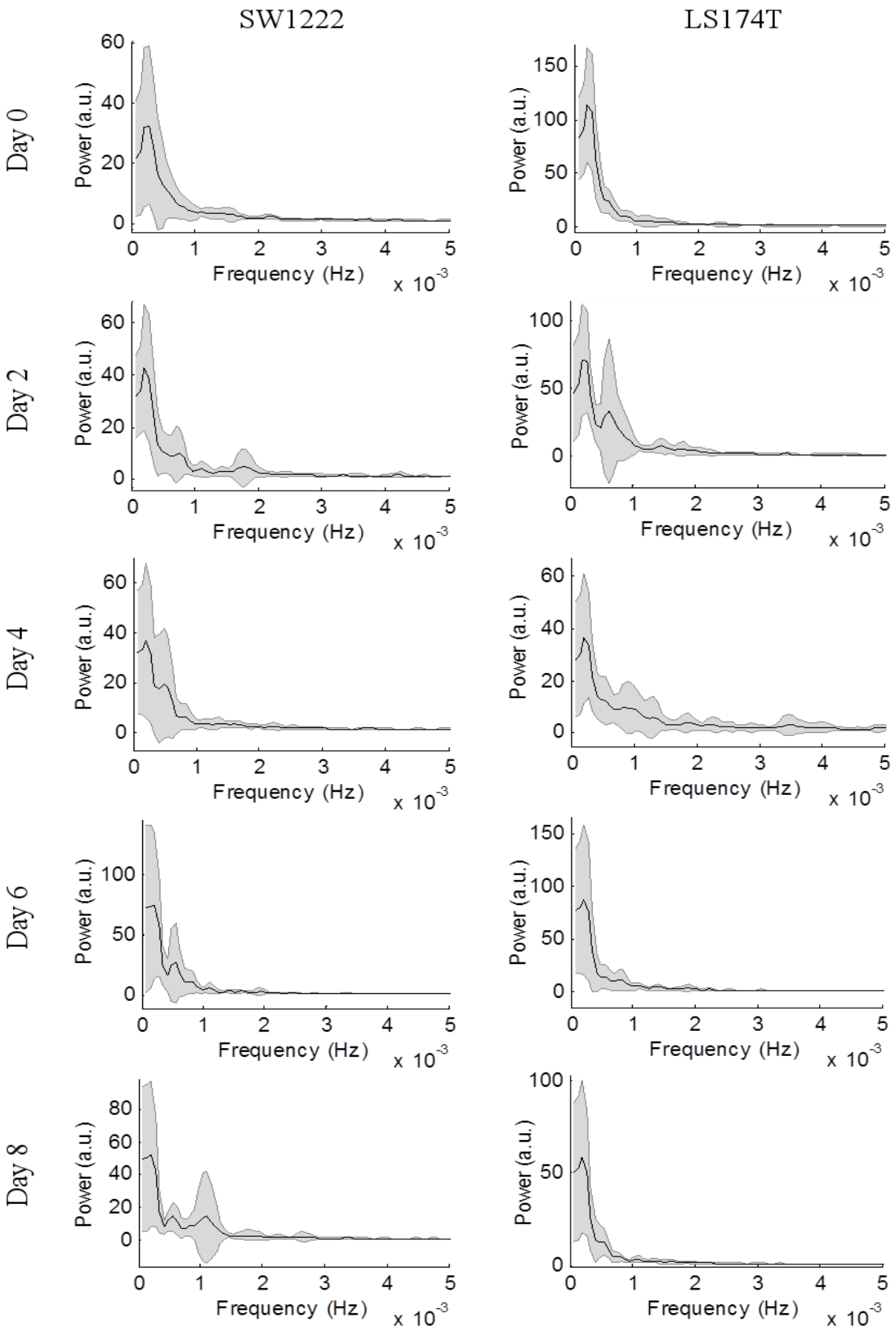

Figure 4.5 – Frequencies of R_2^* oscillation at rest for SW1222 and LS174T tumours. Mean (black line) and standard deviation (shaded area) of power spectra are shown. Dominant frequencies were usually between f_{low} = 2.1×10^{-4} Hz and f_{high} = 1.8 to 2.3×10^{-3} Hz, although at day 4 (LS174T) and day 8 (SW1222) f_{high} was 3.5×10^{-3} Hz and 2.7×10^{-3} Hz, respectively.

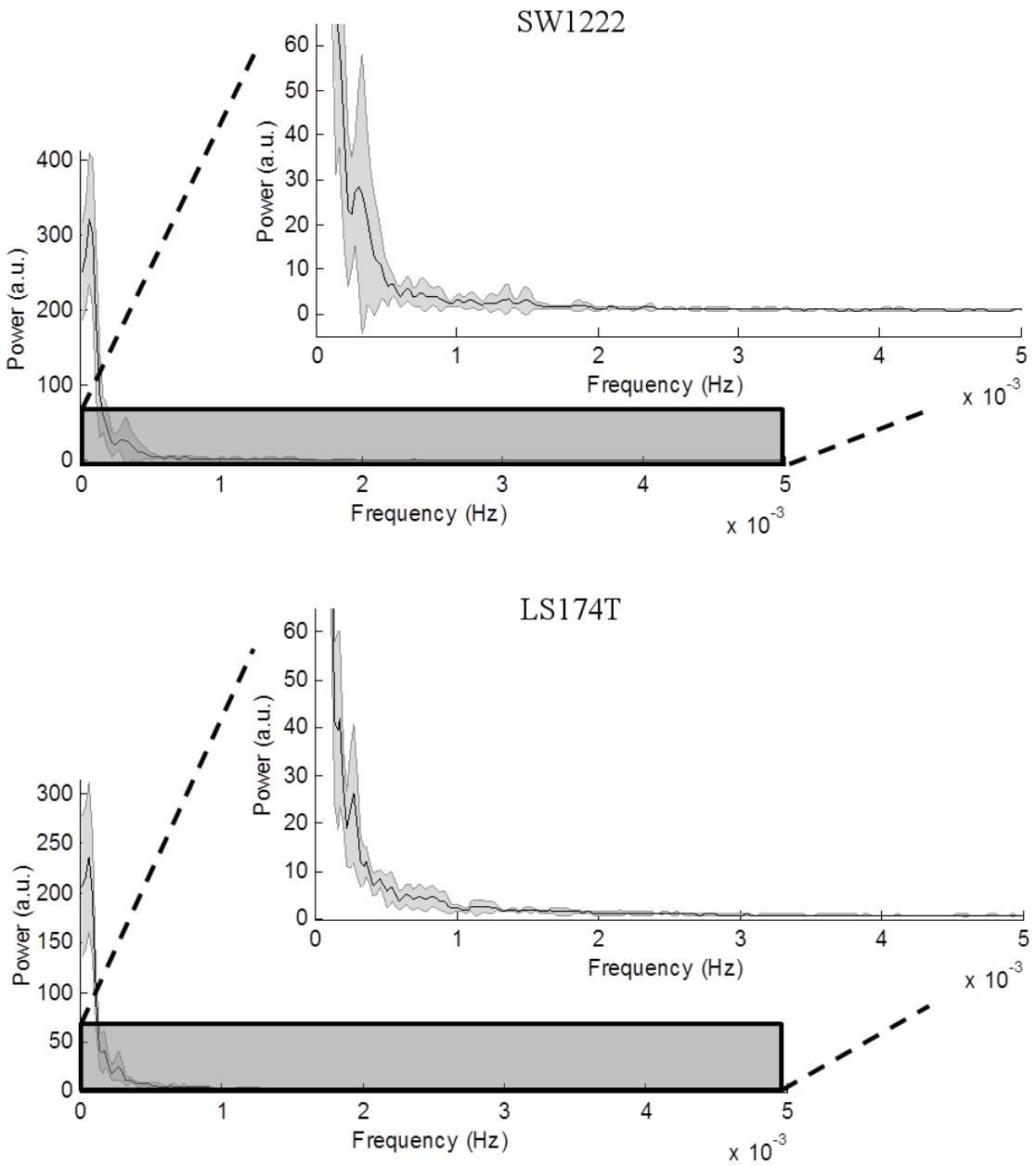

Figure 4.6 – Frequencies of R_2^* oscillation at rest for SW1222 (*n*=5) and LS174T (*n*=6) tumours during 3-hour long acquisitions. Mean (black line) and standard deviation (shaded area) of power spectra are shown. Inset graphs show magnifications of the shaded rectangles. SW1222 tumour dominant frequencies were observed in the low-frequency band of 7×10^{-5} Hz to 1.9×10^{-3} Hz. In LS174T tumours, dominant frequencies were registered between 7×10^{-5} Hz and 1.8×10^{-3} Hz.

4.3.2. Response to hyperoxia challenges

A typical gas challenge voxel time course is shown in figure 4.7A. Hyperoxia (breathing of carbogen or 100% O_2) has the effect of decreasing the relative concentration of paramagnetic deoxyhaemoglobin in the blood of perfused vessels, therefore reducing the relaxation rate R_2^*. This negative ΔR_2^* ($-\Delta R_2^*$) response is the expected effect of switching from air to carbogen or oxygen, which is shown in blue in figure 4.7B. However, positive responses ($+\Delta R_2^*$) can also occur due to not yet fully understood reasons (Fig. 4.7B, red/orange voxels), and a number of possible mechanisms will be debated in Discussion section 4.4.2.

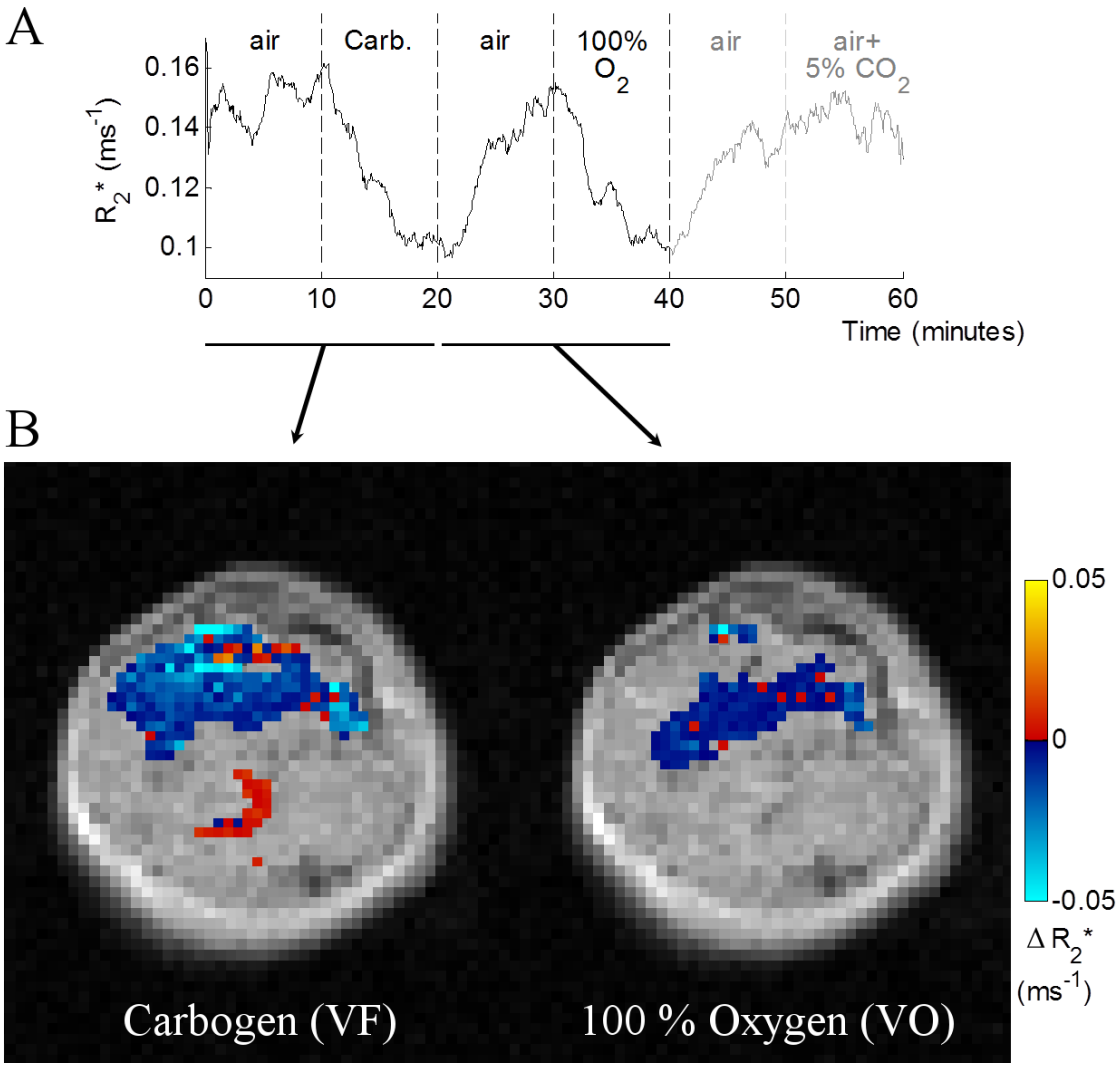

Figure 4.7 – Hyperoxia gas challenge in an example LS174T tumour. A: Single voxel R_2^* time course depicting the variation in R_2^* as a response to the breathing gas. R_2^* estimates were not used for hypercapnia assessment. **B:** Gas challenge spatial maps of vessel functionality with carbogen (VF) or 100% O_2 (VO) in a single slice, calculated from the difference in R_2^* between the hyper-oxygenated gas and air. Maps were thresholded to $P^{FWE} < 0.05$. Voxels surviving the threshold are coloured.

As for the resting state analysis, the percentage of tumour responsive voxels ($-\Delta R_2^*$ or $+\Delta R_2^*$) was assessed for gas challenge data. Figure 4.8A shows the results for carbogen breathing. Negative ΔR_2^* responses were more common than positive ΔR_2^* responses in SW1222 tumours in days 4, 6 and 8. In LS174T tumours, no differences between negative and positive ΔR_2^* prevalence were found. Between tumour types, $-\Delta R_2^*$ responses were predominant in SW1222 tumours on days 4 and 8. SW1222 tumours also showed an increase in the occurrence of $-\Delta R_2^*$ responses between early time points (days 0 and 2) and a late time point (day 8). Figure 4.8B shows the results for 100% O_2 breathing. Here, $-\Delta R_2^*$ responses were more common within SW1222 tumours at day 8. No further significant differences were observed.

Figure 4.9 shows the mean magnitude of ΔR_2^* responses to hyperoxia. Carbogen breathing caused stronger $-\Delta R_2^*$ responses relative to $+\Delta R_2^*$ responses in SW1222 tumours at day 8. No differences were observed between tumour types or study days (Fig. 4.9A). Conversely, the 100% O_2 challenge revealed a reduction in the magnitude of $+\Delta R_2^*$ responses between day 2 and later time points (days 6 and 8) in SW1222 tumours (Fig. 4.9B).

Overall, results show $-\Delta R_2^*$ responses to hyperoxia to be more common and stronger than $+\Delta R_2^*$ responses, but only in SW1222 tumours. Negative ΔR_2^* responses were also more prevalent in SW1222 tumours relative to LS174T tumours. The longitudinal assessment revealed the tumour development to favour the occurrence of $-\Delta R_2^*$ responses and to decrease the strength of $+\Delta R_2^*$ responses in SW1222 tumours.

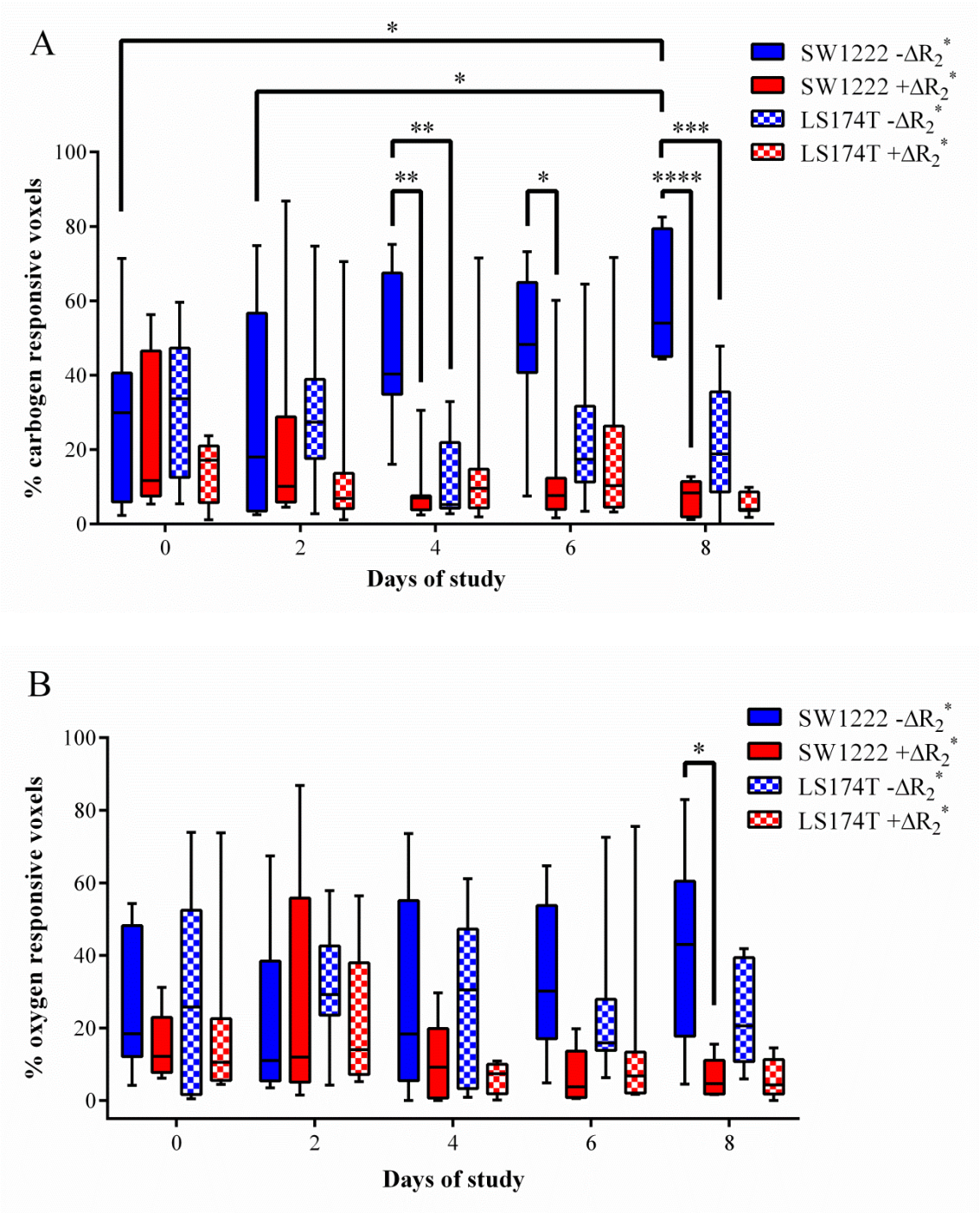

Figure 4.8 – Evolution of the percentage of the tumour volume responsive to carbogen (A) and 100% oxygen (B) gas challenges with the tumour growth. Boxes define the interquartile range, whiskers the 10th and 90th percentile, and central lines the median. Panel A shows three different types of statistical significance: between $-\Delta R_2^*$ and $+\Delta R_2^*$ responses within SW1222 tumours at days 4, 6 and 8; between tumour types regarding the $-\Delta R_2^*$ response at days 4 and 8; between days of study regarding the $-\Delta R_2^*$ response within SW1222 tumours (day 0 vs. day 8 and day 2 vs. day 8). Panel B shows a significant difference between $-\Delta R_2^*$ and $+\Delta R_2^*$ responses within SW1222 tumours at day 8. Significance was tested with a two-way ANOVA followed by Holm-Šídák's multiple comparisons test. *, $P < 0.05$. **, $P < 0.01$. ***, $P < 0.001$. ****, $P < 0.0001$.

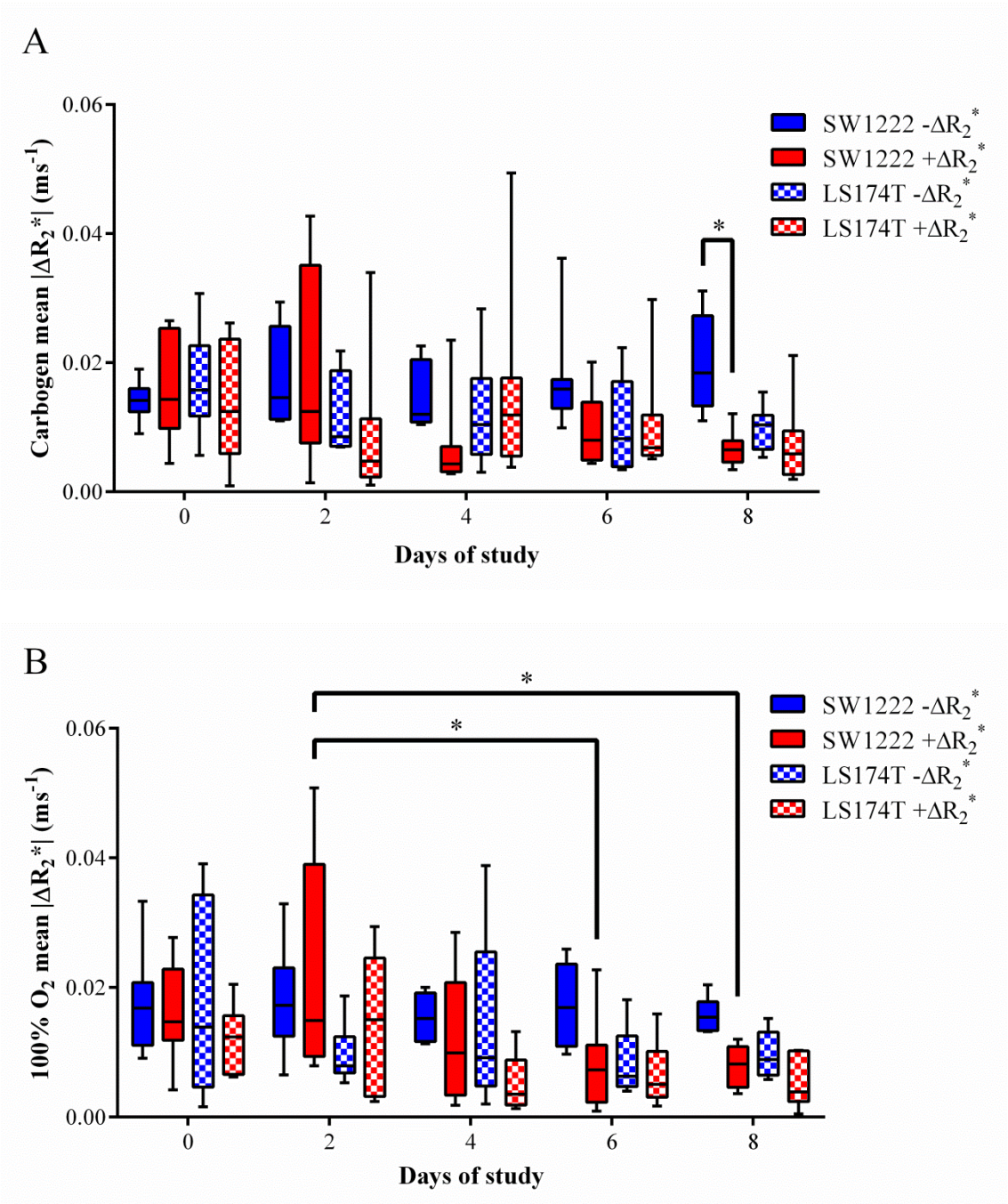

Figure 4.9 - Evolution of the magnitude of tumour response ($|\Delta R_2^*|$) to carbogen (A) and 100% oxygen (B) gas challenges with the tumour growth. A significant difference between $-\Delta R_2^*$ and $+\Delta R_2^*$ responses to carbogen was observed within SW1222 tumours at day 8 (panel A). Between days of study, significant differences were observed in the $+\Delta R_2^*$ response to 100% oxygen within SW1222 tumours (panel B, day 2 vs. day 6 and day 2 vs. day 8). Significance was tested with a two-way ANOVA followed by Holm-Šídák's multiple comparisons test. *, $P < 0.05$.

4.3.3. Response to hypercapnia challenge

Figure 4.10A shows a single voxel time course depicting increased signal intensity (SI) upon changing from breathing air to air + 5% CO_2 (hypercapnia) due to in-flow effects. Figure 4.10B shows the corresponding spatial map exhibiting clusters with a similar response. This $+\Delta SI$ response is the expected effect of a hypercapnia challenge in mature vessels. However, and similarly to hyperoxia, responses with opposite-to-expected signal change also occur $(-\Delta SI)$, which may be due, at least in part, to similar mechanisms (see Discussion section 4.4.2).

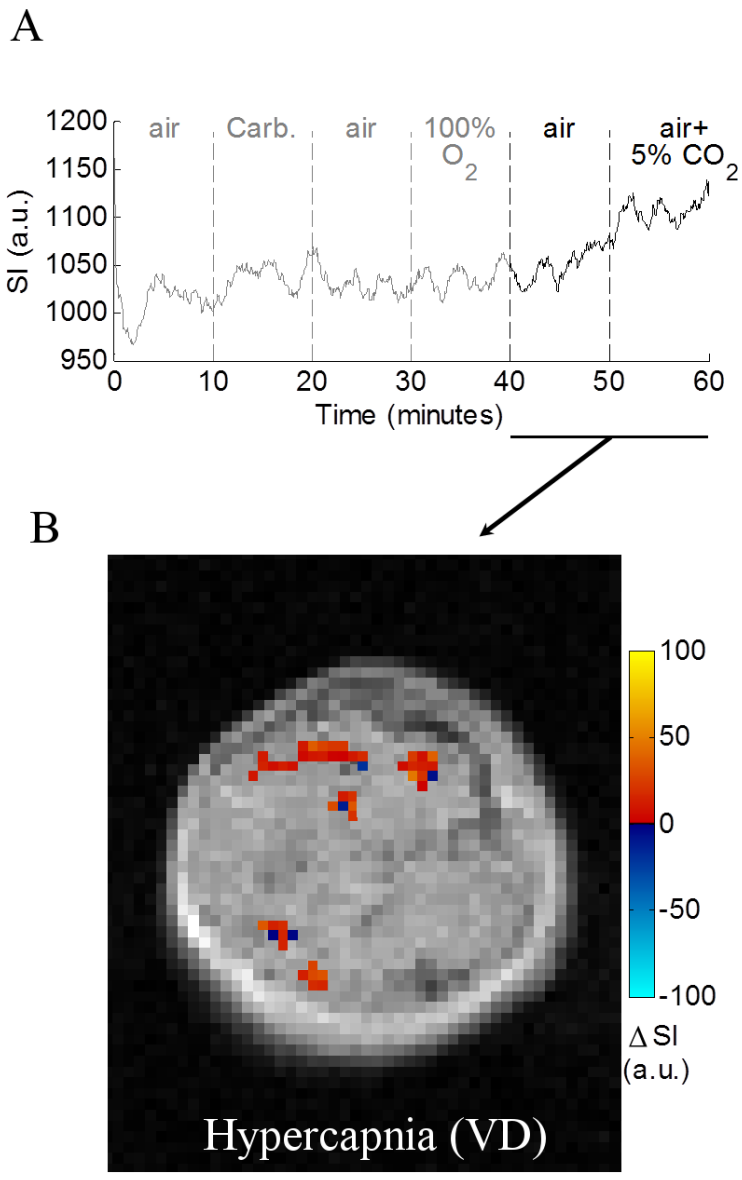

Figure 4.10 – Hypercapnia gas challenge in an example LS174T tumour. A: Single voxel SI time course depicting the variation in SI (or not) as a response to the breathing gas. SI measurements were used exclusively to assess hypercapnia response. **B:** Gas challenge spatial map of vessel maturation (VD) in a single slice, calculated from the difference in SI between hypercapnia and air. Coloured voxels survived $P^{FWE} < 0.05$.

Figure 4.11 shows the percentage of tumour responsive voxels to hypercapnia. SW1222 tumours showed, in day 4, higher percentages of $+\Delta SI$ responses relative to $-\Delta SI$ responses and to LS174T tumours. No longitudinal differences were observed. Additionally, figure 4.12 did not reveal significant effects of any kind in the mean magnitude of ΔSI responses.

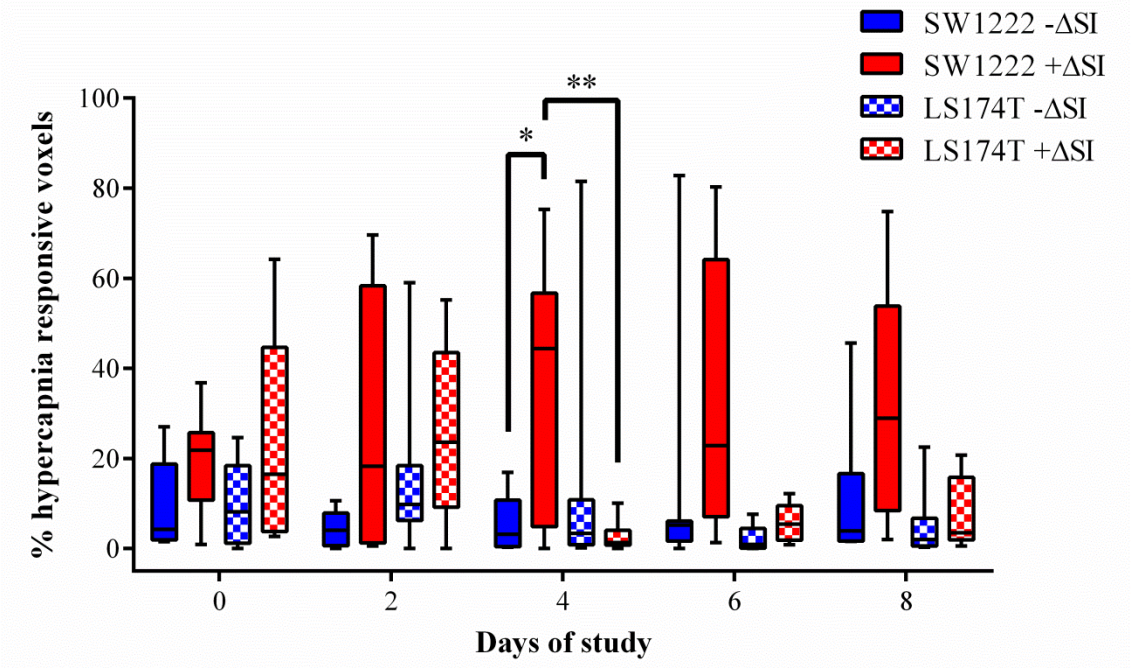

Figure 4.11 – Evolution of the percentage of the tumour volume responsive to the hypercapnia challenge with the tumour growth. At day 4, SW1222 tumours revealed a significant difference between positive and negative responses. Also at day 4, the percentage of voxels with positive response was significantly different between tumour types (two-way ANOVA followed by Holm-Šídák's multiple comparisons test). *, $P < 0.05$; **, $P < 0.01$.

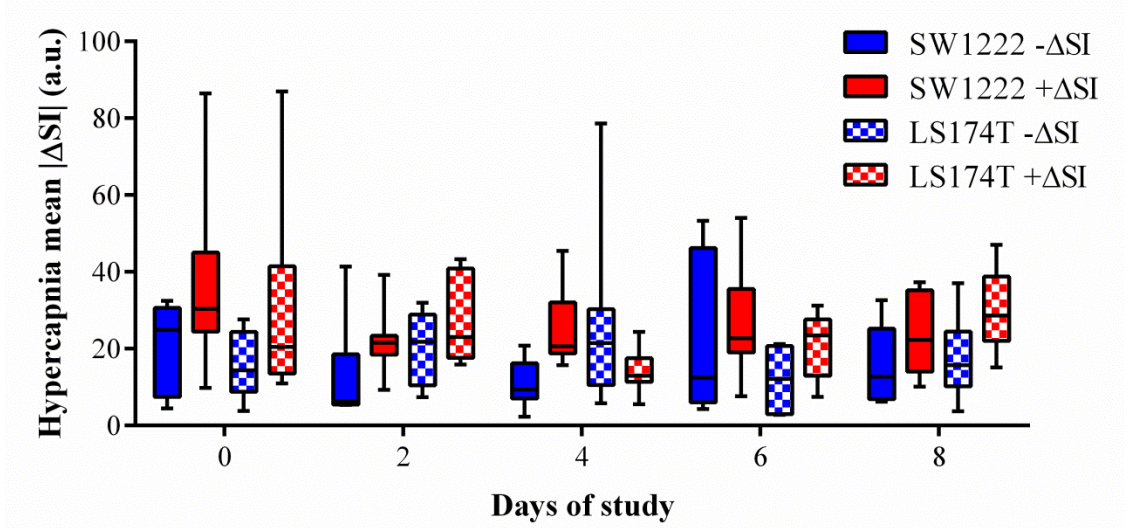

Figure 4.12 - Evolution of the magnitude of tumour response (|ΔSI|) to the hypercapnia challenge with the tumour growth. No significant differences were observed between days of study, tumour type or response signal within the same tumour type (two-way ANOVA followed by Holm-Šídák's multiple comparisons test).

4.3.4. Relationship between spontaneous fluctuations and gas challenge responsiveness

Correlation between resting state R_2^* SD and carbogen ΔR_2^* magnitude responses is exemplified in figure 4.13 for SW1222 and LS174T tumours at day 0. Table 4.1 extends the same analysis to all study days. Generally, correlations were significant although with weak correlation coefficients. A similar result was observed for the correlations between resting state R_2^* SD and 100% oxygen ΔR_2^* (table 4.2). This suggests a weak association between spontaneous fluctuations and vessel functionality, although it might still be influenced by any remaining uncertainty not accounted for in the map thresholding process.

Although still not very strong, more suggestive correlations were found in a few instances. In LS174T tumours, $-\Delta R_2^*$ responses to carbogen breathing in day 0 and to 100% O_2 breathing in day 2 revealed stronger associations: r^2 = 0.53 and r^2 = 0.44, respectively. Interestingly, $+\Delta R_2^*$ responses to carbogen in day 2 (in LS174T tumours) and to 100% O_2 in day 0 (in SW1222 tumours) also revealed higher correlation coefficients: r^2 = 0.54 and r^2 = 0.42, respectively. Additionally, the existence of longitudinal trends was investigated, i.e., from day 0 to day 8 within the same tumour line and response type (positive or negative). No longitudinal trends were observed in carbogen or 100% O_2 breathing.

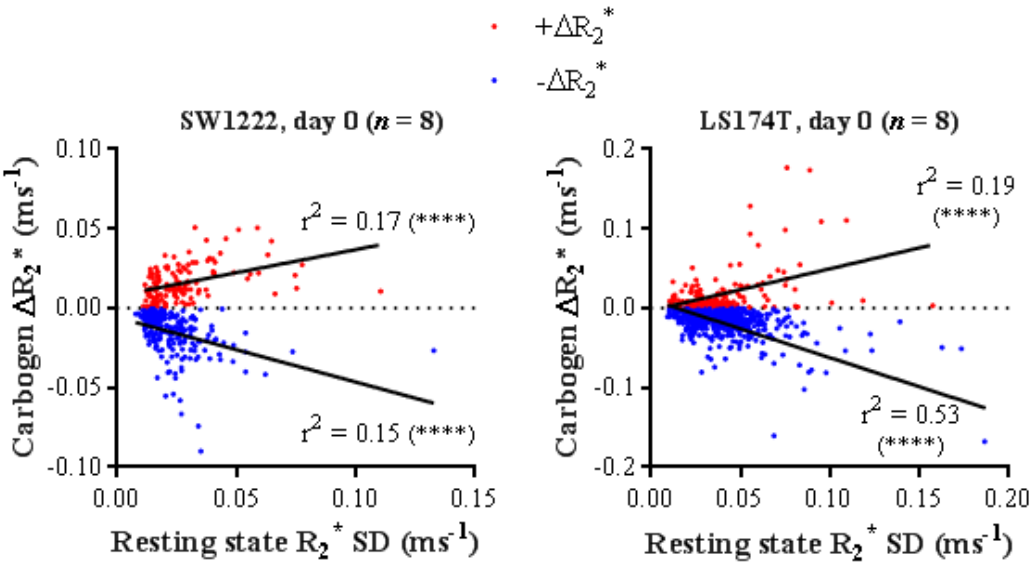

Figure 4.13 – Voxel-wise correlation between resting state R_2^* standard deviation (SD) and carbogen ΔR_2^*, at day 0, in SW1222 (left) and LS174T (right) tumours. Dots represent individual tumour voxels. ****, P < 0.0001 (Pearson's linear correlation).

Table 4.1 – Pearson's linear correlation (r^2, *P*-value) between resting state R_2^* standard deviation and carbogen ΔR_2^* in SW1222 and LS174T tumours. Significant correlations are common, although generally with weak correlation coefficients. ****, $P < 0.0001$.

r^2	SW1222		LS174T	
	$-\Delta R_2^*$	$+\Delta R_2^*$	$-\Delta R_2^*$	$+\Delta R_2^*$
Day 0	0.15 ****	0.17 ****	0.53 ****	0.19 ****
Day 2	0.16 ****	0.22 ****	0.28 ****	0.54 ****
Day 4	0.35 ****	0.21 ****	0.32 ****	0.33 ****
Day 6	0.29 ****	0.38 ****	0.22 ****	0.16 ****
Day 8	0.24 ****	0.23 ****	0.36 ****	0.12 ****

Table 4.2 – Pearson's linear correlation (r^2, *P*-value) between resting state R_2^* standard deviation and 100% O_2 ΔR_2^* in SW1222 and LS174T tumours. Mostly significant correlations were observed, although weak correlation coefficients are common. ns, $P > 0.05$ (non-significant). *, $P < 0.05$. **, $P < 0.01$. ****, $P < 0.0001$.

r^2	SW1222		LS174T	
	$-\Delta R_2^*$	$+\Delta R_2^*$	$-\Delta R_2^*$	$+\Delta R_2^*$
Day 0	0.11 ****	0.42 ****	0.15 ****	0.06 ****
Day 2	0.25 ****	0.36 ****	0.44 ****	0.22 ****
Day 4	0.36 ****	0.07 ****	0.16 ****	0.23 ****
Day 6	0.17 ****	8×10^{-8} ns	0.37 ****	0.27 ****
Day 8	0.19 ****	0.08 *	0.16 ****	0.21 ****

Table 4.3 shows the results of the correlation between resting state R_2^* SD and hypercapnia ΔSI magnitude responses. A great number of poor correlations were observed, with some even lacking statistical significance. Of all, only $-\Delta SI$ responses in SW1222 tumours at day 2 approached a noticeable degree of association with the SD of spontaneous fluctuations ($r^2 = 0.51$). Longitudinal trends alongside the study days were also investigated, although no trends were observed.

Table 4.3 – Pearson's linear correlation (r^2, *P*-value) between resting state R_2^* standard deviation and hypercapnia ΔSI in SW1222 and LS174T tumours. Significant and non-significant correlations were observed, mostly with weak correlation coefficients. ns, $P > 0.05$ (non-significant). *, $P < 0.05$. **, $P < 0.01$. ***, $P < 0.001$. ****, $P < 0.0001$.

r^2	SW1222		LS174T	
	$-\Delta SI$	$+\Delta SI$	$-\Delta SI$	$+\Delta SI$
Day 0	0.04 *	0.003 ns	6×10^{-4} ns	0.13 ****
Day 2	0.51 ***	0.05 **	0.009 ns	0.05 ****
Day 4	0.18 ****	0.009 ns	0.02 ns	0.19 ***
Day 6	0.17 ****	0.002 ns	8×10^{-4} ns	0.03 *
Day 8	0.06 *	0.11 ****	0.006 ns	0.007 ns

4.3.5. Histological markers and their relationship with spontaneous fluctuations

Fluorescently labelled tumour sections revealed significant differences between tumour types, with SW1222 tumours showing a more extensive vascular network (from endothelial cell staining), which was better perfused and less hypoxic than in LS174T tumours (Figs. 4.14A, 4.15A and 4.15B). These observations are in agreement with previous studies by El-Emir *et al.* [117] and Pedley *et al.* [120]. Furthermore, visual inspection of H&E sections confirmed the different morphology of each tumour line, with SW1222 tumours showing better differentiation into glandular structures, which is in agreement with previous literature (Fig. 4.15C) [119]. The percentage of pericyte coverage in the tumours, alongside the degree of pericyte attachment to tumour blood vessels (% mature vessels), was not significantly different between tumour types (Fig. 4.14A and B).

In tumour sub-regions with high R_2^* SD, tissues were well perfused and viable (non-necrotic) in all SW1222 ($n = 5$) and LS174T ($n = 4$) tumours (examples in Fig. 4.15B, C and D). Mature and immature blood vessels were homogeneously distributed in both tumour types, suggesting spontaneous fluctuations in these tumours can occur regardless of the presence of pericyte coverage of the tumour vessels.

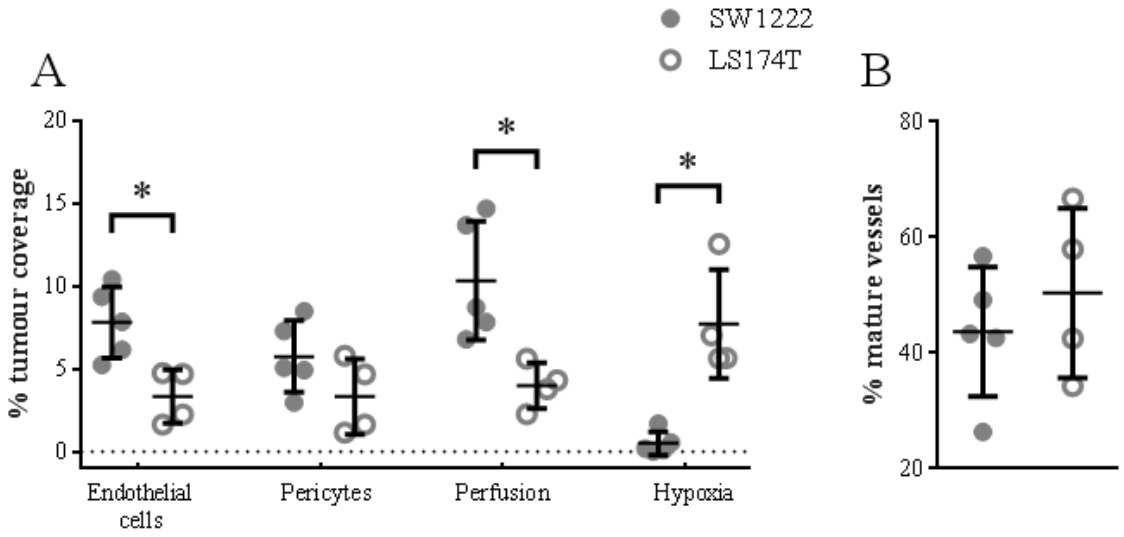

Figure 4.14 – Quantitative fluorescence histology in SW1222 (*n* = 5) and LS174T (*n* = 4) tumour xenografts. A: Percentage tumour coverage of endothelial cells, pericytes, perfusion and hypoxia. **B:** Percentage of blood vessels covered with pericytes. Bars represent mean ± SD. SW1222 tumours have significantly higher vascular density and are better perfused and less hypoxic than LS174T tumours (Mann-Whitney *U*-test). No difference was found in the percentage of pericytes or in its coverage of blood vessels between both tumour types (Mann-Whitney *U*-test). *, $P < 0.05$.

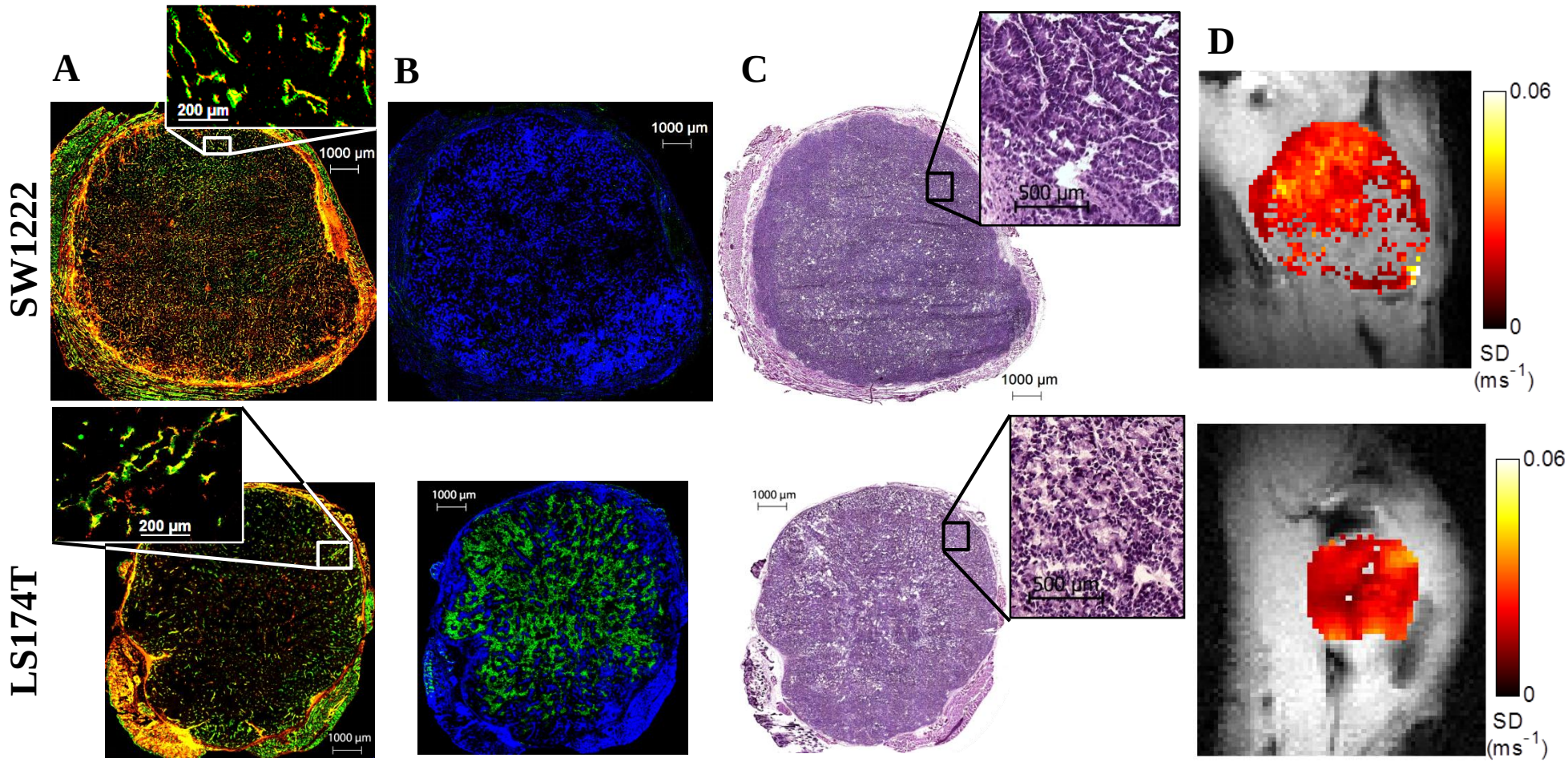

Figure 4.15 – Histology in example SW1222 and LS174T tumour xenografts and comparison with MRI data. A: Double staining with CD31 (endothelial cells, green) and α-SMA (mature vessels, red). Insets show blood vessels covered with pericytes (yellow). **B:** Double staining with Hoechst 33342 (perfusion, blue) and pimonidazole (hypoxia, green). **C:** Morphology (H&E) showing moderate-to-well differentiated tissue into glandular structures in the SW1222 tumour and poorly differentiated tissue in the LS174T tumour. **D:** Corresponding resting state maps of R_2^* SD.

4.3.6. Oxygenation and pH of systemic blood

Alternate breathing of different gas mixtures can cause blood pH variations. This effect can further influence the oxygenation status of the blood due to the Bohr effect, which states that haemoglobin's oxygen binding affinity is inversely related to acidity [130]. Therefore, blood pH can also affect R_2^* estimations. Blood sampling allowed the measurement of pH, dissolved gases, oxygen saturation and some metabolites.

Figure 4.16A shows the pH variation throughout the experimental protocol. At the end of the resting state period, pH values were within the reference range (7.350 – 7.450). Carbogen (70 – 85 min., ΔpH = -0.11) and hypercapnia (130 – 140 min., ΔpH = -0.16) caused pH decreases relative to the resting state pH, due to increased CO_2 content (5% in both, see figure 4.16B). This mechanism is shown in equations 4.4 and 4.5, where the concentration of hydrogen ions ($[H^+]$) depends on the concentration of dissolved CO_2. Higher $[H^+]$ causes pH decrease:

$$CO_2 + H_2O \rightleftharpoons H_2CO_3 \rightleftharpoons HCO_3^- + H^+ \quad , \qquad \text{Eq. 4.4}$$

$$pH = -\log[H^+] \quad , \qquad \text{Eq. 4.5}$$

where H_2CO_3 is carbonic acid and HCO_3^- is the bicarbonate ion, which is alkalotic, and its concentration throughout the protocol is shown in figure 4.16C. Conversely, the second air breathing phase (85 – 100 min., ΔpH = +0.11) caused blood alkalosis, which was then inverted with 100% O_2 breathing (100 – 115 min., ΔpH = +0.04).

Figure 4.16D shows similar blood saturation (O_2sat) levels between pulse oximetry and blood sampling, with a mean discrepancy of 1.1% between them. The trend of both measurements also follows the same pattern along the different time points, meaning the relative differences are maintained approximately constant. Hyperoxia challenges (carbogen and 100% O_2) naturally caused the greatest O_2sat values. Conversely, hypercapnia registered the lowest O_2sat, probably due to the Bohr effect.

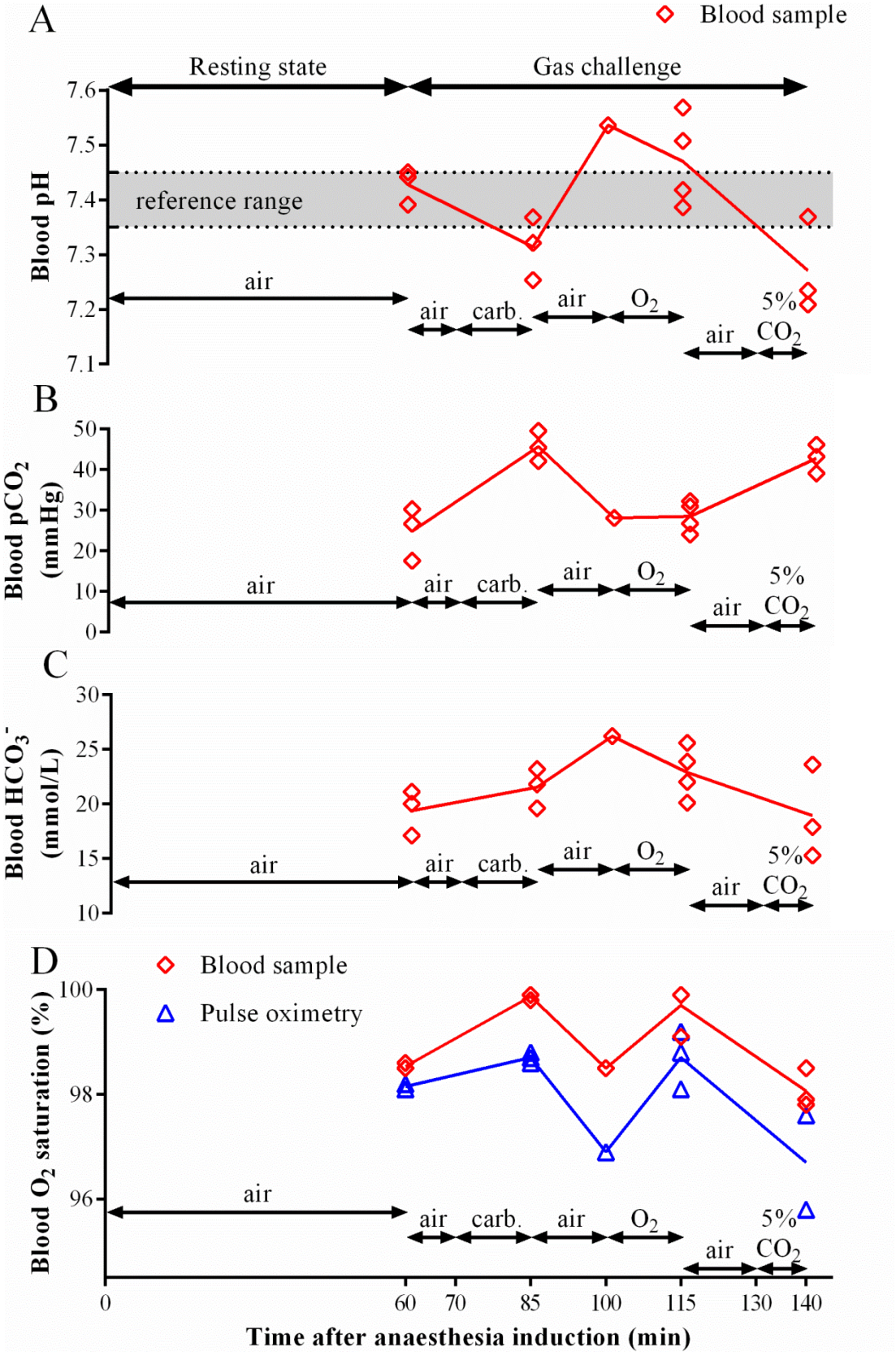

Figure 4.16 – Blood gas analysis and pulse oximetry. A: pH variation with the different breathing gas mixtures. **B:** CO_2 partial pressure. **C:** Bicarbonate ion concentration. **D:** Comparison between blood sample and pulse oximetry readings regarding systemic oxygen blood saturation. Blood samples were taken at the end of the gas breathing periods, immediately before changing the breathing gas mixture. Solid lines connect the mean values at each time point.

4.4. Discussion

4.4.1. Detection of spontaneous fluctuations at rest

Spontaneous fluctuations in R_2^* above noise uncertainty were observed in 60-minute dynamic MRI scans in SW1222 or LS174T colorectal tumour xenografts. The presence of fluctuations was confirmed by the identification of frequency peaks in power spectra. Fluctuating frequencies were usually found between f_{low} = 0.76 cycles/hour and f_{high} = 6.48 to 8.28 cycles/hour between tumour types and study days. These oscillatory periods are in a similar interval to those observed by several groups in a range of mouse [34;82;87], rat [23;25;84], canine [93], human xenograft [91;92] and human [83] tumours. In two occasions, however, peaks of higher frequency were detected: 12.6 cycles/hour in LS174T tumours at day 4, and 9.72 cycles/hour in SW1222 tumours at day 8. Frequencies of this periodicity are not uncommon [34;82;83;92], but represent a deviation from the observed range in these tumours and can possibly reflect an alteration of the microenvironmental processes governing tumour blood flow variations.

Also at day 4, LS174T tumours presented a higher percentage of fluctuating voxels relative to SW1222 tumours. Additionally, the amplitude of fluctuations significantly decreased between days 0 and 8 in LS174T tumours. These differences were probably not due to the experimental setup or the quality of the data, which were identical throughout the study. Regarding the observation at day 4, it should be stressed that it occurred only between tumour types, and was not a longitudinal effect in either SW1222 or LS174T tumours. One possible explanation for the observation of such difference relies on the markedly different phenotype of these tumours, specifically their vascular properties, in which perfusion status may vary in different ways. Another reason might be due to the statistical test itself, where a small relative variation in the percentage of oscillating voxels between tumour types resulted in a significant result, even if there was not a longitudinal variation in each individual tumour line. Conversely, the variation between days 0 and 8 in LS174T tumours suggests that longitudinal effects can occur in these tumours. This result may be a confounder in interpreting variations in spontaneous fluctuations in the case of studies aimed at targeting the tumour vasculature, if the study length is 8 days or more.

In addition to the 60-minute scans, three-hour long resting state scans were also undertaken to resolve low-frequency peaks in the frequency spectra. These longer scanning times enabled lower frequency oscillations of 0.25 cycles/hour (or higher) to

be detected. Fluctuating periods in this range have not yet been specifically reported in tumours, possibly because continuous acquisition protocols do not usually exceed 80 minutes. This result is indicative of the potential of long scanning sessions in uncovering slower periodicities of oscillation, as an alternative to increased sampling frequency.

Muscle R_2^* dynamic variations did not generally present high enough amplitude to overcome the background noise uncertainty threshold, which is indicative of the comparatively larger amplitude fluctuations in tumours. Braun *et al.* [35] made a similar observation between tumour and muscle pO_2 using recessed-tip oxygen microelectrodes. Muscle fluctuations were previously observed in T_2^*-weighted gradient-echo images [34], and so it is conceivable that R_2^* variations might also be occurring, although not entirely detectable with the sequence implemented here. Low amplitude fluctuations in the muscle could suggest the influence of systemic variations in the tumour is minor, however, this is a rather simplistic approach, and more studies in this regard are needed before a conclusion can be made.

Tumour regions of high resting state R_2^* amplitude variation were located in vascularly perfused and viable areas in both tumour types, as assessed by CD31, Hoechst 33342 and H&E immunoreactivity. A similar observation was made by Baudelet *et al.* [34;41] in T_2^*-weighted images of fibrosarcomas. This result is as would be expected, given there will only be dynamic changes in blood flow, and consequently oxygenation, in blood vessels that are perfused, even if this perfusion occurs in a transient fashion, as it is characteristic of solid tumours.

Following a qualitative assessment, some evidence was found for a longitudinal re-distribution of local high amplitude R_2^* oscillations, especially in SW1222 tumours, which represents an important observation in further characterising the evolution of the tumour microenvironment. Still, an accurate assessment of such evolution would have to include a computational registration step to insure the same tumour regions were being compared between different days.

In SW1222 tumours, given the small percentage of hypoxic areas, the observed R_2^* fluctuations might not correspond to cycling hypoxia, but possibly to an oscillation in the blood oxygenation which is regularly above 10 mmHg. In fact, spontaneous fluctuations in pO_2 were previously observed to occur in syngeneic mouse liver tumours regardless of the basal oxygenation state [87]. If true, delivery of systemically applied

therapies would still be hindered due to the oscillatory behaviour, but radiotherapeutic treatments would potentially be more effective than in LS174T tumours.

No clear spatial relationship was observed between the amplitude of spontaneous fluctuations and vessel maturation/immaturity. Pericyte coverage was not preferentially located in specific tumour sub-regions, suggesting it is not essential nor it impairs spontaneous fluctuations. Therefore, vasomotion of mature vessels could be partially responsible for generating dynamic changes in blood flow and oxygenation in these tumours. In fact, Baudelet *et al.* [41] reported that the majority of fluctuating tumour areas was immature, but that mature regions also presented high incidence of fluctuations. Previously, also Dewhirst *et al.* [23] found a relationship between vasomotion and flow oscillations in rat mammary tumours. Spontaneous fluctuations in blood flow and oxygenation in SW1222 and LS174T tumours are thus potentially induced by a combination of structural vascular abnormalities and muscularly-induced vascular contraction and dilation cycles.

4.4.2. Tumour response to hyperoxia

Vasoactive gas challenges have been used in numerous tumour studies because they enable inferences to be drawn about vascular properties [41;49;110;131-136] and about the possible outcome of antitumour treatment strategies [49;110;137-139]. One aim of this longitudinal hyperoxic challenge (carbogen or 100% oxygen) was to infer the evolution of tumour vascular function within the growing tumour, by assessing the strength and prevalence of R_2^* decrease responses ($-\Delta R_2^*$). Discrimination between tumour types was also sought, as well as between types of response ($-\Delta R_2^*$ *vs.* $+\Delta R_2^*$) to infer about the functionality state of the perfused vasculature.

Negative $-\Delta R_2^*$ responses to hyperoxia, the anticipated response type due to decrease of paramagnetic deoxyhaemoglobin concentration, were observed in SW1222 and LS174T tumours, indicating regions of functional vasculature. Conversely, other tumour areas presented R_2^* step increase responses ($+\Delta R_2^*$). Despite having been reported before [49;104;111;112;131;140-142], the mechanisms behind this contradictory response are not yet fully understood. In the case of carbogen breathing, which improves both blood flow and oxygenation, several mechanisms can be occurring. Two possible effects are vascular steal from the surrounding vasculature or

intratumoral vascular steal [49;104;108;111;112;131;140-142]. These effects consist of an increase in blood flow in the host vasculature or in a localised tumour region, respectively, due to CO_2-induced vasodilation. This causes blood to be diverted from tumour regions that have no compensatory vasoactive mechanisms [104], leading to a decrease in oxygenation in those areas and consequent R_2^* increase. In addition, a vasoactive challenge that improves blood flow is likely to be associated with a blood volume increase [108]. If this effect occurs in the feeding arterioles containing partially desaturated blood, the net effect could be of an increase in deoxyhaemoglobin concentration. Moreover, especially in hypoxic tumours, increased blood flow may not decrease the blood desaturation if the fraction of oxygen extraction increases. Consequently, even under improved oxygen delivery, it is the balance between changes in blood flow, blood volume and oxygen utilisation that will decide which way the R_2^* shifts [108].

Robinson *et al.* [104] suggested that T_2^*-weighted GE decreases upon carbogen breathing (reflecting a similar effect to R_2^* increases) could also be due to a decrease in perfusion, resulting from the oxygen-induced vasoconstriction, should the CO_2-induced vasodilation not be of sufficient magnitude to overcome the oxygen effect. If this is the case, it makes sense that vasoconstriction could also occur with 100% O_2 breathing, where vascular dilation will not happen and the accumulation of deoxyhaemoglobin in the affected regions will be even greater.

Growth of SW1222 tumours favoured an increase in $-\Delta R_2^*$ percentage responsiveness to carbogen. This behaviour occurred potentially due to the well-known fact that tumours need to recruit blood vessels from the surrounding vasculature to promote growth [143]. Increased blood supply from such feeding vessels alongside tumour growth would be expected to gradually increase tumour susceptibility to systemic variations. Additionally, the magnitude of $+\Delta R_2^*$ responses to 100% O_2 decreased with the study days. In this regard, and as previously mentioned in section 2.2, the relationship between R_2^* variation and tumour pO_2 change was found not to be reproducible, and so a direct comparison between tumours requires caution [109], which represents a limitation of the current study. Nevertheless, this observation suggests tumour growth promoted gradually weaker steal effects, possibly through decreased vasoconstriction, although the reasons behind this effect merit further investigation.

Between tumour types, SW1222 tumours showed higher prevalence of $-\Delta R_2^*$ response to carbogen at days 4 and 8. This effect was also anticipated due to the previously known vascular differences between SW1222 and LS174T tumours [117-120] which were confirmed in the histological analysis performed here. SW1222 tumours have higher vascular density and are better perfused, which leads to higher functional fractions. Under a carbogen challenge, SW1222 tumours could potentially respond better to radiation therapy, due to larger oxygenated tumour volume, as well as to systemically applied therapies (e.g. chemotherapy), due to better delivery, relative to LS174T tumours, although therapy response also depends on the sensitivity of the targeted cell line.

Relative to the response type, $-\Delta R_2^*$ responses were significantly more prevalent than $+\Delta R_2^*$ responses to carbogen (days 4, 6 and 8) and 100% O_2 (day 8) breathing in SW1222 tumours. This result suggests the majority of perfused vessels are experiencing increased oxygenation, being therefore functional. Negative ΔR_2^* responses were also stronger (higher magnitude) than positive ΔR_2^* responses to carbogen (day 8) in SW1222 tumours, which, although not quantitatively related to tumour pO_2, is further informative about the state of functional vasculature in these tumours.

The lack of any longitudinal effects or response type differences in LS174T tumours is probably the result of the relatively low vascular density and poor perfusion alongside large hypoxic areas in these tumours [112]. Such microenvironmental characteristics potentially impair the effect of the hyperoxic gas challenges, rendering it too small to be reliably detected.

The observations from the longitudinal vasoactive hyperoxia gas challenges indicate that the size/stage of the tumour development influences its vascular response, so one must take that into account when performing studies of this nature.

On a technical note, it is worth to acknowledge that some R_2^* values in the time series of some voxels are possible to have been influenced by poor goodness of fit, arising mostly from the lower signal intensity at later echo times against the background noise and consequent greater measurement uncertainty. However, the majority of such inaccuracies are expected to have been filtered out by applying the MAP thresholding, in resting state maps, or the family-wise clustered SPM thresholding, in gas challenge maps.

4.4.3. Tumour response to hypercapnia

The longitudinal hypercapnia challenge (air + 5% CO_2) aimed to infer the evolution of tumour vessel maturation by assessing the strength and prevalence of signal intensity increase responses ($+\Delta SI$). Differences between response type ($+\Delta SI$ vs. $-\Delta SI$) were additionally studied to assess the maturation state of the perfused vasculature. Differences in mature vasculature between tumour types were also investigated.

Longitudinal effects were not observed in SW1222 or LS174T tumours, suggesting no tumour growth-associated evolution of the mature vasculature. This result indicates the 100% O_2-induced decrease in $+\Delta R_2^*$ magnitude (discussed in section 4.4.2.) was probably not due to a decrease in vascular maturation.

Between tumour types, $+\Delta SI$ responses were significantly more prevalent in SW1222 tumours at day 4. This result could indicate the vasculature of SW1222 tumours was more mature than in LS174T tumours. However, the histological analysis of the percentage of mature vessels revealed similar values between tumour types. Consequently, this predominance of $+\Delta SI$ response in SW1222 tumours is probably due to their higher vascular density and perfusion.

The percentage of $+\Delta SI$ responses was higher than their negative counterpart in SW1222 tumours at day 4, which suggests most perfused vessels are mature in his tumour type. LS174T tumours did not discriminate between response types, and so the percentage of mature perfused vessels is possibly similar to the percentage of immature perfused vessels.

4.4.4. Spontaneous fluctuations *versus* gas challenge responsiveness

The possibility that the amplitudes of R_2^* spontaneous fluctuations and gas challenge-responsive areas (hyperoxia and hypercapnia) were well correlated was not generally confirmed. Suggestive correlations only occurred in a few occasions at days 0 and 2, and even these were not especially strong.

It must be true that spontaneous fluctuations, as well as gas challenge responses, can only occur in perfused blood vessels. Related to this is the good spatial agreement between the histological perfusion marker Hoechst 33342 and R_2^* SD high amplitude variations. So why were the amplitudes of spontaneous fluctuations and gas challenge

responses not strongly correlated? First of all, the relationship between the amplitudes of both measurements is not necessarily the same as the relationship between their spatial distributions. Additionally, while a tumour region is fluctuating at a given moment, it might not be at a future time point [34]. This behaviour can cause an apparent reduction in the fluctuating amplitude, whereas the vasculature might still be well perfused and strongly responsive to the gas challenge. The opposite may also happen, where a high spontaneous R_2^* amplitude variation occurred in a region weakly responsive to the gas challenge, due to a decrease in perfusion at the time of the gas challenge. Another potential confounder is the fact that well-perfused and highly oxic tumour areas would not show a significant R_2^* change because haemoglobin is already largely saturated [49]. This could have occurred, particularly in SW1222 tumours, further impairing the correlations between resting state and hyperoxia amplitudes. Finally, a degree of uncertainty might still be present in each of the R_2^* estimates, which can manifest as additional scatter in the voxel-wise correlation plots and reduce the correlation coefficient.

In the hypercapnia challenge, one must additionally take into account the fact that around 50% of the vasculature was immature. This means perfused vessels can be either mature or immature, further diminishing the likelihood of a strong correlation.

4.4.5. Influence of blood pH on R_2^* measurements

Spontaneous fluctuations in tumour and muscle tissues were probably not influenced by the pH of blood, given that no deviations from the reference range were observed at 60 minutes post-anaesthesia induction.

During the gas challenge experiment, pH oscillations under and above the resting state pH were observed. Carbogen breathing caused a pH decrease due to increased carbon dioxide in the blood. This effect triggered a compensatory acid-base homeostasis mechanism, in which the concentration of metabolic HCO_3^- ($[HCO_3^-]$) alkalotic ion also increased.

Upon changing to the second air breathing phase, CO_2 tension in the blood decreased to its initial value. However, a further increase in $[HCO_3^-]$ was observed, causing the highest registered pH. It should be mentioned this effect was observed in one animal and, given the impossibility to repeat the experiment (due to faulty equipment and lack

of assistant personnel), it is unclear whether this is a reproducible phenomenon. Nevertheless, observation of R_2^* time courses revealed similar R_2^* values between baseline and upon the second air breathing phase, suggesting either the Bohr effect did not significantly affect R_2^* estimates or the blood alkalosis at the second air breathing phase is uncommon.

The 100% oxygen breathing phase caused a [HCO_3^-] decrease due to the continued absence of perturbations to the CO_2 tension. This caused pH values to return closer to the resting state pH. Finally, hypercapnia caused the lowest pH due to the combined effect of increased CO_2 and low concentration of HCO_3^-.

Variations in pH between carbogen and air breathing were previously reported [108], and were suggested to be a possible confounder to R_2^* response, although its effect is unclear [144]. In this study, if the Bohr effect had had an influence on the hyperoxia response, carbogen breathing would have been expected to show weaker responses and/or lower percentage responsiveness relative to 100% O_2 breathing. It is not obvious that such difference occurred in either tumour type, although carbogen and 100% O_2 responses were not statistically compared. Still, this observation is further suggestive of the minimal influence of the Bohr effect on the tumour response. Perhaps the fact that carbogen improves blood flow, in addition to oxygenation, in functional and mature blood vessels, counteracted the pH effect [135].

4.5. Conclusions

This study demonstrated the feasibility of using gradient-echo MR sequences to estimate the occurrence of spontaneous fluctuations in blood oxygenation in colorectal carcinomas. In particular, it showed that the percentage of the tumour experiencing spontaneous fluctuations is independent of the tumour size, and that the amplitude of such fluctuations may be influenced by the tumour stage, depending on the tumour type. The frequencies of oscillatory behaviour were additionally found to be influenced by the stage of tumour development.

Vasoactive challenges revealed that the percentage of the tumour responsive to carbogen breathing increases with the tumour growth, which suggests systemic influences in tumours become increasingly more important. However, this occurs only

if the tumour is well perfused. Consequently, the better perfused tumours also have higher response prevalence.

Comparison of magnitude variations between gas challenge responses and spontaneous fluctuations did not reveal strong correlations, indicating one cannot use vasoactive protocols to infer about the amplitudes of fluctuation. However, a good spatial agreement was found between high amplitude fluctuations and histological markers of viable tissue and vascular perfusion, confirming spontaneous fluctuations occur preferentially in perfused areas.

Breathing of gas mixtures of high oxygen and/or carbon dioxide concentration was shown to affect systemic blood oxygen saturation and systemic blood pH. Still, the pH effect probably had minimal repercussions in the studied tumours given that both the prevalence and response amplitude were similar between different breathing gases. Conversely, continuous air breathing showed no pH drifts from the reference range, and so the occurrence of tumour spontaneous fluctuations was probably not influenced in this way.

5. Influence of systemic variations on cycling hypoxia patterns in tumours

The experimental results shown in Chapter 4, together with earlier studies (described in section 2.2.1), support of the use of gradient-echo MRI to study several aspects of blood oxygen fluctuations in tumours. However, the influence of systemic variations in cycling hypoxia patterns in tumours has not yet been directly investigated. This chapter addresses this issue by comparing spontaneous R_2^* fluctuations in tumours with systemic measurements of blood oxygen saturation, in which two different approaches were considered. Part of the work comprised in this chapter was used to write a paper entitled 'Decomposition of spontaneous fluctuations in tumour oxygenation using BOLD MRI and independent component analysis', which was accepted for publication in the British Journal of Cancer [145].

5.1. Introduction

The initial approach to the above-described problem consisted of a correlation assessment between tumour R_2^* dynamics and systemic pulse oximetry recordings. This method allows the mapping of the tumour regions mostly influenced by systemic blood oxygen variations, thereby enabling fluctuations caused specifically by tumour pathophysiology to be identified.

Although useful for a fast initial assessment, this initial "direct correlation" approach requires a given tumour imaging voxel to be fluctuating either due to systemic or tumour-specific influences, when it is likely that most oscillating voxels display a combination of both processes. To overcome this limitation, a novel methodological approach based on independent component analysis (ICA) was developed. ICA is a computational blind source separation technique that has been used in BOLD studies of the brain, which allows a signal to be decomposed into its constituent components [146-148]. In the brain, ICA has been applied to identify spatially coherent fluctuations in blood oxygenation that are associated with regions that are functionally connected. By analogy, ICA is here proposed as a method to identify regional connectivity within tumours, albeit reflecting different biological mechanisms to those in brain, alongside the ability to study such signals in isolation. Each isolated tumour signal can thus be

compared with pulse oximetry to discriminate between systemically-driven and tumour-specific R_2^* fluctuations and account for both effects in the same imaging voxel.

Therefore, this study aimed to investigate whether tumour spontaneous fluctuations included contributions from systemic variations in blood oxygenation in SW1222 and LS174T tumours, alongside tumour-specific sources. To this end, direct correlation and ICA decomposition approaches were applied.

The hypotheses for this study were:

- Tumour cycling hypoxia events are the result of a combination of systemic and tumour-specific effects;

- The estimates of the ICA approach better reflect the relative influence of systemic and tumour-specific sources of fluctuation.

In addition, this study aims to assess whether the separation of the R_2^* patterns based on their source of fluctuation allows relationships with tumour pathophysiology to be uncovered.

5.2. Materials and methods

5.2.1. Animal models and imaging protocol

SW1222 (n = 5) or LS174T (n = 5) tumour xenografts were grown as previously described. Each tumour was scanned at rest at two weeks after inoculation, following the procedure described in section 3.3. Tumour volumes ranged from 135 mm^3 to 670 mm^3. The cohort of tumours used in this study is the same as the one used in Chapter 4 to assess histological distributions, although this chapter describes distinct post-processing strategies from those previously implemented.

5.2.2. *In vivo* pulse oximetry

Concurrently with the MRI acquisition, pulse oximetry recordings were obtained with a sensor clamped to the thigh of the animal (MouseOx, Starr Life Sciences Corp., USA), which allowed the direct measurement of systemic arterial oxyhaemoglobin

saturation – O_2sat. Systemic and tumour vasculature were modelled as shown in figure 5.1, wherein the tumour is influenced by both systemic and local changes in oxygenation.

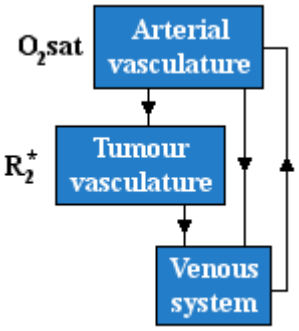

Figure 5.1 – Schematic diagram of the systemic influence on the tumour oxygenation.

5.2.3. Tumour MRI data analysis and relationship with systemic blood oxygenation

Tumour maps of resting state R_2^* estimates were calculated as described in section 3.4. Specific post-processing methods for each adopted approach (direct correlation or ICA) are described next.

5.2.3.1. Direct correlation approach

As with the analysis described in Chapter 4, only tumour imaging voxels exhibiting amplitude R_2^* oscillations above the uncertainty associated with background noise were considered for analysis. Pearson's correlation between each voxel's R_2^* time course and the systemic O_2sat trace was then performed. If the correlation was significant ($P < 0.01$), the corresponding R_2^* oscillatory behaviour was considered to be mostly due to systemic blood oxygen variations, and was represented in a voxel-wise matrix – $R_{2\,sys}^*$. Conversely, poorer correlations ($P > 0.01$) were ascribed to local, tumour-specific, events, where R_2^* time courses were represented in a separate matrix – $R_{2\,ts}^*$. A summary of the data acquisition and post-processing is shown in figure 5.2A. Measurements of systemic arterial blood pressure were equally taken, concomitantly with O_2sat and MRI,

although issues with probe malfunction meant not enough numbers were obtained to perform a reliable statistical analysis, and so these measurements were not included in this thesis.

The percentage of oscillating voxels and their mean R_2^* standard deviation (SD) were computed separately for systemic and tumour-specific oscillations. Wilcoxon matched-pairs tests were used to compare between systemic and tumour-specific distributions within the same tumour line. Mann-Whitney *U*-tests were used to assess differences between tumour types.

5.2.3.2. Model for MRI data decomposition – ICA approach

A timeline of the data acquisition and post-processing procedures for the ICA approach is shown in figure 5.2B. Tumour R_2^* time courses were first processed using principal component analysis (PCA), a computational technique that allows the extraction of the highest variance components in the data, and which is usually applied to highly dimensional datasets. In PCA, the variance in the data is associated to eigenvectors in a decreasing rank-order fashion, so that the first eigenvector has the largest variance, the second eigenvector has the second largest variance, and so on [149]. This ordered process results in the last eigenvectors having very little variance, being thus ascribed to background noise [149]. Dimensionality reduction of the R_2^* data was then performed. This was achieved by selecting all the eigenvectors up to the 'shoulder' of the PCA decomposition curve (see Fig. 5.2C) as well as the eigenvectors after that point which were associated with a time course exhibiting a dominant frequency peak. At this intermediate stage, power spectra were observed using the Fast Fourier Transform (FFT) method, instead of the Lomb method, due to its substantially faster computational time and because the main concern was to observe whether any frequency peaks were present, regardless of how accurate these were being represented. On average, 89 out of 944 eigenvectors per dataset were chosen ($n = 10$). This pre-processing procedure was performed for two reasons: (i) it allowed the subsequent ICA decomposition of the data to be simplified, because the great majority of the variance is concentrated on a reduced number of eigenvectors, meaning all the data can be explained in fewer components, and (ii) by doing so, some of the background noise is expected to be filtered out, which also facilitates the ICA decomposition [149].

Spatial ICA was then applied to this dimensionally reduced data (FastICA v2.5 [150]), allowing the linear superposition of signals that compose the R_2^* dynamics to be separated into independent processes (or components). Each independent component has a (previously unknown) unique time course and an associated spatial map. Each component map quantifies how much each voxel's R_2^* behaviour is explained by the corresponding component time course. Due to their independence from one another, each independent component can be studied individually. The decomposition process was modelled as:

$$X = MS \quad , \qquad \text{Eq. 5.1}$$

where X is the voxel-wise matrix of R_2^* time courses, which was transformed into a 2D matrix (*time points* × *number of voxels*); M is the "mixing" matrix (*time points* × *number of components*), which contains each (data-driven) component time course in a separate column, and has a corresponding spatial representation in the rows of matrix S (*number of components* × *number of voxels*) [148].

Separation between systemic and tumour-specific influences on tumour R_2^* fluctuations was undertaken by correlating each independent component time course with the systemic O_2sat time course (Pearson's linear correlation). A significant correlation ($P < 0.01$) suggested that the current independent component represented systemic blood oxygenation dynamics. Conversely, if the correlation was less significant ($P > 0.01$), the time course of the independent component, its FFT power spectrum and its spatial map were studied in order to assess if it was a component modelling tumour-specific dynamics. Two selection criteria were adopted: (i) if the frequency spectrum presented a peak at a defined frequency, this was enough evidence of cycling behaviour, or (ii) if the independent component spatial maps, which were normalised and thresholded by z-value ($|\text{z-score}| \geq 2.2$) [148], presented clustering regions (minimum of 5 voxels), this meant that those regions shared a degree of similarity in their R_2^* dynamics. To improve the robustness of the second selection criteria, only the components that exhibited spatial clustering regions associated with non noise-like (distinctive) temporal features were selected, in order to prevent noisy independent components from being considered (see Fig. 5.2D). When observed, regional clustering was often present across several imaging slices, as demonstrated by the 3D representation in figure 5.2D, suggesting temporally coherent R_2^* patterns over a

tumour volume. Any remaining components (i.e., ones with poor correlation and that did not exhibit a frequency peak or spatial clustering effects), were considered to be modelling any background noise not previously filtered by PCA and were not considered for further analysis.

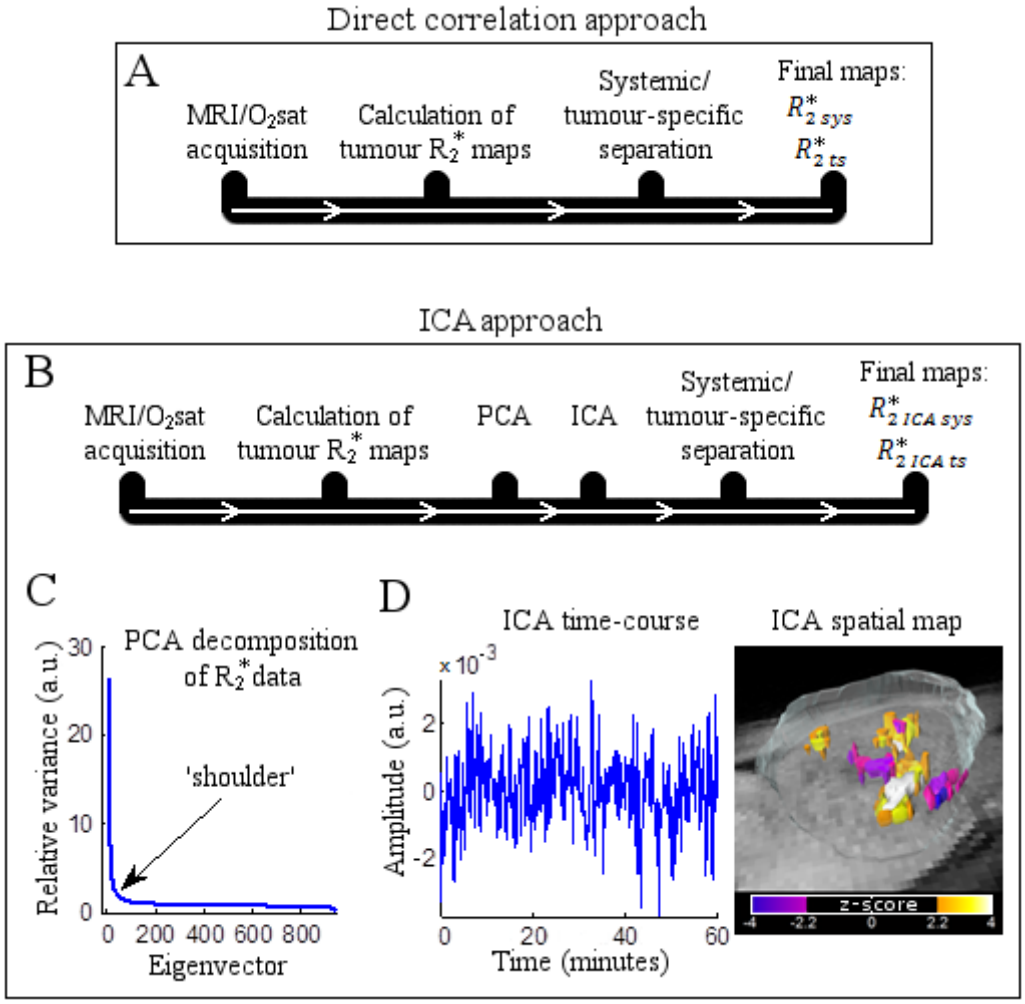

Figure 5.2 – Data acquisition and post-processing for the direct correlation approach and the ICA approach. A, B: Timeline of data acquisition and post-processing methods for each approach. **C:** PCA decomposition curve showing the relative variance associated to each eigenvector. Eigenvectors to the left of the 'shoulder' of the curve have high variance. **D:** Time course and 3D spatial map of one independent component in an example SW1222 tumour. Adapted from [145].

The next step consisted of combining the component time courses matrix with the component spatial maps matrix to recover the R_2^* data, although now separated into systemic and tumour-specific influences, in a process which is the reverse of the ICA decomposition:

$$R_{2\,ICA\,sys}^{*} = M_{sys}S_{sys}$$

Eq. 5.2

$$R_{2\,ICA\,ts}^{*} = M_{ts}S_{ts} \quad ,$$

where $R_{2\,ICA\,sys}^{*}$ and $R_{2\,ICA\,ts}^{*}$ are the voxel-wise matrices of systemic and tumour-specific R_2^* time courses, respectively.

Lastly, to threshold $R_{2\,ICA\,sys}^{*}$, a final correlation between the systemic O_2sat and the time courses of individual voxels of $R_{2\,ICA\,sys}^{*}$ was computed (Pearson's linear correlation). Only the most significant correlations ($P < 0.01$) were selected to represent systemically oscillating tumour regions. A similar procedure was employed to detect the most tumour-specific fluctuating areas, where only non-significant correlations ($P > 0.05$) between the systemic O_2sat and the dynamics of $R_{2\,ICA\,ts}^{*}$ were considered. As in the direct correlation approach, Wilcoxon matched-pairs tests were used to compare between systemic and tumour-specific distributions within the same tumour line. Mann-Whitney *U*-tests were used to assess differences between tumour types.

5.2.4. Frequency analysis of thresholded R_2^* maps and O_2sat curves

Time courses of thresholded systemic or tumour-specific R_2^* maps, following the direct correlation or the ICA approach, were analysed in the frequency domain, for both tumour lines. Similarly to Chapter 4, the Lomb method was applied to individual R_2^* time courses and subsequently combined into a single averaged spectrum. The spectral mean and standard deviation of the tumour cohort was then computed. The Lomb method was equally applied to O_2sat curves, where the mean and standard deviation of the cohort of mice bearing SW1222 or LS174T tumours was computed. Dominant frequencies of R_2^* or O_2sat oscillation were assessed based on spectral power (peak height).

5.2.5. Histological assessment and whole-tumour statistical relationships

Histology was performed following MRI imaging as described in section 3.5. Fast spin-echo anatomical images were used to measure tumour volumes. Statistical

correlations between distributions of histological, R_2^* or tumour volume measurements required the use of non-parametric Spearman's rho test due to small sample numbers. $P < 0.05$ was considered to be significant.

5.3. Results

5.3.1. Relationships between sources of R_2^* oscillation and between tumour lines

Figure 5.3 shows an example SW1222 tumour, in which R_2^* time courses were found to be significantly correlated with systemic blood oxygenation variations ($P < 0.01$, Pearson's correlation) using either the direct correlation approach ($R_{2\,sys}^*$) or the ICA approach ($R_{2\,ICA\,sys}^*$). Additionally, both approaches revealed R_2^* temporal patterns that were not correlated with systemic blood oxygen variations ($P > 0.05$, Pearson's correlation), which were considered to be specific to the tumour microenvironment ($R_{2\,ts}^*$ or $R_{2\,ICA\,ts}^*$). Using the direct correlation approach, these two sources of oscillation were identified in separate tumour regions. However, the ICA approach demonstrated the ability to identify systemic and tumour-specific R_2^* oscillations in the same voxel, not being necessarily from discrete regions in the tumour. Both oscillatory sources were observed in all SW1222 ($n = 5$) and LS174T ($n = 5$) tumours using either approach.

The percentage of voxels exhibiting systemic or tumour-specific fluctuations in each tumour line is represented in figure 5.4A (direct correlation approach) and figure 5.4C (ICA approach). The majority (or all – Fig. 5.4A, SW1222) of SW1222 and LS174T tumours showed a greater occurrence of tumour-specific fluctuations than systemic fluctuations, although the difference was not statistically significant ($P > 0.05$, Wilcoxon matched-pairs test).

The mean standard deviation of R_2^* fluctuations is plotted in figure 5.4B (direct correlation approach) and 5.4D (ICA approach). No significant differences were observed between systemic and tumour-specific fluctuations or between tumour lines.

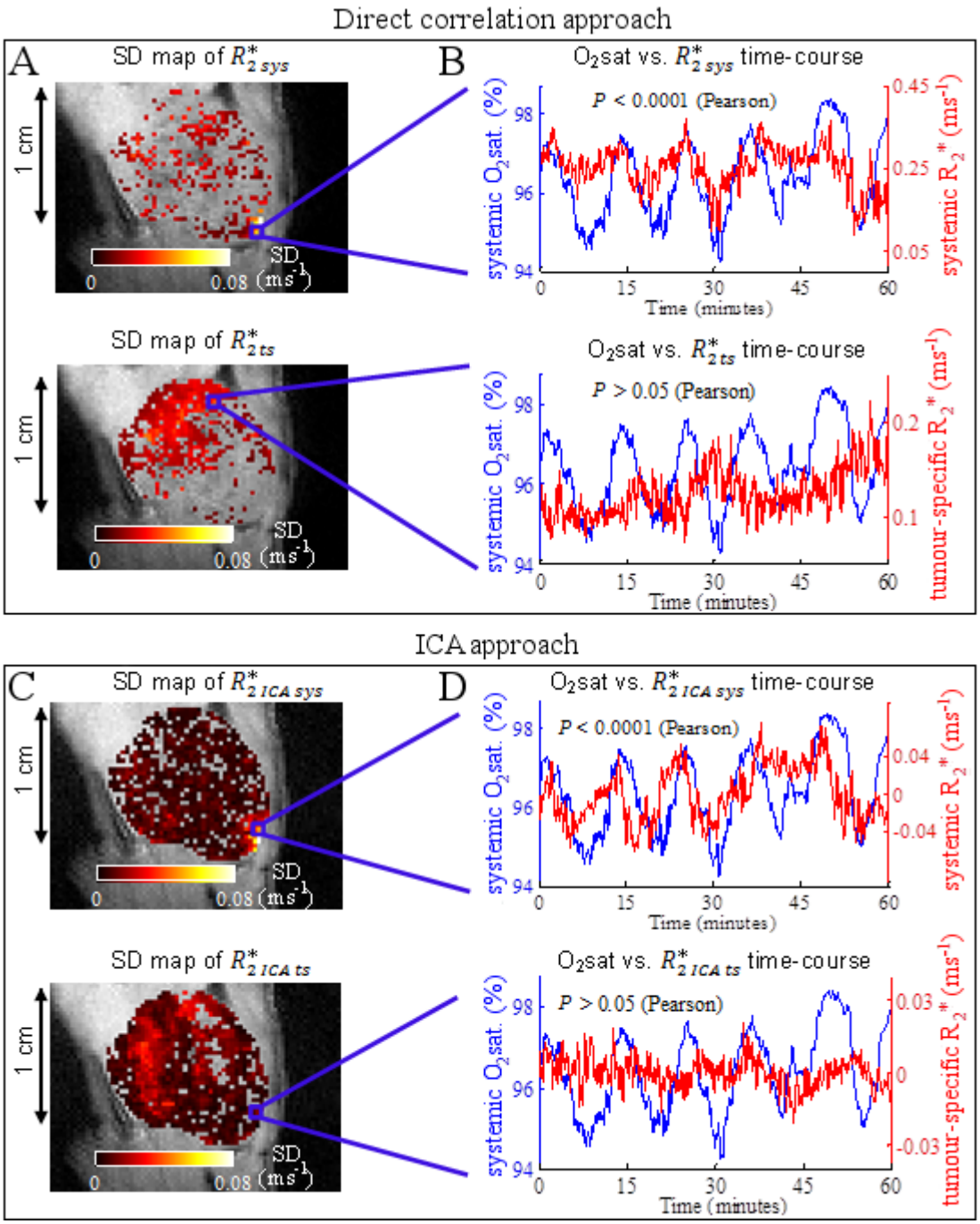

Figure 5.3 - Systemic and tumour-specific influences on tumour R_2^* spontaneous fluctuations in an example SW1222 tumour, following the direct correlation or the ICA approach. A, C: Voxel-wise standard deviation (SD) maps of the R_2^* fluctuations due to systemic (direct correlation: $R^*_{2\,sys}$; ICA: $R^*_{2\,ICA\,sys}$) or tumour-specific (direct correlation: $R^*_{2\,ts}$; ICA: $R^*_{2\,ICA\,ts}$) influences. High SD in different regions between maps distinguishes the tumour areas most affected by either source. With ICA decomposition, colocalised voxels between both maps reflect the simultaneous influence of systemic and tumour-specific events in those tumour regions. **B:** Correspondence between the R_2^* time course from a single voxel (red), oscillating above noise uncertainty, and the O_2sat curve (blue). **D:** Correspondence between the R_2^* time course from a single voxel (red), after ICA separation, and the O_2sat curve (blue). R_2^* and O_2sat were measured simultaneously. Adapted from [145].

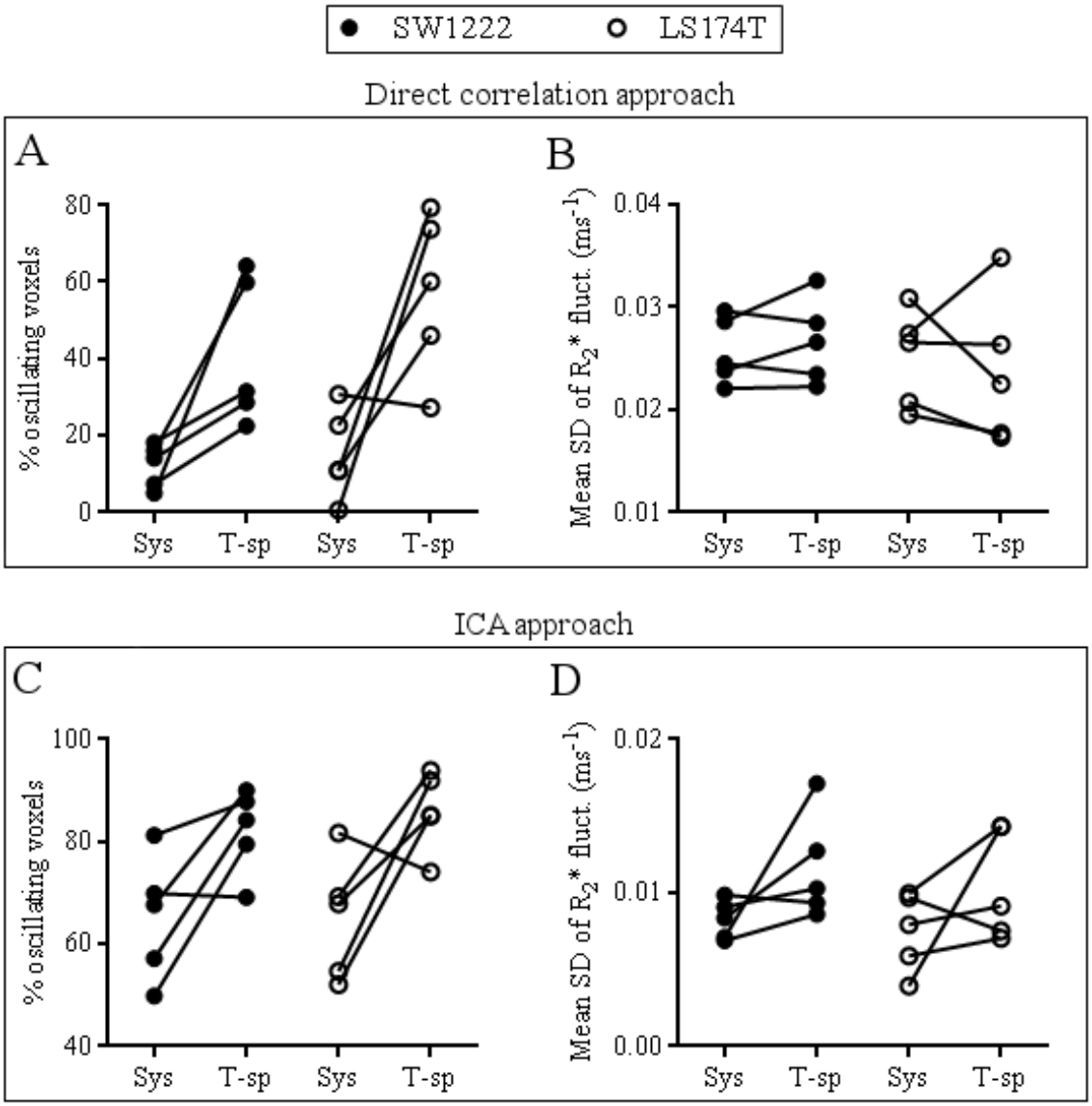

Figure 5.4 – Relative influence of systemic (Sys) and tumour-specific (T-sp) fluctuations in SW1222 and LS174T tumours, following the direct correlation or the ICA approach. A, C: Percentage of systemic and tumour-specific oscillating voxels. **B, D:** Mean standard deviation (SD) of R_2^* fluctuations. In both tumour lines, fluctuations due to tumour-specific influence showed higher prevalence in the majority of tumours, relative to systemic fluctuations (panels A and C), although these differences were not statistically significant (Wilcoxon matched-pairs test). No significant differences were found in the SD of R_2^* fluctuations (panels B and D). Adapted from [145].

All LS174T tumours exhibited large systemic fluctuations in the tumour periphery (Fig. 5.5), which can more easily be appreciated in the R_2^* SD maps of the ICA approach, whereas tumour-specific fluctuations were observed in both the centre and the periphery. Conversely, systemic and tumour-specific fluctuations were distributed throughout SW1222 tumours.

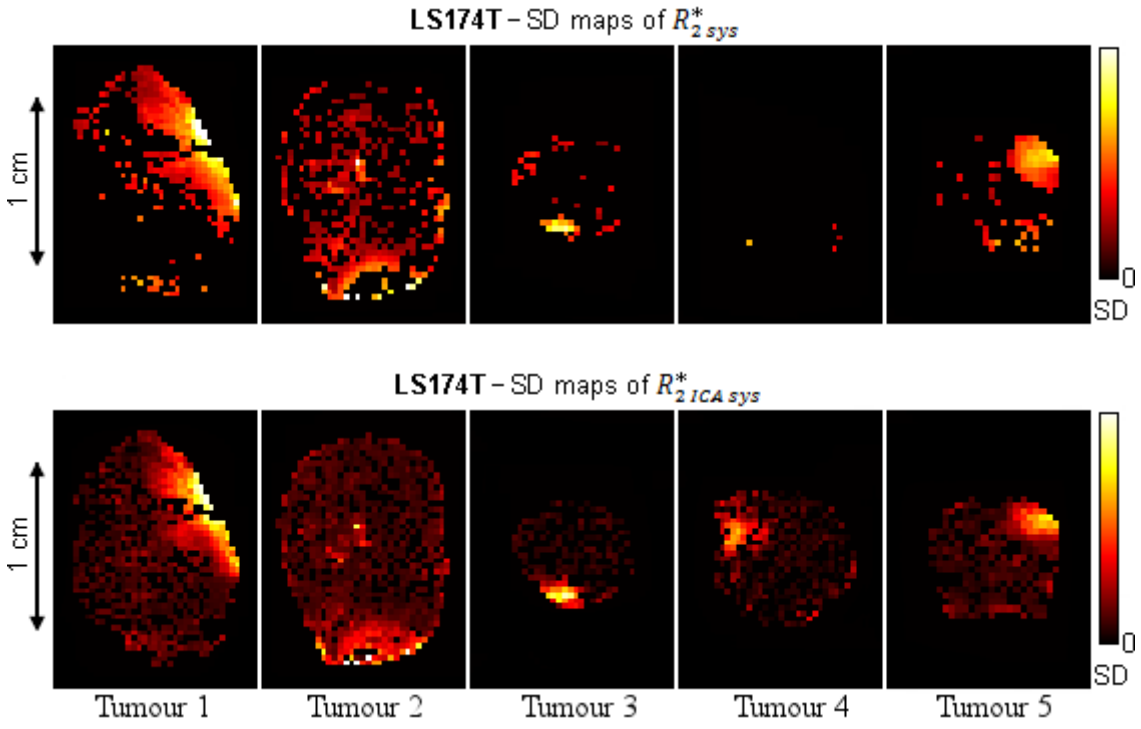

Figure 5.5 – Spatial distribution of high amplitude systemic R_2^* fluctuations, following the direct correlation ($R^*_{2\,sys}$) or the ICA approach ($R^*_{2\,ICA\,sys}$). High amplitude systemic fluctuations are located in the tumour periphery, which is more apparent in the ICA approach maps. Conversely, SW1222 fluctuations (systemic and tumour-specific), and LS174T tumour-specific fluctuations, displayed no obvious spatial patterning. Adapted from [145].

Figure 5.6 shows the frequencies of R_2^* fluctuations, organised by tumour line and fluctuating source, for both approaches[3]. Dominant frequencies were assessed from the peak height of frequency spectra. The range of dominant frequencies (in cycles/hour) in each plot is shown in bold. The lowest frequency peaks, observed at 0.75 cycles/hour or 1.00 cycle/hour, are at similar frequencies to those observed in Chapter 4 for a 60 minute-long acquisition. Conversely, highest frequencies of oscillation are commonly different to those previously detected, especially for the ICA approach, where these are either above (systemic: SW1222) or below (systemic: LS174T and tumour-specific: both tumour lines).

Between direct correlation and ICA approaches, the range of dominant frequencies in LS174T tumours is comparable. In SW1222 tumours, however, some differences were

[3] The results of the frequency analysis here presented (using the Lomb method) differ from those published in the British Journal of Cancer paper (where FFT was employed) [145]. Here, the Lomb method revealed an advantage relative to FFT due to the oversampling capacity, which allowed a better differentiation between frequency peaks.

observed. Specifically, a broad peak at 7.75-8.00 cycles/hour was detected in tumour-specific oscillations when using the direct correlation approach (see green arrow), but not when ICA decomposition was employed. Upon analysis of the spectra of SW1222 systemic oscillations, peaks at similar frequencies to the one mentioned above were observed in both the direct correlation (peak at 7.5 cycles/hour) and ICA (broad peak at 7.5-7.75 cycles/hour) approaches (see red arrows). This observation suggests the R_2^* fluctuations identified as tumour-specific in the direct correlation approach are additionally being partially influenced by systemic influences, which provides further evidence of the simultaneous influence of systemic and local fluctuating mechanisms in a given tumour region. The ICA decomposition additionally revealed the ability to detect complex fluctuating modes, where 6 distinct peaks were observed in the spectrum of SW1222 systemic oscillations against the 5 peaks in the equivalent spectrum of the direct correlation approach.

Within the spectra of the ICA approach, systemic influences revealed differences in the range of oscillatory frequencies between both tumour lines, with SW1222 tumours presenting peaks at higher frequencies. The same was not observed in tumour-specific influences, where the dominant frequency range was comparable between SW1222 and LS174T tumour types. Between sources of fluctuation, systemic influences showed broader dominant frequency ranges, with peaks at higher frequencies, in both tumour lines, which is in agreement with the fact that systemic O_2sat curves exhibit a relatively broad range of frequencies in both SW1222 and LS174T tumour-bearing mice (see Fig. 5.7).

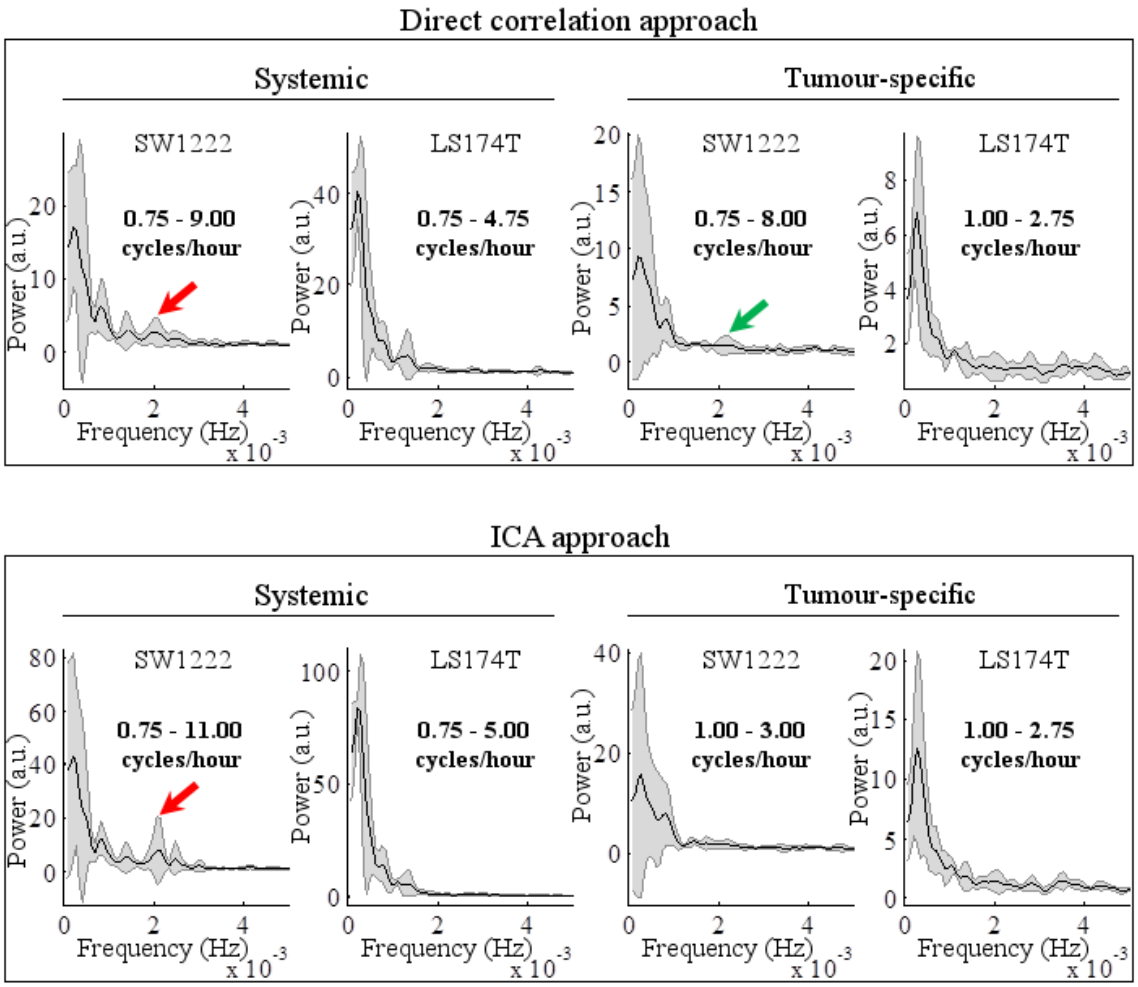

Figure 5.6 – Frequency analysis of tumour R_2^* oscillations, for the direct correlation or the ICA approach, organised by tumour line and systemic or tumour-specific influence. Mean (black line) and standard deviation (shaded area) of power spectra are shown. The range of dominant frequency peaks is shown in bold. Green and red arrows show frequency peaks at similar frequencies between plots, suggesting systemic influences are present in tumour-specific oscillations in the direct correlation approach only. Different tumour types were observed to exhibit dominant oscillatory frequencies across different ranges. Systemic and tumour-specific sources also revealed different ranges of oscillatory frequency.

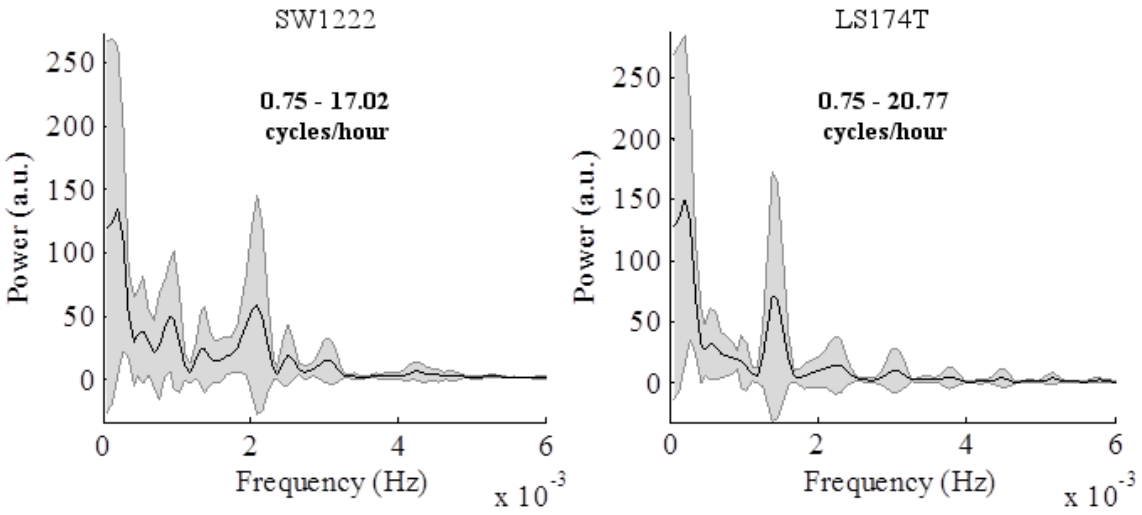

Figure 5.7 – Frequency analysis of the O_2sat curves in SW1222 or LS174T tumour-bearing mice. Mean (black line) and standard deviation (shaded area) of power spectra are shown. The range of dominant frequency peaks is shown in bold.

5.3.2. Physiological basis of tumour fluctuations

The percentage of each tumour that exhibited R_2^* fluctuations due to systemic influences was significantly correlated with the tumour volume when using the ICA approach (Fig. 5.8C, systemic) but not with the direct correlation approach (Fig. 5.8A, systemic). There was no significant correlation between tumour volume and the percentage of each tumour exhibiting tumour-specific fluctuations in either approach (Fig. 5.8A, C, tumour-specific).

Comparison of histological measures with MRI data revealed a significant inverse correlation between the percentage of mature vessels (assessed by co-localisation of α-SMA and CD31 immunostaining) and the magnitude of tumour-specific, but not systemic, fluctuations when using either approach (Fig. 5.8 B, D). No correlation was found between the percentage of mature vessels in each tumour and the size of the tumour.

Focusing on the results from the ICA approach, qualitative observations revealed that, in tumour sub-regions with high systemic or tumour-specific R_2^* variation, tissues were well perfused and viable (non-necrotic) in 4 SW1222 (n = 5) and 3 LS174T (n = 4) tumours. This result is slightly different from that observed in Chapter 4 in the same tumour cohort, where all tumours presented high R_2^* SD associated with well perfused and viable tissue.

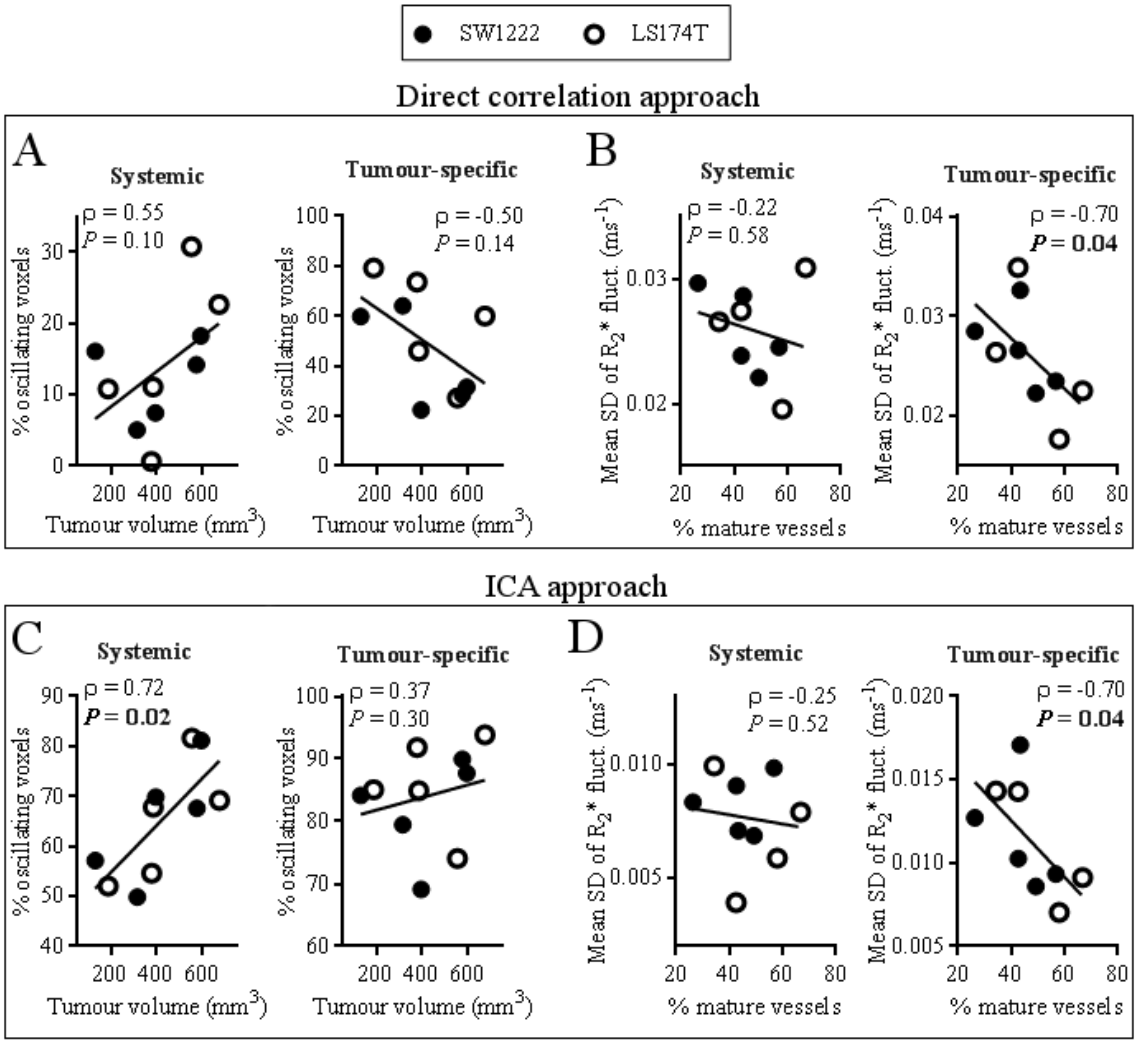

Figure 5.8 – Relationship between tumour size, R_2^* fluctuations and mature vasculature, for the direct correlation or the ICA approach. Significance was tested with Spearman's rho correlation test. **A, C:** Influence of tumour size on the occurrence of systemic or tumour-specific R_2^* fluctuations. Direct correlation did not reveal any significant relationships (P > 0.05). Conversely, ICA decomposition showed the percentage of systemically oscillating voxels is directly related to the size of SW1222 and LS174T tumours (P = 0.02), but no relationship was found with tumour-specific oscillations (P = 0.30). **B, D:** Both approaches revealed the percentage of mature vessels is inversely related to the mean standard deviation (SD) of tumour-specific, but not systemic, R_2^* fluctuations (P = 0.04 for both approaches). Adapted from [145].

5.4. Discussion

5.4.1. Discrimination between the sources of R_2^* fluctuation in tumours and between tumour types

In this study, two different approaches were employed for characterising individual contributions to cycling hypoxia in tumours. Specifically, each approach was designed to separate systemic from tumour-specific sources of R_2^* variation in individual tumours. The first – direct correlation approach – involved the correlation of tumour R_2^* time courses with systemic blood oxygen saturation (O_2sat) readings. The second – ICA approach – involved the decomposition of tumour R_2^* signals into its constituent components, using independent component analysis, and posterior separation into systemic or local influences based on the O_2sat curve, alongside noise filtration. Each approach allowed the identification of the areas mostly affected by either mechanism in individual tumours. Low-frequency fluctuations in oxygen tension and blood flow were previously observed in both tumour and muscle by Braun and collaborators [35], using recessed-tip oxygen microelectrodes and laser-Doppler flow probes. Despite having observed greater low-frequency activity and greater magnitude changes in tumours, this provided an early suggestion for systemic influences. Baudelet and colleagues [34] also reported a similar observation when comparing T_2^*-weighted gradient-echo fluctuations between tumour and contralateral muscle. They additionally looked at whether muscle and tumour time series were correlated, and concluded that systemic changes did not affect the tumour microenvironment because no significant results were obtained. Although the direct correlation approach presented here is conceptually similar to their study, the ICA approach is more refined, as it isolates high-variance data and separates the multitude of processes contributing to R_2^* fluctuations prior to any time series correlation. Moreover, ICA decomposition provides the unique advantage of being able to identify tumour regions that are simultaneously suffering from systemic and tumour-specific effects, which would be otherwise impossible. These features meant the results between both approaches differed in occasions, as observed in the previous section, with the measurements obtained with the ICA approach being generally considered more reliable. For this reason, interpretation of the results obtained will mainly focus on the ICA approach data.

Systemically-driven, high amplitude fluctuations were observed to be preferentially located in the tumour periphery in LS174T tumours, whereas in SW1222 tumours there

was no preferential location. This observation is potentially due to the less extensive vascular network evident in LS174T tumours, compared with SW1222 tumours. Fewer blood vessels can lead to impaired perfusion which, in combination with the higher microvascular density in the LS174T tumour periphery, potentially reduces the influence of systemic variations in the central area of the tumour. A similar observation was reported in an MRI study of A-07 melanoma xenografts, where blood flow fluctuations occurred preferentially in the tumour periphery, in which case the authors considered vasomotor activity in the supplying vasculature as a probable cause of fluctuations [88]. Conversely, SW1222 tumours have a vascular tree closer to that of normal tissues, leading to greater perfusion throughout the tumour (and less hypoxia), and potentially allowing the transmission of systemic variations from the tumour edge towards its core more effectively.

The range of dominant oscillatory frequencies of R_2^* estimates varied between tumour lines and between sources of fluctuation. Considering the systemic fluctuations, SW1222 tumours exhibited a wider range of frequencies relative to LS174T tumours. This result is unlikely to be due to differences in the O_2sat fluctuations between mice bearing one or the other tumour type because LS174T tumour-bearing mice actually presented a wider range of frequency peaks than SW1222 tumour-bearing mice. This result is again probably due to the significantly denser and better perfused vasculature of SW1222 tumours, which renders these tumours more susceptible to systemic influences relative to LS174T tumours, as was demonstrated in Chapter 4 with the systemically applied carbogen and hypercapnia challenges. Conversely, tumour-specific fluctuations of both tumour types have comparable frequencies of fluctuation. Between sources of fluctuation, broader ranges of frequency peaks were observed in systemic fluctuations in both tumour types. Considering that (i) O_2sat fluctuations experience a relatively broad range of frequencies and (ii) tumour-specific R_2^* fluctuations have a relatively narrow frequency span, then systemic R_2^* fluctuations would indeed be expected in a wider range relative to tumour-specific R_2^* fluctuations. Interestingly, the higher frequencies of O_2sat oscillations seem to have been attenuated in tumours. Tumour and normal vasculatures present marked structural and functional differences, and so it is conceivable that not all dynamic properties of systemic oxygenation will influence the tumour regions suffering from such effects.

5.4.2. Relationships between R_2^* fluctuations and pathophysiological measurements in tumours

Systemic and tumour-specific sources of R_2^* oscillations were further assessed by comparing the percentage of oscillating voxels with the tumour size. The occurrence of systemic, but not tumour-specific, R_2^* oscillations was found to be directly related to the size of tumours in both SW1222 and LS174T xenografts. Related to this, Chaplin *et al.* [37] had already reported a relationship between the occurrence of cycling hypoxia and the size of SCCVII tumours. In their study, they injected (i.v.) the fluorescent perfusion marker Hoechst 33342 twenty minutes before applying 10 Gy of radiation to tumours. Subsequently, a large differential survival between well perfused cells and poorly perfused cells was observed in small tumours ($\leq$ 200 mg). However, this differential decreased as the tumour size increased, which they inferred was due to a higher occurrence of cycling hypoxia in larger tumours, therefore acting as a protective mechanism against radiation. They suggested this relationship should depend on tumour type or site of implantation. Still, given the results presented here, one possible alternative is that, as tumours develop and acquire increased blood supply from the surrounding vasculature, the influence of systemic blood flow variations in the tumour becomes increasingly prevalent. Such effect can potentially occur by (i) an increase in the number of systemic feeding vessels accompanying tumour growth or (ii) an increase in the diameter of those vessels. In fact, results of Chapter 4 support this hypothesis, given that tumour growth favoured an increase in the percentage responsiveness to carbogen breathing. Nevertheless, the evolution of the tumour feeding vasculature does not seem to have yet been directly investigated and a study of this nature would provide valuable information about the systemic influences on tumour cycling hypoxia.

Oscillations in R_2^* estimates additionally revealed a link to tumour biology. The amplitude of tumour-specific fluctuations was found to be inversely correlated to the degree of vessel maturation in SW1222 and LS174T tumours, but no similar relationship was found with systemic fluctuations. This illustrates another key benefit of the methods developed in this study, in that isolation of tumour-specific fluctuations from those occurring due to systemic influence allows a clear insight into tumour pathophysiology. Interpretation of this finding relies on the role of mural cells in the structural support of blood vessels: mature vessels have increased integrity and stability [151], thus being less susceptible to mechanical stress-related microenvironmental factors responsible for cycling hypoxia, such as raised interstitial fluid pressure [31].

This interpretation is in agreement with a previous electron paramagnetic resonance imaging study of two carcinoma models, which suggested an inverse relationship between the maturity of the tumour microvascular network and the amplitude of tissue pO_2 fluctuations [86]. A similar conclusion was reported in a related study of melanoma and cervical carcinoma xenografts, where the presence of connective tissue embedding the tumour microvessels was associated with stabilisation of blood flow and tissue pO_2 fluctuations [152]. Moreover, T_2^*-weighted MRI estimates of pO_2 and blood flow in syngeneic fibrosarcoma-II tumours previously showed that signal fluctuations occur predominantly in regions of immature vasculature [41].

Moreover, no correlations were observed between the percentage of oscillating voxels (systemic or tumour-specific) and the percentage of mature vessels. This result is in agreement with the suggestion from Chapter 4 which stated that spontaneous fluctuations should occur regardless of the presence of muscle cell coverage, due to the homogeneous distribution of mature and immature blood vessels.

5.4.3. Limitations of the method

The approaches used in this study suffer from a number of limitations. In addition to the previously mentioned confounding effects associated to estimating blood oxygen variations with gradient-echo MRI [108], both approaches, as implemented here, did not consider any possible lag between the O_2sat variations and tumour R_2^* fluctuations. However, the circulation time in mice is of the order of the temporal resolution of the gradient-echo acquisition used in this study, so such effects can be assumed to be negligible. Additionally, systemic influences in the tumour microenvironment can come from different sources, such as pulsatile flow and blood pressure, in addition to blood oxygenation, which prevents the realisation of a ‘complete picture’ of the systemic physiological sources of the oscillations in the tumour. Still, this limitation can be overcome, at least partially, by simultaneous measurements of these systemic properties, concomitantly with MR imaging.

5.5. Conclusions

This study demonstrated a non-invasive and, particularly with the ICA approach, novel method to directly identify systemic influences on tumour cycling hypoxia patterns and separate these from tumour-specific effects. Due to its further refinement, the ICA approach is additionally considered a more accurate estimate of the relative influence of each source of R_2^* fluctuation in tumours, which is reflected in the results of this study.

This method has the potential to be easily translatable to the clinic, where tumour cycling hypoxia is still poorly characterised, with only a few published studies to date [83;94] (see Chapter 7 for an implementation of ICA in a clinical context). Although the systemic blood oxygenation might not suffer from such dramatic temporal variations in humans, the fact that other systemic effects are possibly influencing the tumour microenvironment is advantageous and can be incorporated in the method. If applied in the clinical setting, the ICA approach or its future versions would help predict the temporal and spatial delivery of systemically applied therapies, such as chemotherapy or radioimmunotherapy, in individual patients, and consequently help tailor a more effective delivery regime. Additionally, separating the sources of fluctuations occurring in tumours could potentially provide an insight into tumour pathophysiology in a clinical context, given the relationships found with vascular characteristics in this study.

6. Effect of imatinib therapy on R_2^* spontaneous fluctuations and gas challenge responsiveness in tumours

Chapters four and five were aimed to investigate the microenvironmental characteristics of tumour cycling hypoxia and its physiological basis. The current chapter builds on this knowledge to assess the effect of the agent imatinib mesylate, which has shown to have antiangiogenic properties, on tumour spontaneous R_2^* fluctuations and systemically applied vasoactive gas challenges. These measurements are complemented by a comprehensive range of histological markers.

6.1. Introduction

The antitumour therapy protocol employed in this study used imatinib mesylate (Novartis Pharma GmbH, Germany), a form of targeted therapy originally developed to treat chronic myeloid leukaemia [153], which was then applied to treat other tumour types such as gastrointestinal stromal tumours [154-156] or other forms of leukaemia, amongst others [157;158]. Imatinib mesylate is a tyrosine-kinase inhibitor of the receptor of platelet-derived growth factor (PDGF) [153;159;160]. PDGF is a protein that has an important role in the angiogenic process [161-164] and, accordingly, imatinib has previously been observed to reduce the microvascular density in clinical and pre-clinical tumours, including LS174T colorectal tumour xenografts [165-168]. Additionally, imatinib therapy was shown to decrease the intratumoral interstitial fluid pressure (IFP) in human xenograft models of lung (A549) and colorectal (LS174T) carcinoma [166;169]. Given these effects, imatinib therapy could potentially be promoting the normalisation of the vasculature in LS174T tumour models. The "vascular normalisation" hypothesis was popularised by Jain in 2001 [170], but was first proposed by Le Serve and Hellmann in 1972 [171]. It posits that antiangiogenic agents can prune some vessels whilst promoting an improvement of the integrity and function of the remaining vasculature towards a state more closely resembling normal vessels [170]. This effect was later supported in a number of studies using inhibitors of vascular endothelial growth factor (VEGF) or its receptor (VEGFR), where IFP reduction and improvements in perfusion, oxygenation and delivery of drugs or other molecules were observed [172-176]. Structural and functional vascular improvement is consequently associated with increased vascular coverage of perivascular cells

(comprised of pericytes and vascular smooth muscle cells) [174-177]; however, imatinib treatment has shown to reduce the pericyte coverage in different tumour models [178;179], given that PDGF also regulates the recruitment of such cells [180;181]. Still, this consequence is potentially tumour-type dependent, as no such effect was observed in a study with LS174T tumours [165].

Given the effects of imatinib therapy on LS174T tumours, a hypothesis of vascular normalisation can be formulated. The anticipated implications of a normalised vasculature are:

- To reduce the amplitude and prevalence of tumour R_2^* spontaneous fluctuations, which are characteristic of the highly permeable tumour vessels and elevated IFP microenvironment;
- To increase the responsiveness to gas challenges. Improvements in the tumour uptake of chemotherapeutic and radioimmunotherapeutic agents upon treatment with imatinib, including LS174T tumours, provide additional support for this hypothesis [165;168;169;182;183].

Further to these specific hypotheses, this study aims to investigate whether imatinib treatment caused an effect on tumour perfusion, hypoxia, vascular density or vascular maturation, as measured with histological markers.

6.2. Materials and methods

6.2.1. Animal models and *in vivo* MRI

Cells of the LS174T colorectal tumour line were cultured and injected as previously described (see section 3.2). After approximately 2 weeks of tumour growth, baseline MRI scans were performed (day 0). Three sets of data were acquired. The first acquisition was a 60-minute dynamic GEMS 'resting state' scan aimed at evaluating R_2^* spontaneous fluctuations at rest. The second acquisition was a 40-minute dynamic GEMS 'gas challenge' scan, during which different gas mixtures were administered in 10-minute intervals: air, carbogen, air, air + 5% CO_2 (hypercapnia). Changes in signal intensity (SI) and R_2^* relative to air-breathing phases were measured. GEMS sequence parameters were the same as described in section 3.3. The final acquisition was a Look-Locker segmented Inversion Recovery sequence, from which two $R_1(=1/T_1)$ maps

were calculated, one during air breathing and another during carbogen breathing. Look-Locker sequence parameters: *TR = 10 s, 50 TIs, TI spacing = 110 ms, TR_{RF} = 2.3 ms, TE = 1.18 ms, in-plane field of view 20×20 mm^2, matrix size 128×128, slice thickness 1.5 mm, 5 slices, flip angle = 8°*. This MRI protocol was repeated at days 3 and 5 of the study. R_1 data was obtained in collaboration with Rajiv Ramasawmy (UCL Centre for Advanced Biomedical Imaging).

6.2.2. Therapy protocol

Imatinib was administered by oral gavage (100 mg × kg^{-1} × day^{-1}, non-fractioned dose) immediately after the baseline scans and then each day for five consecutive days (n = 10). Animals in the control group were treated with saline (n = 9). Daily calliper measurements were taken to assess tumour growth rate. Tumour volume (V) was determined by the equation: $V = (\pi/6) \times longer\ diameter \times (shorter\ diameter)^2$ [169]. In the treated group, one tumour was not imaged, and was instead used for tumour growth assessment and histology. Another tumour in the treated group ulcerated at day 3 and this mouse had to be euthanised.

6.2.3. MRI data analysis

Four different spatial maps were calculated: **(i)** standard deviation maps of spontaneous R_2^* fluctuations (R_2^* SD maps); **(ii)** R_2^* maps of the difference between carbogen and air breathing (ΔR_2^*); **(iii)** R_1 maps of the difference between carbogen and air breathing (ΔR_1); **(iv)** signal intensity (SI) maps of the difference between hypercapnia and air breathing (ΔSI).

Maps of R_2^* SD were acquired in order to estimate the percentage of voxels fluctuating above the background noise uncertainty and their respective amplitude. To this end, the MAP algorithm was employed to threshold the maps. The example curves represented in figure 6.1A show, as would be expected, that original R_2^* time courses have a similar profile to PCA/ICA-filtered R_2^* time courses, although with higher variability. Nevertheless, relative differences between different regions within a given tumour are similar between MAP-thresholded and PCA/ICA-filtered maps (see the similarity between both maps in figure 6.1B). MAP thresholded maps were thus used

for assessment of the amplitude of fluctuations and percentage of fluctuating voxels, which would not be possible with the PCA/ICA maps because these show all voxels, regardless of their fluctuating profile (see figure 6.1B).

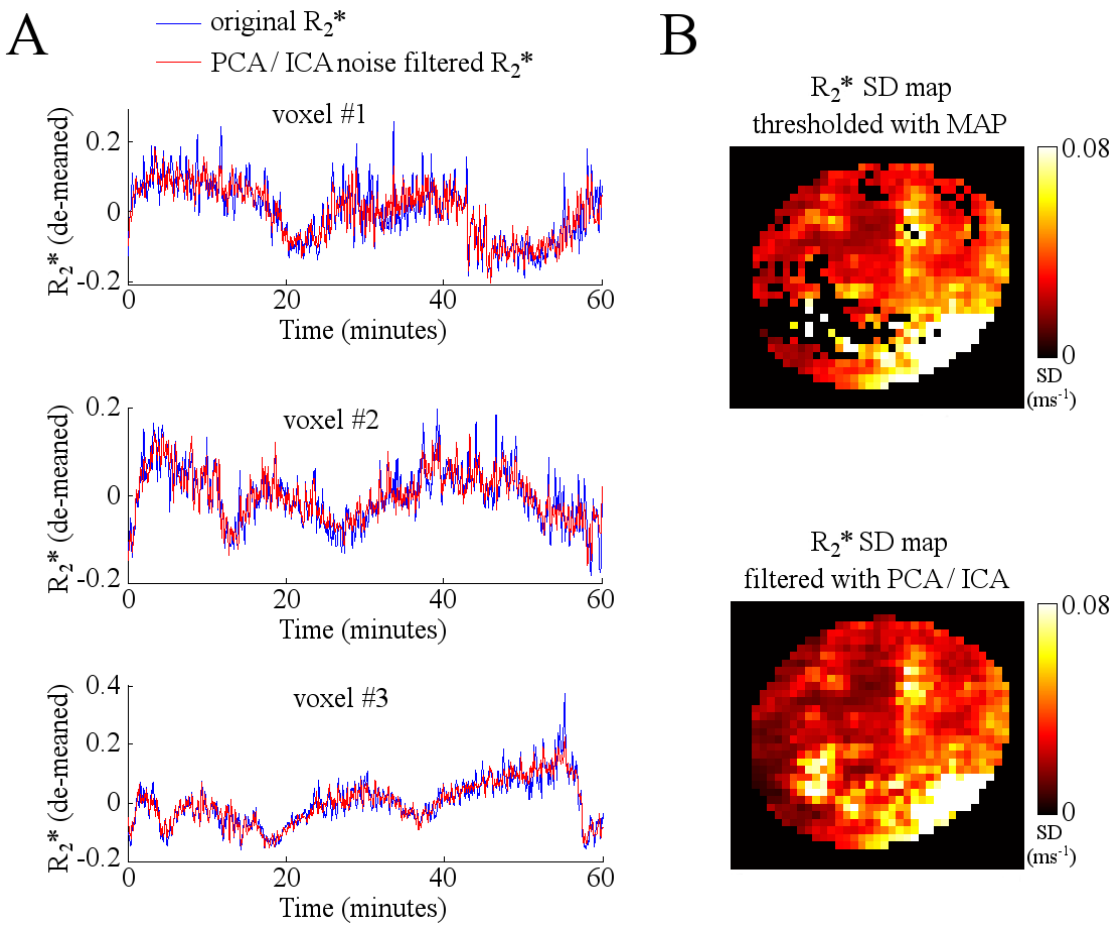

Figure 6.1 – MAP thresholding and PCA/ICA filtering on an imatinib-treated tumour at day 5. A: Original (blue) and PCA/ICA noise filtered (red) R_2^* time courses in 3 example, representative, voxels. Filtered R_2^* curves show less variability than original R_2^*, although both curves follow a similar behaviour. **B:** Corresponding standard deviation (SD) maps. Original R_2^* (MAP thresholding map) shows slightly larger SD values relative to PCA/ICA filtering. Still, relative differences are kept throughout the tumour, which can be observed by comparing both maps.

Maps of ΔR_2^* between carbogen and air breathing were calculated and thresholded as detailed in section 3.4, with the aim of estimating blood oxygenation changes. Similarly to the analysis described in Chapter 4, quantification of the maps was performed for both the percentage of voxels exhibiting a significant ΔR_2^* (positive or negative) and the corresponding mean magnitude values of these voxel locations.

Maps of ΔR_1 between carbogen and air breathing were calculated to estimate tissue oxygenation changes. Paramagnetic dissolved molecular oxygen accelerates T_1 relaxation through dipole-dipole interactions between the water protons and the molecular oxygen [105]. A paramagnetic molecule tumbling in solution creates a fluctuating magnetic field [184], therefore causing a faster T_1 recovery (i.e., shorter T_1) by increasing the likelihood of the tumbling frequency to match the precessional frequency of an excited proton (i.e., the Larmor frequency). The closer the tumbling rate is to the Larmor frequency, the more efficient the molecule is in promoting relaxation [184]. Voxel-wise ΔR_1 maps were calculated as:

$$\Delta R_1 = \frac{1}{T_{1\,Carb}} - \frac{1}{T_{1\,Air}} \quad , \qquad \text{Eq. 6.1}$$

which means an increase in tissue oxygenation upon carbogen breathing is expected to cause a positive ΔR_1. Maps of ΔR_1 were not thresholded because a statistical analysis could not be performed due to the fact that T_1 measurements are not dynamic (only one time point). This issue could be overcome by performing repeated measurements under identical conditions, although this is time consuming and not suitable to have been implemented in the current study. The percentage of positive or negative carbogen-responsive voxels and its mean ΔR_1 value were computed for all treated tumours (n = 8) and 3 control tumours.

The matrix size of ΔR_1 maps was additionally reduced to 64×64 in order to perform a correlation analysis with ΔR_2^* maps. This was aimed at assessing the relationship between tissue oxygenation and blood oxygenation estimates in treated tumours. The magnitude values of individual voxels in both maps were plotted against each other (only supra-threshold voxels in ΔR_2^* maps were considered). One plot was created for each day of MRI scanning. In each plot, voxels of all respective tumours were grouped (n = 8).

Maps of ΔSI between hypercapnia and air breathing were calculated and thresholded as detailed in section 3.4, being aimed at estimating blood flow variations. As before, the percentage of voxels exhibiting positive or negative ΔSI responses and their respective mean magnitude values were computed.

6.2.4. Histological assessment

Histology was performed as previously described for H&E and fluorescence distributions of vascular perfusion (Hoechst 33342 – blue), pericytes (α-SMA – red) and hypoxia (pimonidazole – green). Also as before, vascular endothelial cells were stained with a rat monoclonal antibody against CD31 (Abcam, UK), but now revealed with either Alexa Fluor-488 (Life Technologies, UK) or Alexa Fluor-568 (Life Technologies, UK), green or red fluorophores, respectively. Pericytes were also identified using a rabbit polyclonal anti-NG2 antibody (Millipore, UK), which was revealed with Alexa Fluor-488 (Life Technologies, UK). Tumour coverage of pericytes stained with anti-NG2 was performed as for the rest of the fluorescent markers. The percentage of capillaries covered with pericytes (α-SMA or NG2) was also calculated following the procedure described in section 3.5.

Seven treated tumours were histologically assessed. Histology was not performed on the imaged tumours of the control group because a similar analysis had been performed previously (see Chapter 4). However, pericyte staining with the anti-NG2 antibody had not been carried out and, given this necessity, a new cohort of LS174T tumours (n = 6) was set up, in which pericyte quantification was performed in this way. From these, one mouse was additionally injected with Hoechst 33342 and pimonidazole before being sacrificed. Together with earlier fluorescence distribution assessments, the sample size of each marker in the control group was: Hoechst 33342 (n = 5), pimonidazole (n = 5), CD31 (n = 10), α-SMA (n = 10), NG2 (n = 6), α-SMA coverage of blood vessels (n = 10) and NG2 coverage of blood vessels (n = 6).

6.2.5. Statistical analysis

Differences in the growth rate between treated and control tumours (assessed with MRI or calliper measurements) were assessed with a Mann-Whitney U-test in each individual day. The same test was used for assessing differences between treated and control tumours regarding quantitative distributions of histological fluorescence markers.

In order to assess the effect the administration of imatinib had on tumour MRI estimates, the longitudinal evolution of individual tumours (i.e., throughout the study days) was observed. Tumours in the control group were studied to assess if similar

effects occurred without administrating the drug. A one-way ANOVA followed by Holm-Šídák's multiple comparisons test was used to assess significant differences between days 0, 3 and 5 in treated tumours. The same test was used separately in the control group. This was performed for R_2^* spontaneous fluctuations, R_2^* response to carbogen, R_1 response to carbogen and SI response to hypercapnia. Voxel-wise correlation between ΔR_2^* and ΔR_1 responses to carbogen breathing was assessed with Pearson's linear correlation.

6.3. Results

6.3.1. Imatinib therapy did not impact on tumour growth rate or on spontaneous R_2^* fluctuations

Administration of imatinib mesylate did not affect tumour growth, as assessed by MRI or calliper measurements (Fig. 6.2). A similar observation was previously reported, in which imatinib, on its own, did not significantly delay the growth of LS174T tumours [169].

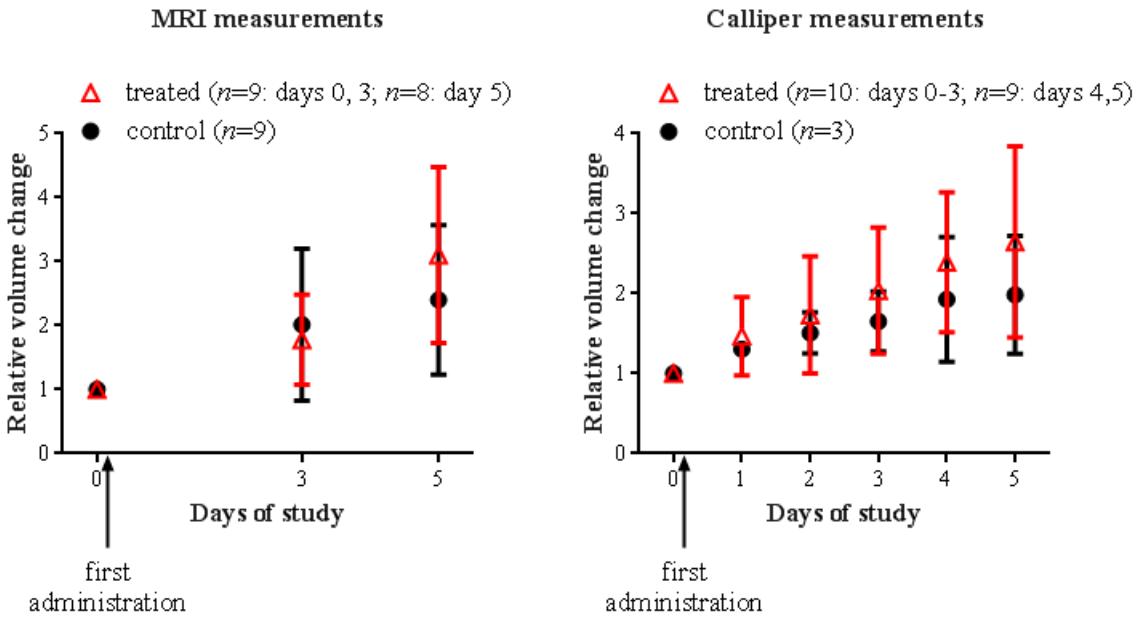

Figure 6.2 – Tumour growth in treated (imatinib) and control (saline) tumours assessed with MRI (left) and calliper (right) measurements. Imatinib or saline was first administered immediately after the baseline scan. No significant differences in growth rate between both groups were identified (Mann-Whitney *U*-test). Data are mean ± SD.

Imatinib therapy did not cause a significant change in the prevalence or amplitude of spontaneous R_2^* fluctuations throughout the duration of the study (Fig. 6.3). Upon MRI scanning, one control tumour was found to present substantial time-varying susceptibility artifacts. This tumour was not considered in dynamic MRI-related assessments.

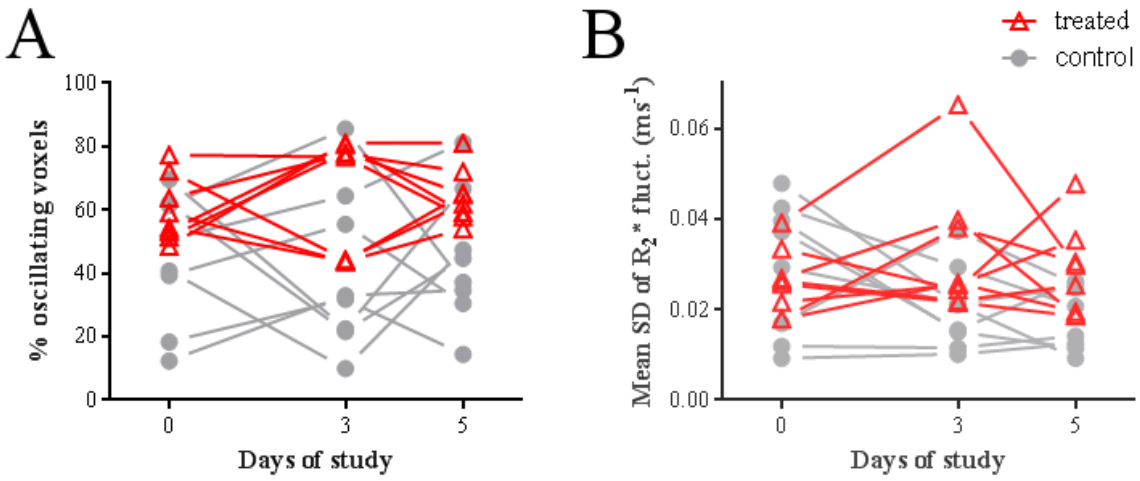

Figure 6.3 – Percentage of the tumour voxels experiencing spontaneous R_2^* oscillations (A) and corresponding mean standard deviation (SD) of such variations (B). No significant differences were found in the treated (imatinib, n = 8) or control (saline, n = 8) groups throughout the study days (one-way ANOVA followed by Holm-Šídák's multiple comparisons test).

6.3.2. Imatinib therapy promoted gas challenge response heterogeneity

Figure 6.4 illustrates the tumour R_2^* response to the carbogen challenge. Data from day 3 was omitted only for illustration purposes, but an alternative illustration containing data from the 3 scanning days is shown in the supplementary data (Fig. S6.4). The percentage of voxels exhibiting positive ($+\Delta R_2^*$) or negative ($-\Delta R_2^*$) responses did not change significantly throughout the study days, both in treated or control groups (Fig. 6.4B). The magnitude of R_2^* responses was also not significantly different between different days (Fig. 6.4C). However, an interesting effect was observed in the treated group between days 0 and 5, in which positive responses showed larger magnitudes at day 5 and negative responses presented larger negative magnitudes in the same day (Fig. 6.4C). This observation led to the investigation of the heterogeneity in the tumour response. The standard deviation (SD) of all supra-threshold ΔR_2^* magnitude values was computed, and a significant increase in the

response heterogeneity was observed in the treated group, but not in the control group, between days 0 and 5 (Fig. 6.4D). This result can be qualitatively appreciated in figure 6.4A.

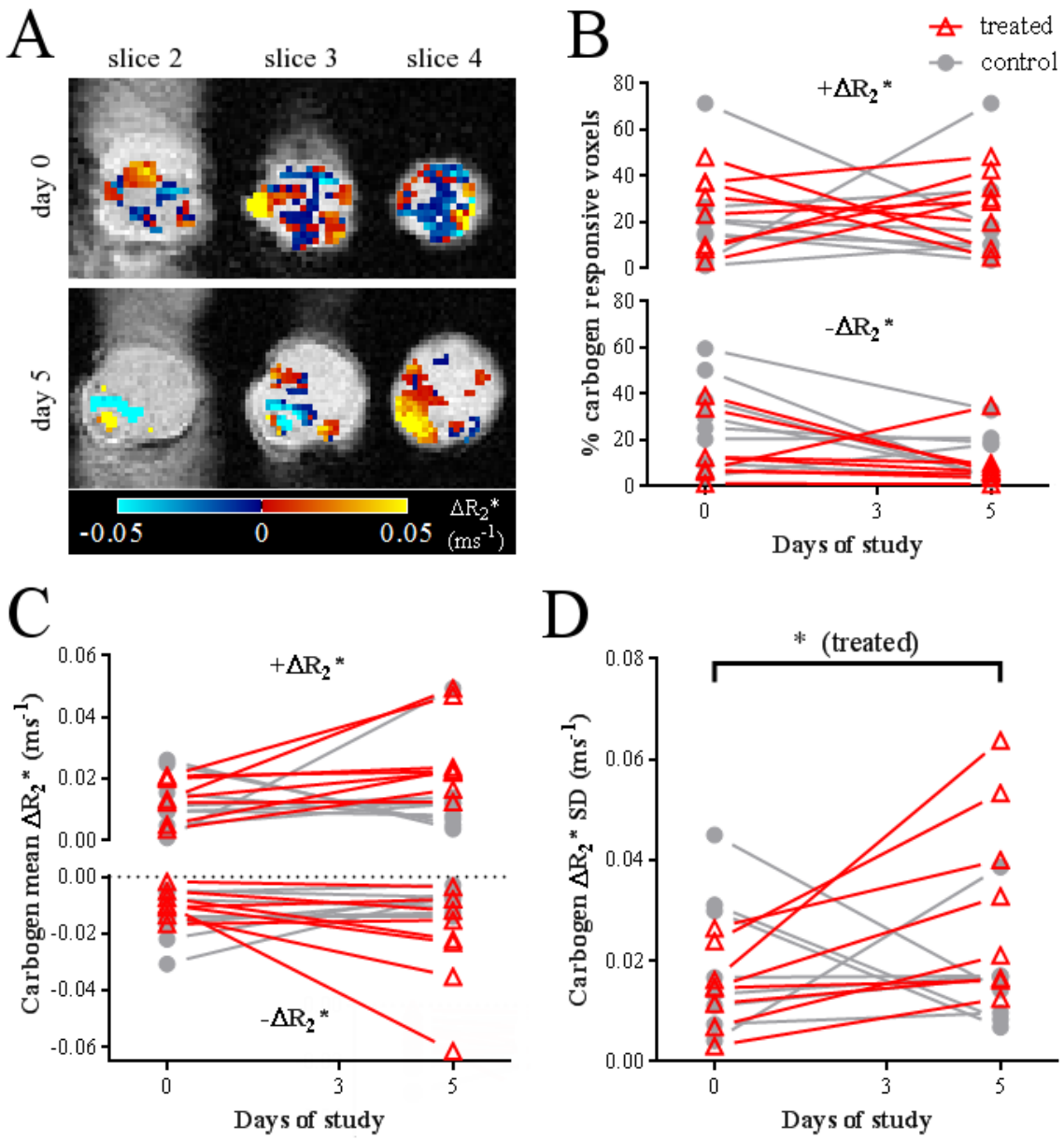

Figure 6.4 – Tumour R_2^* response to the carbogen challenge at baseline (day 0) and day 5. Significance between days of study in treated (imatinib, n = 8) or control (saline, n = 8) groups was tested with a one-way ANOVA followed by Holm-Šídák's multiple comparisons test. **A:** Representative example dataset of the effect of imatinib therapy: increase in the heterogeneity of carbogen response between days 0 and 5. **B:** Percentage of tumour voxels showing a positive ($+\Delta R_2^*$) or negative ($-\Delta R_2^*$) response to carbogen. **C:** Corresponding mean ΔR_2^* values for each treated or control tumour. **D:** Standard deviation of the magnitude values represented in **C**, depicting a significant increase in the heterogeneity of the carbogen response between days 0 and 5 in the treated group, but not in the control group. *, $P < 0.05$.

Figure 6.5 shows the tumour R_1 response to the carbogen challenge. The percentage of positive ($+\Delta R_1$) or negative ($-\Delta R_1$) responsive voxels was not significantly different between study days, both in treated or control groups (Fig. 6.5A). The corresponding ΔR_1 magnitudes were also not significantly different throughout the study (Fig. 6.5B).

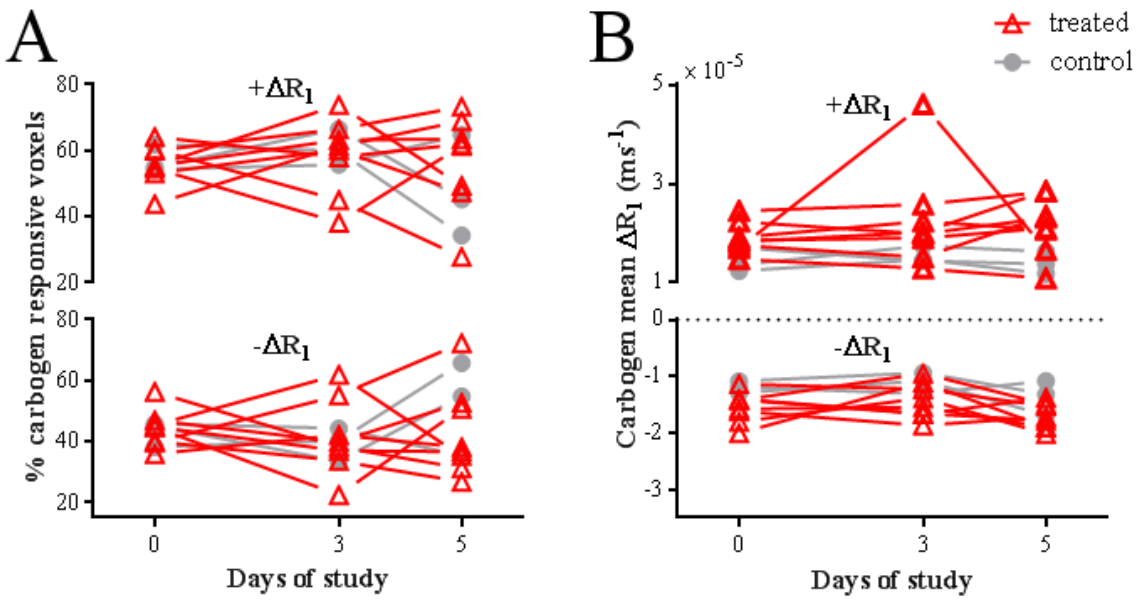

Figure 6.5 – Tumour R_1 response to the carbogen challenge at days 0, 3 and 5 in treated (imatinib, *n* = 8) and control (saline, *n* = 3) groups. A: Percentage of tumour voxels showing a positive ($+\Delta R_1$) or negative ($-\Delta R_1$) response. **B:** Corresponding mean ΔR_1 values for each treated or control tumour. No significant differences were observed throughout the study days in the treated or control groups (one-way ANOVA followed by Holm-Šídák's multiple comparisons test).

Correlation between R_2^* and R_1 responses to carbogen is represented in figure 6.6. This relationship was not significant at days 0 and 3. Day 5 revealed a significant correlation between both parameters, although with a weak correlation coefficient (R=-0.11). Still, this trend showed the anticipated relationship, in which a relatively low ΔR_2^* (high blood oxygenation) corresponds to a relatively high ΔR_1 (high tissue oxygenation).

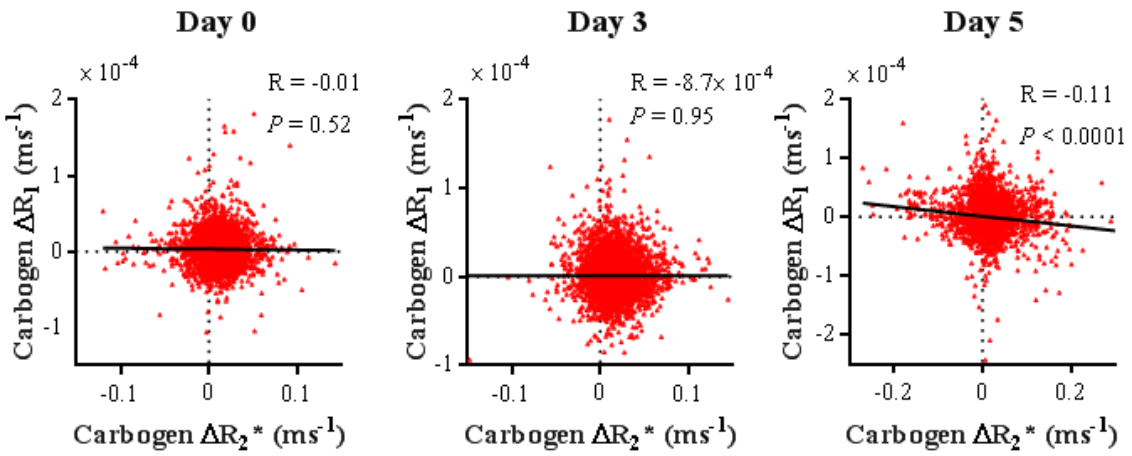

Figure 6.6 – Voxel-wise correlation between ΔR_2^* and ΔR_1 responses to carbogen breathing in treated tumours (n = 8) at days 0, 3 and 5 of the therapy study. Dots represent individual tumour voxels. Correlation coefficients (R) and significance (*P*-values) were obtained using Pearson's linear correlation.

Figure 6.7 shows the tumour SI response to the hypercapnia challenge. The percentage of responsive voxels (+ΔSI or –ΔSI) and their corresponding magnitude ΔSI were not significantly different between study days in treated or control groups (Fig. 6.7A and B). However, similarly to figure 6.4, a "mirrored" longitudinal evolution between +ΔSI and –ΔSI magnitude responses was observed in the treated group (Fig. 6.7B). Thus, the standard deviation of ΔSI magnitude values was calculated to assess the response heterogeneity to hypercapnia (Fig. 6.7C). No significant differences were observed, although there was a decrease in heterogeneity in 5 treated tumours between days 0 and 3 (no change in 3 tumours) and an increase in heterogeneity in 7 treated tumours between days 3 and 5 (decrease in 1 tumour).

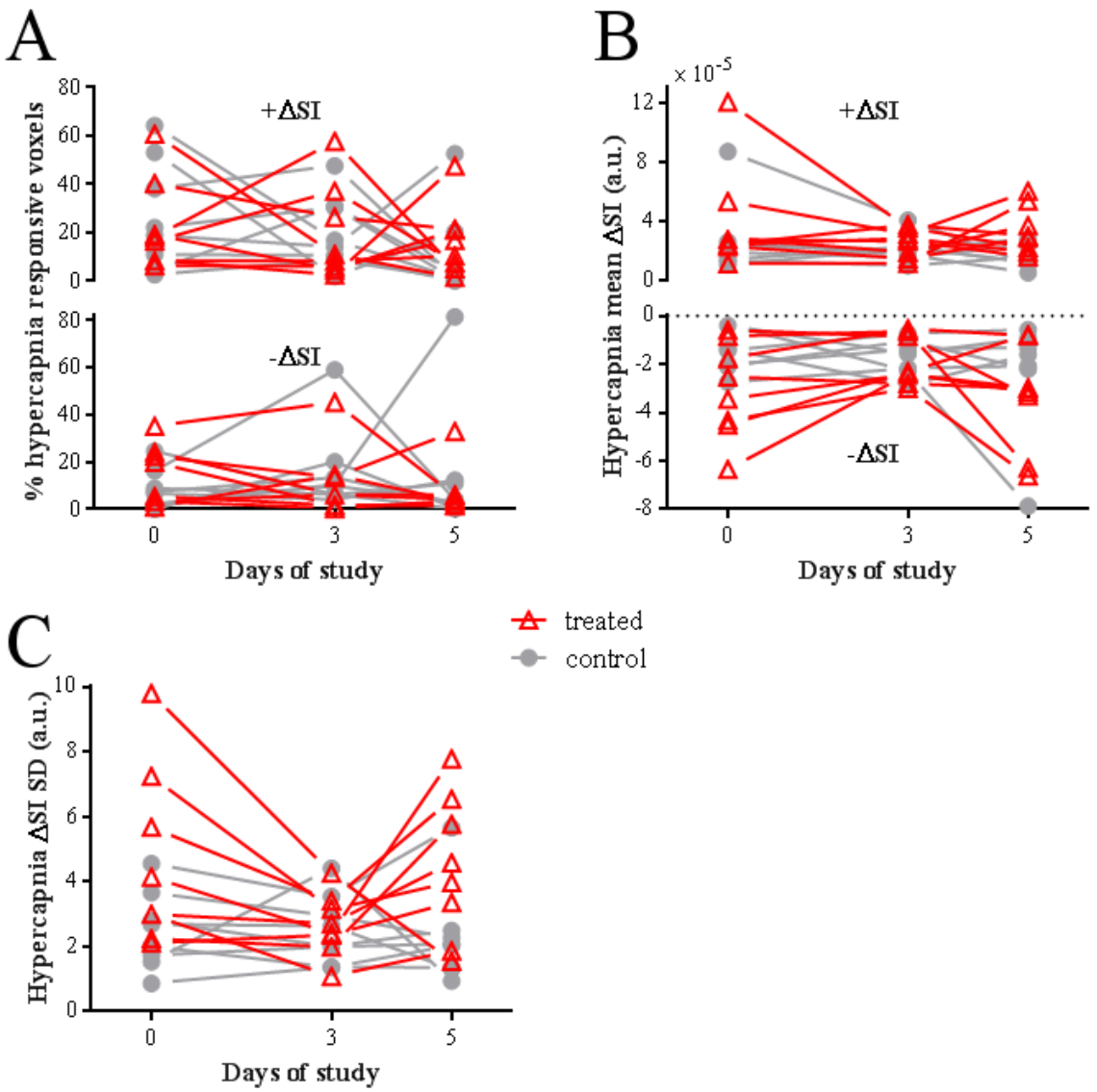

Figure 6.7 – Tumour signal intensity (SI) response to air + 5% CO_2 breathing challenge (hypercapnia) at days 0 (baseline), 3 and 5. A: Percentage of tumour voxels showing a positive (+ΔSI) or negative (-ΔSI) response to hypercapnia. **B:** Corresponding mean ΔSI values for each treated or control tumour. **C:** Standard deviation of the magnitude values represented in **B**. No significant differences were observed throughout the study days in the treated or control groups (one-way ANOVA followed by Holm-Šídák's multiple comparisons test).

6.3.3. Imatinib therapy did not normalise the tumour vasculature

Pericytes express a number of markers of differentiation and, consequently, no single marker has the ability to identify all pericytes [185]. In this study, two of these markers were used: α-smooth muscle actin (α-SMA) and NG2 chondroitin sulfate proteoglycan. The expression of α-SMA occurs in most perivascular cells (composed of pericytes and vascular smooth muscle cells), whereas NG2 is expressed on arteriolar perivascular

cells and capillary pericytes but not on venular pericytes [185;186]. Since the vasculature of LS174T tumours is predominantly composed of capillaries, both antibodies exclusively stain pericytes in this tumour type. Moreover, the expression of α-SMA is possibly dependent on endothelial release of transforming growth factor-β (TGF-β), whereas differentiation into NG2-positive pericytes is independent of TGF-β [187].

Administration of imatinib caused a decrease in the percentage of capillaries covered with NG2-stained pericytes, relative to control tumours (Fig. 6.8A and B and Fig. 6.9B). However, the percentage of capillaries covered with α-SMA-stained pericytes was similar between treated and control groups (Fig. 6.8A and B and Fig. 6.9B). This NG2-selective effect of imatinib could be due to the different factors involved in the expression of both pericyte populations. No significant differences were observed between treated and control tumours concerning the percentage tumour coverage of perfusion, hypoxia, vascular endothelial cells or pericytes (α-SMA or NG2) (Fig. 6.9A). These results combined indicate vascular normalisation did not occur with imatinib therapy.

Structurally, imatinib-treated tumours presented hyperdilated blood vessels (see Fig. 6.8A), which is potentially due to a loss of structural support given the decreased pericyte coverage (NG2). Enlarged blood vessels like these were not very commonly found in untreated LS174T tumours (see Fig. 6.8B), and when they were the dilation was not so apparent.

A qualitative analysis of the tumour morphology revealed that treated tumours presented larger areas of small, round and sparsely distributed nuclei, relative to control tumours (see Fig. 6.8C for examples of treated tumours). Cells of this morphological aspect were additionally experiencing nuclei fragmentation (Fig. 6.8C, red arrows). These observations combined suggest cells are possibly undergoing imatinib-induced apoptosis. However, an unequivocal conclusion cannot be drawn without a specific marker of apoptosis, such as caspase-3. Conversely, viable tumour cells are more densely arranged and have larger and non-spherical nuclei, being commonly located near the tumour edges or around the blood vessels (Fig. 6.8C).

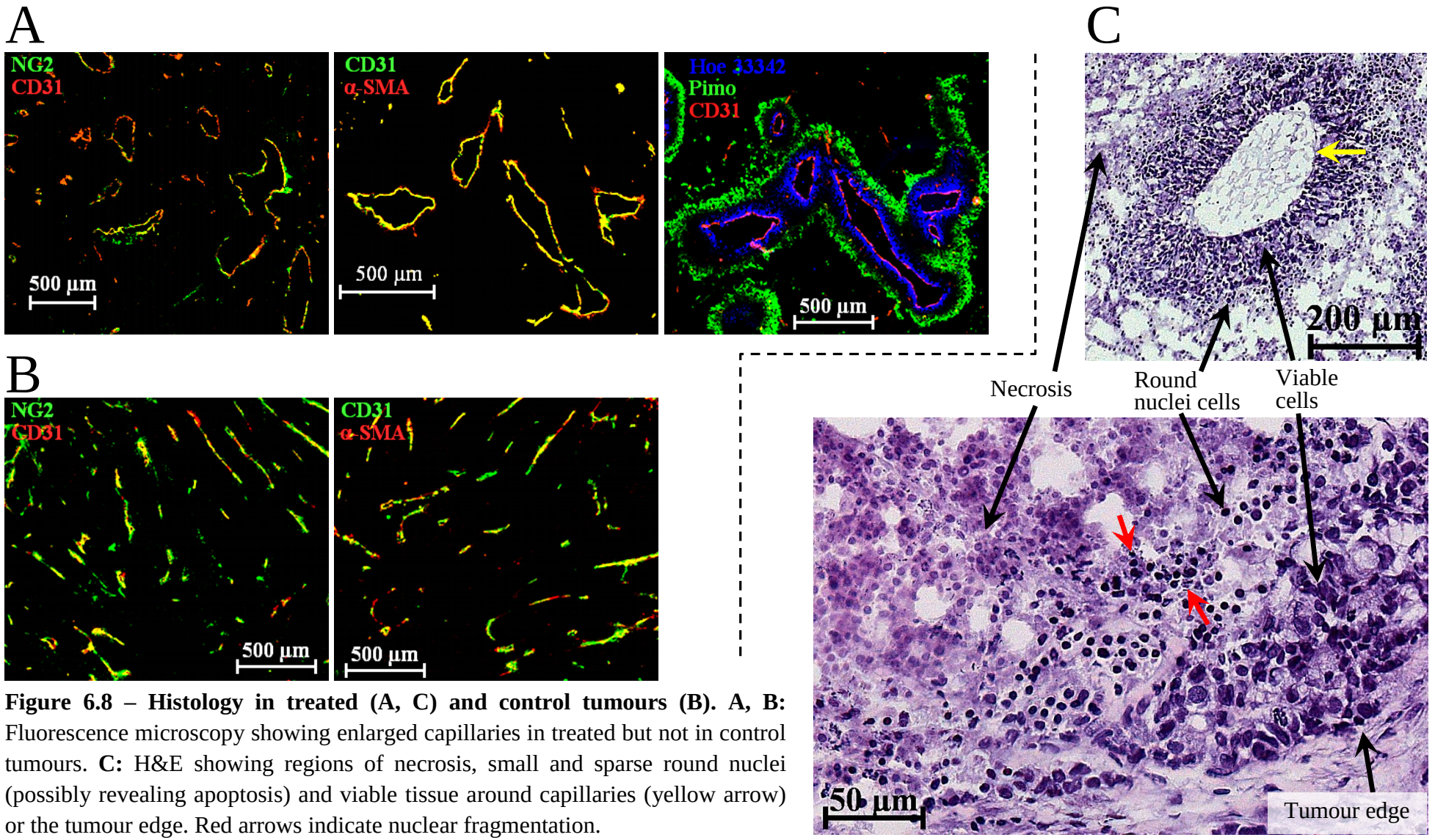

Figure 6.8 – Histology in treated (A, C) and control tumours (B). A, B: Fluorescence microscopy showing enlarged capillaries in treated but not in control tumours. **C:** H&E showing regions of necrosis, small and sparse round nuclei (possibly revealing apoptosis) and viable tissue around capillaries (yellow arrow) or the tumour edge. Red arrows indicate nuclear fragmentation.

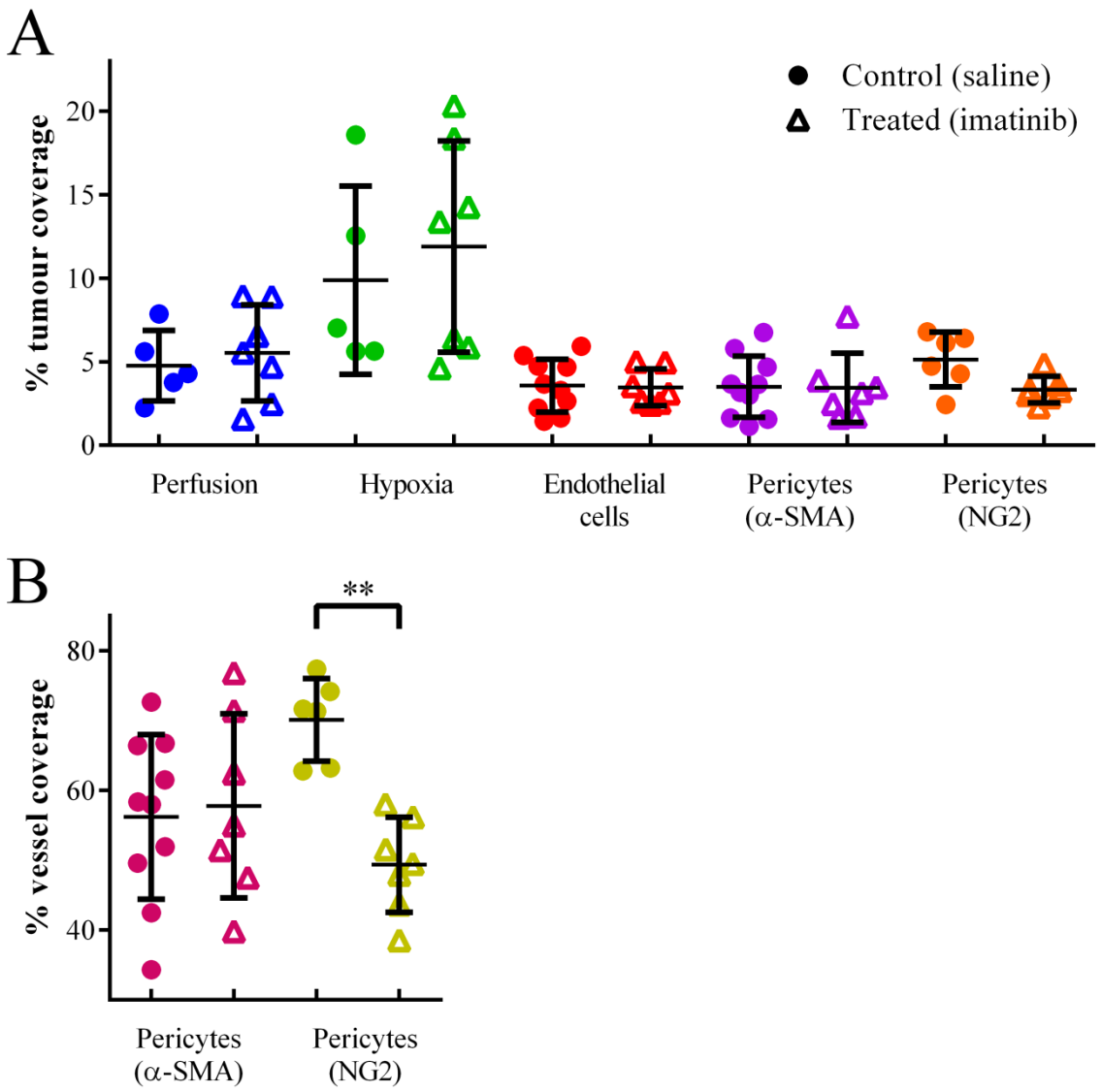

Figure 6.9 – Quantitative fluorescence histology in control and treated LS174T tumours. A: Percentage tumour coverage of perfusion, hypoxia, endothelial cells and pericytes stained with either anti-α-SMA or anti-NG2 antibodies. **B:** Percentage of blood vessels covered with pericytes. Bars represent mean ± SD. Imatinib treatment caused a significant decrease in the capillary coverage of pericytes stained with anti-NG2 but not with anti α-SMA. Significance between distributions of treated and control tumours was assessed with a Mann-Whitney *U*-test. **, $P < 0.01$.

6.4. Discussion

The antitumour drug imatinib mesylate was used in this study to assess its influence on tumour R_2^* spontaneous fluctuations and responsiveness to vasoactive gas challenges. Between LS174T and SW1222 tumour xenografts, the former was chosen because imatinib therapy previously caused an increase in antibody uptake in LS174T but not in

SW1222 tumours [165]. In the same study, the authors additionally reported that imatinib promoted pericyte detachment from endothelial cells (ECs) only in SW1222 tumours. Decreased vessel maturation opposes to the proposed hypothesis of vascular normalisation, therefore not a desirable effect in the context of this study. Moreover, LS174T tumours present moderate to poor differentiation and are less vascularised and perfused than SW1222 tumours, thus could be considered as having *a* priori a greater potential for an increase in the efficiency of its vascular network upon therapy.

6.4.1. Effect of imatinib therapy on the vascular and cellular characteristics of LS174T tumours

Quantification of histological distributions revealed that the regime of drug administration used (100 mg × kg^{-1}, once per day during 5 consecutive days) did not promote normalisation of the tumour microvasculature. Vascular pruning did not occur and perfusion and hypoxia were not different from control tumours. This result could possibly be due to the relatively short therapy window (5 days vs. 7 days in previous studies [165;169]) and/or the fact that therapy was not fractioned (half-life of imatinib is approx. 4 hours in mice [188], meaning a fractioned dose is more effective [169]). In accordance with this previous knowledge, the planned length of this study was 9 days, although issues with ulceration in some tumours caused the experiment to be shortened. Also, fractioned dose proved to be challenging to implement due to the length of the MRI scans.

Contrary to what was previously reported for LS174T tumours, the vascular coverage of pericytes (expressing NG2) decreased upon therapy, which is in agreement with the observation that imatinib inhibits the PDGF pathway in this tumour line [169], further disproving the normalisation hypothesis. Differing observations regarding the effect of imatinib on LS174T vessel maturation could be due to differences in the employed quantification methods: in the present study the percentage of pericyte coverage was calculated, whereas Rajkumar *et al.* [165] calculated the Pearson's correlation between the colocalisation of endothelial and pericyte marker staining. Disruption of the pericyte-EC contact resulted in blood vessel hyperdilation. This effect was previously observed with an inhibitor of PDGF receptor (PDGFR), where the authors concluded that tumour pericytes, albeit less abundant or more loosely attached

relative to normal vasculature, still have an important role in maintaining vascular integrity and function [187].

Decreased pericyte coverage is likely to increase leakage into the extravascular space [189] and, consequently, increase the interstitial fluid pressure (IFP). However, PDGF is a critical regulator of IFP [182;183;190] and imatinib-mediated inhibition of its receptor was shown to decrease IFP and hypoxia in LS174T tumours [169]. The fact that this study did not reveal changes in the percentage of hypoxia staining upon treatment possibly results from these two antagonistic effects cancelling each other.

A previous study has also shown that absence of vascular normalisation occurred in other tumour models with a number of angiostatic compounds [191]. Normalisation is therefore dependent on the combination of compound + tumour type. Consequently, it is also worth to keep in mind that imatinib might not be a drug that straightforwardly promotes vascular normalisation, at least in LS174T tumours.

The observed effects of imatinib therapy on the tumour cellular characteristics are more challenging to interpret. Histological sections of H&E revealed what can possibly be an increase in apoptosis observed across large areas of the tumour. Imatinib is a PDGFR inhibitor that targets the tumour vasculature and, accordingly, inhibition of PDGFR was previously observed to increase endothelial cell apoptosis [187]. Still, the majority of the observed non-viable cells distributed in the tumour stroma are unlikely to be of vascular nature. So why were non-endothelial cells affected? Imatinib additionally targets tyrosine kinases involved in signal transduction pathways, like Bcr-Abl and c-kit receptor [153], and it was previously shown that imatinib-mediated inhibition of the c-kit pathway induced apoptosis in a human colon adenocarcinoma cell line (LS180) [192]. Given that LS174T tumours are also a c-kit-positive human colon adenocarcinoma cell line [193], it is conceivable that imatinib could have had a similar apoptotic effect in the current study.

6.4.2. Effect of imatinib therapy on spontaneous R_2^* fluctuations

Imatinib therapy did not affect the percentage of oscillating voxels or the amplitude of R_2^* fluctuations. Baranowska-Kortylewicz *et al.* [169] showed that imatinib can decrease IFP through blockade of PDGFR. In such circumstances, the amplitude and/or prevalence of R_2^* variations are expected to decrease due to their dependence on raised

IFP. However, as mentioned above, it is not obvious that imatinib caused IFP decrease in the current study, due to the pericyte-EC dissociation and likely increase in vessel permeability. If IFP remained unchanged with therapy, it provides an explanation for the lack of therapeutic effect in R_2^* fluctuations.

Additionally, the fact that spontaneous R_2^* fluctuations were not affected despite the decrease in vessel maturation combined with the result of Chapter 5 of an inverse relationship between the amplitude of tumour-specific fluctuations and vessel maturation, suggests that vasomotion of mature vessels has little effect in generating flow/oxygen fluctuations in LS174T tumours. Perhaps the pericyte-EC contact is strong enough to regulate the vascular structure but still excessively loose in order to exert vasoconstrictive effects. Blood flow/oxygen spontaneous fluctuation independence from vasomotion could thus help explain the absence of therapeutic effect.

6.4.3. Effect of imatinib therapy on the tumour response to applied gases

Administration of imatinib revealed interesting results regarding the gas challenge responses, although of no straightforward interpretation, and drew attention to the importance of localised, rather than generalised, effects.

An increase in the heterogeneity of ΔR_2^* upon carbogen breathing was observed at 5 days following treatment. Relying on histological observations, vessel hyperdilation could be thought of leading to increased blood volume, which could increase the tumour's capacity for oxygen transport, resulting in a greater negative ΔR_2^*. In turn, stronger responses to the challenge increase the potential for vascular steal effects from the nearby vasculature, causing a greater positive ΔR_2^*. A combination of these effects could therefore explain the increased heterogeneity in the R_2^* response to carbogen.

A decrease in the heterogeneity of the ΔSI response to hypercapnia at day 3 was also observed, albeit non-significant. Imatinib reduced the vascular coverage of pericytes, potentially causing a smaller positive ΔSI via loss of muscle tone. This weaker response has the potential consequence of decreasing the amplitude of negative ΔSI responses due to vascular steal effects. These two effects combined provide an explanation for the reduced heterogeneity in ΔSI at day 3. The early effect of imatinib on the hypercapnia response was reversed at day 5, which could be related to previous reports of "windows" of therapeutic efficacy in the first few days of treatment with antiangiogenic

drugs, after which the tumour recovers to the initial state (see a review on ref. [194]). Two factors could be casing the window's closure: excessively high or prolonged dosing or emergence of drug resistance [194].

Imatinib did not cause a significant change in the R_1 response to the carbogen challenge throughout the study. Additionally, correlation between carbogen ΔR_2^* and ΔR_1 revealed non-significant or weak relationships. Similarly to the data presented in Chapter 4, these results might be due to uncertainty in the measurement estimates, possibly because of background noise, which causes additional scatter. Concerning the R_1 data in particular, uncertainty could also be due to sub-optimal imaging parameters. O'Connor *et al.* [195] performed a conceptually similar experiment, in which they compared R_2^* and R_1 responses to carbogen and oxygen inhalation in patients. They observed significant R_1 increases with the gas challenge in a number of organs, indicating R_1 mapping can be used to monitor the molecular oxygen status. Of note, oxygen dissolved in blood plasma, apart from that in tissue fluid, also influences the R_1 relaxation rate. Still, ΔR_1 response upon a hyperoxic gas challenge is dependent on several physiological processes, like arterial blood flow, arterial blood volume and tissue metabolism [195], which can further influence measurement uncertainty in tumours due to their inherent heterogeneous microenvironment. Furthermore, tumour areas responsive to carbogen could have also varied between R_2^* and R_1 acquisitions due to variations in the perfusion status, providing an additional explanation for the poor correlation results.

6.5. Conclusions

This study aimed to assess the effect of the antitumour therapy imatinib mesylate on the LS174T tumour spontaneous R_2^* fluctuations and responsiveness to vasoactive gas challenges. It was additionally hypothesised that imatinib could potentially promote a "vascular normalisation" effect, similarly to what has been observed with other antiangiogenic drugs. The results revealed that imatinib, as administered here, does not promote the normalisation of the vasculature in LS174T tumours. Consequently, the amplitude and prevalence of R_2^* fluctuations remained unchanged. Also, responsiveness to gas challenges did not reveal a generalised effect, rather emphasized the importance of local effects which influenced response heterogeneity.

Despite the results of this study, previous reports suggest that imatinib is a drug with great potential. If the therapy protocol can be fractioned and of greater duration, it is possible that it can have a more desirable effect towards an evolution of the tumour microenvironment that can decrease spontaneous oxygen fluctuations and better respond to secondary therapies.

7. Resting state R_2^* as a biomarker for prostate tumours: a clinical study

The dynamic gradient-echo MRI (GE-MRI) sequence used in Chapters 4 to 6 was adapted to a translational study, where R_2^* fluctuations were investigated as a method of discriminating early-stage prostate tumours from healthy tissue. The realisation of the potential of this MRI technique in the characterisation of the preclinical tumour microenvironment led to the assessment of its suitability in identifying tumours in the prostate in the clinical setting. This study was carried out in collaboration with Dr. Shonit Punwani, Dr. Catherine Morgan and Nicola Stevens (University College Hospital), where I contributed to the design of the study and performed the post-processing of the MR data, including the implementation of independent component analysis for the first time in prostate studies.

7.1. Introduction

Prostate cancer is the most common and the second most deadly cancer among UK men [196]. Prostate biopsy guided by ultrasound remains the gold standard for diagnosing prostate cancer [197]. Although providing histopathological evidence, this technique suffers from a number of limitations. Perhaps the greatest drawback is due to the fact that prostate cancer is generally multifocal, whereas only a small portion of the prostate is sampled, which does not guarantee confirmation of tumour disease and causes large cancers to be under-evaluated [197;198]. In fact, prostate biopsy mainly samples the most posterior 18 mm of the gland, and it usually fails to include the anterior part, where about 20% of cancers develop [197;199]. Conversely, the fact that prostate biopsies are usually directed in a "blind fashion" causes millimetre-sized cancer foci to be detected, which do not usually represent clinically significant cancers [197].

To overcome the limitations imposed by blind biopsies, multiparametric MRI of the prostate has become an important tool in the diagnosis, evaluation and treatment planning of prostate cancer [197]. In any given patient, a T_2-weighted morphological sequence, a diffusion imaging sequence, and a dynamic contrast-enhanced (DCE) T_1-weighted sequence are commonly used to characterise different aspects of the tumours [197;200]. Spectroscopy sequences may also be employed [197;200]. The combination of T_2-w, diffusion and perfusion imaging led to a diagnostic precision between 85% and

87% in a number of studies (see a review in ref. [197]). However encouraging, these results indicate there is still room for improvement. The current study describes an attempt to improve on early detection of prostate tumours using dynamic GE-MRI R_2^* measurements. The evidence that tumours exhibit R_2^* temporal fluctuations, combined with the dynamic and non-invasive characteristics of this imaging protocol, justifies undertaking an assessment of its diagnostic performance.

Early tumour detection is fundamental to improve disease survival, and so the aim of this study was to investigate whether tumour R_2^* spontaneous fluctuations occur in a clinical setting. If true, the potential of such fluctuating behaviour to be a biomarker of malignancy can be assessed.

7.2. Materials and methods

7.2.1. Patient cohort

Patients with elevated levels of prostate-specific antigen (PSA) serum are at risk of developing prostate cancer [198;200]. Accordingly, the cohort of this study was composed of 20 male patients (mean age 65.85, range 58-79 years) with PSA concentration usually above 4.00 ng/ml (mean 7.03, range 1.40-15.00 ng/ml). Patients 2 and 3 presented low PSA levels (2.00 and 1.40 ng/ml, respectively) but were still approved for this study by the medical staff. A table with each patient's information is shown in supplementary data (Table S7.1). Twenty two patients were initially scheduled, although patients 5 and 18 did not proceed with the template biopsy and were therefore excluded from analysis. Patients were informed of the study and signed consent was given prior to their enrolment.

7.2.2. MRI imaging protocol

Multiparametric MRI of the prostate was performed on a Philips Achieva 3.0 T 60 cm horizontal-bore system (Philips Medical Systems, Best, The Netherlands). Anatomical T_2-weighted images were obtained, alongside maps of apparent diffusion coefficient (ADC) (Fig. 7.1A, B) and DCE, for tumour localisation. Before DCE acquisition, a 15-minute dynamic GE-MRI sequence was also obtained to assess R_2^* temporal variations. GE sequence parameters were: *TR = 200 ms, 5 echoes, TE_1 = 20*

ms, echo spacing = 3.5 ms, in-plane field of view 256×256 mm^2, matrix size 128×128, slice thickness 2 mm, spacing between slices = 5.39 mm, 5 slices, flip angle = 20°, 22.5 s/image.

7.2.3. MRI data analysis

Regions of healthy prostate (n = 24 regions) and prostate tumour (n = 16 regions) were selected upon analysis of multiparametric MRI data by an experienced radiologist. Tumour lesions were subsequently confirmed with a biopsy. Maps of R_2^* SD were calculated as described in section 3.4, where healthy and tumour regions were then reproduced.

Occurrence of rectal peristaltic movements, which can produce motion artifacts, was assessed by observing cine images of raw T_2^*-w data (Fig. 7.1C, a). Independent component analysis (ICA) was then implemented as a strategy to eliminate such artifacts. ICA was applied to the whole prostate volume. Differences in MR acquisition parameters between pre-clinical and clinical data meant some adaptations had to be performed to the ICA decomposition procedure described in Chapter 5. Dimensionality reduction with PCA was not employed in the prostate data because even the last principal components showed relevant information. This resulted from the small number of time points (40 *vs.* 944 in the pre-clinical datasets), which meant only 40 principal components could be generated. Few data time points also made it harder to judge the nature (noisy/non-noisy) of each independent component. This, associated to the fact that healthy prostate regions do not necessarily experience blood flow/oxygenation fluctuations, prompted the decision to eliminate only those independent components that were suspect of modelling artifacts. This was performed based on the presence of spikes in their time courses. Figure 7.1C, b shows an example of one such artifactual independent component and its spatial map, showing a clustering effect in the same region of the motion artifact (previously observed in Fig. 7.1C, a). This artifact is clearly visible in the original R_2^* SD map (Fig. 7.1C, c), but not in the ICA-filtered R_2^* SD map (Fig. 7.1C, c). The effect of removing artifactual components is also obvious upon observation of individual R_2^* voxel time courses (Fig. 7.1 C, c), where the spike at the time of motion (time-point 32) was eliminated. On average, 27.45 out of 40 independent components were chosen.

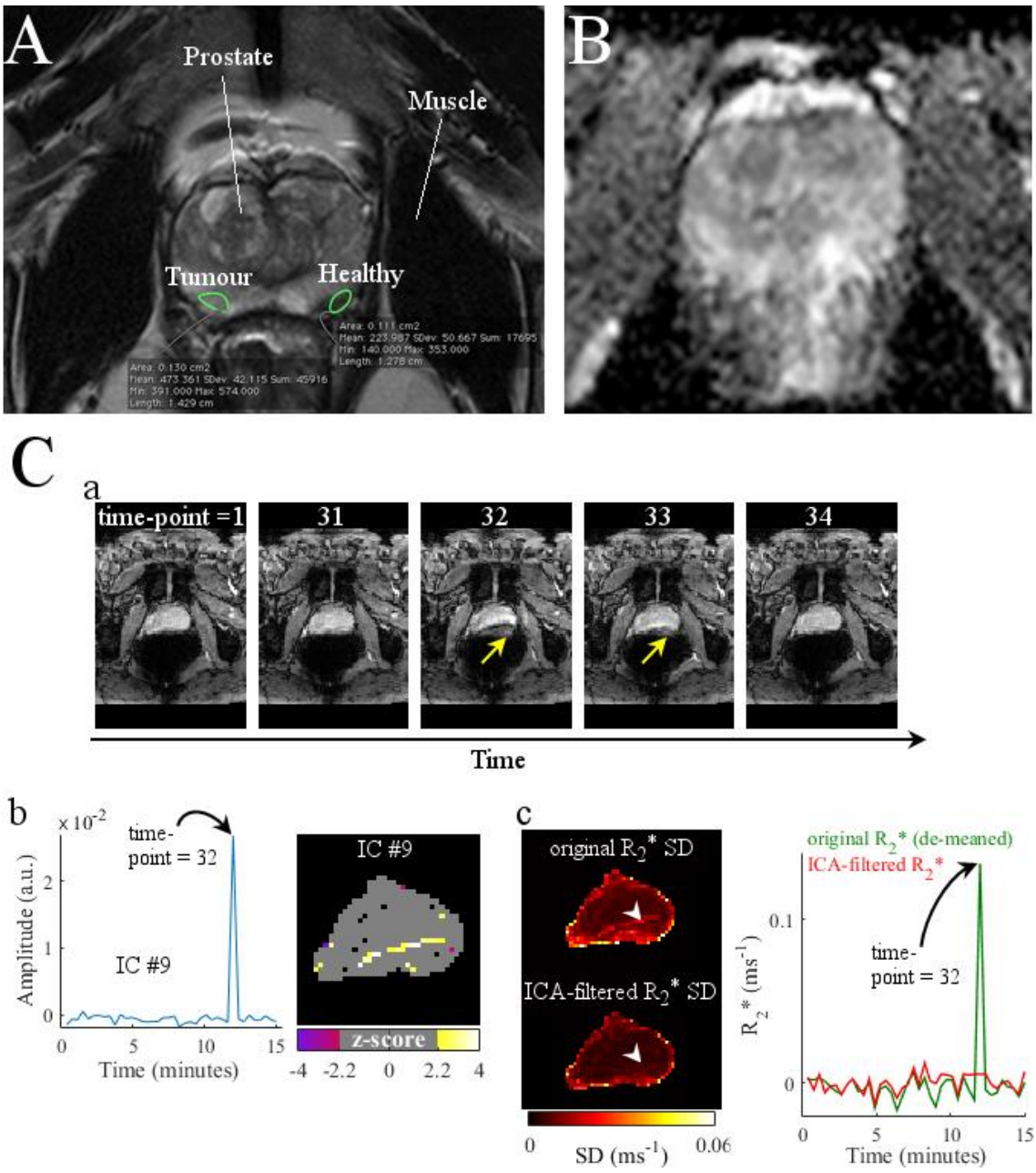

Figure 7.1 – Post-processing strategy. Identification of healthy and early-stage tumour regions in the prostate was carried out by observation of T_2-weighted images (**A**) and ADC maps (**B**), and posteriorly confirmed with a biopsy. **C:** Detection and elimination of motion artifacts. **a:** Prostate motion was observed in cine images of raw data (see yellow arrows). **b:** Time course and respective spatial map of one example independent component (IC #9), found to be modelling motion of the prostate: a peak above the time-course baseline and corresponding spatial clustering were observed. **c:** Elimination of such ICs resulted in decreased artifactual R_2^* temporal variation. Original (green) and ICA-filtered (red) R_2^* time courses of the voxel identified by the arrowheads are shown.

Mean R_2^* SD values were calculated for each tumour region and its corresponding healthy region (n = 16) to assess if there was a significant difference in the amplitude of R_2^* fluctuations between them. Healthy prostate regions that did not have corresponding tumour lesions were not considered in this assessment, in order to exploit the paired nature of the statistical test used. Statistical differences were assessed with the Wilcoxon matched-pairs tests.

R_2^* time courses of healthy (n = 24) or tumour (n = 16) regions were also assessed in the frequency domain using the Lomb method. As before, for each dataset, spectra of individual voxels were combined into a single averaged spectrum. The spectral mean and standard deviation of the cohort was then computed.

7.3. Results and Discussion

Figure 7.2 shows the difference between R_2^* SD values of healthy and prostate tumour regions, which was not significant. Observation of individual independent component spatial maps also did not reveal any clustering effect in the selected regions of interest. The power spectra of R_2^* time courses was also similar between healthy and tumour areas (Fig. 7.3).

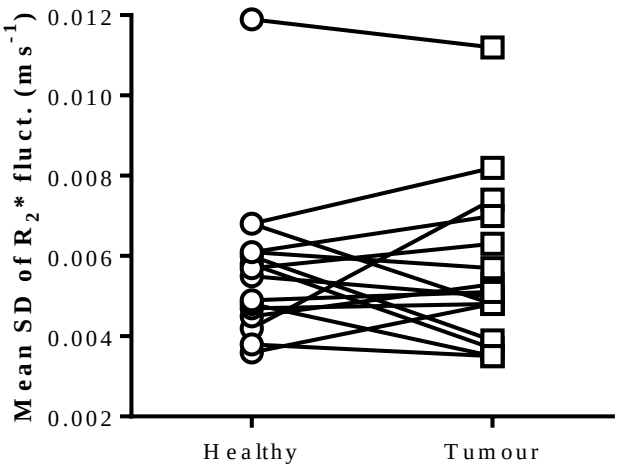

Figure 7.2 – Mean standard deviation (SD) of R_2^* time-courses in healthy and tumour regions of the prostate (n = 16). No significant differences were observed (Wilcoxon matched-pairs test).

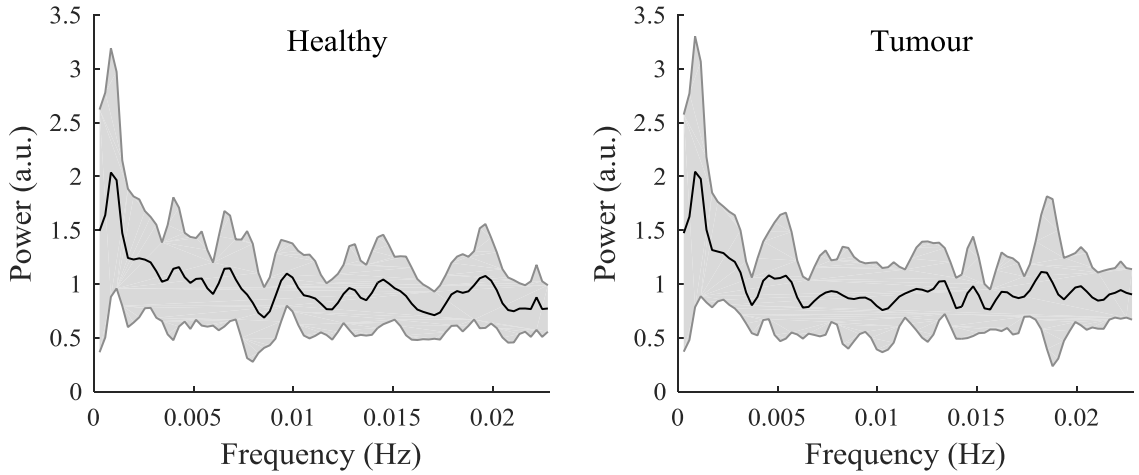

Figure 7.3 – Frequencies of R_2^* variation in healthy (n = 24) and tumour (n = 16) regions. Mean (black line) and standard deviation (shaded area) of power spectra are shown. Spectra do not reveal differences between the R_2^* dynamics of healthy and tumour regions.

These observations indicate that dynamic R_2^* measurements of the prostate, as implemented here, are not sensitive enough to detect early-stage tumours of the prostate, and are therefore not yet suitable to be used as a biomarker of tumour disease in the clinic. Reasons for this lack of differentiation might include the fact that cycling hypoxia has been identified in advanced stages of tumour progression; hence, it might not yet be present in the early stages of tumour development. In addition, studies on cycling tumour hypoxia in humans are still scarce, which means the clinical reality of this problem might present considerable differences in relation to the pre-clinical situation. Consequently, as the MRI protocol implemented here was directly adapted from the pre-clinical protocol, it is possible that the parameters used in this study were sub-optimal in the detection of R_2^* prostate tumour spontaneous fluctuations. One limitation of this study was that drawing of regions of interest on maps of R_2^* SD possibly suffered from lack of accuracy. This could be overcome by co-registering T_2-w images, ADC maps and DCE maps to R_2^* SD maps. Other limitations consisted of involuntary motion artifacts due to rectal peristalsis and low sampling rate or insufficient scan length. These could be addressed by considering a clinical situation in which the tumours do not suffer from such neighbouring motion (e.g. brain), and also by increasing the number of acquisition points, mainly by increasing the sampling rate

to allow clinical practice feasible, aiming to help to improve the distinction between oscillatory and noise-modelling independent components.

8. Conclusions and future directions

Hypoxia, either chronic or cycling, has been found to occur in solid tumours, causing resistance to treatment and is also associated with tumour progression and development of metastatic disease. However, between both types of hypoxia, several comparative studies found the cycling form to be more severe and the one that appears to be present to a greater extent in tumours. For these reasons, and due to its oscillatory nature, which makes it more easily measurable with MRI, cycling hypoxia was made the focus of this research, while looking for associations between these transient patterns and tumour pathophysiology.

Two studies by Baudelet *et al*. [34;41] provided the starting point for this thesis. The initial approach, here implemented in Chapter 4, consisted in adapting their 'resting state' and 'gas challenge' protocols to subcutaneous colorectal tumour xenografts. A major difference was the use of R_2^* estimates instead of signal intensity recordings from T_2^*-weighted images. R_2^* transverse relaxation rates directly depend only on the oxygenation of the blood and not on blood flow, therefore helping in the interpretation of the data. Spontaneous R_2^* fluctuations were detected in SW1222 and LS174T tumours, suggesting the occurrence of cycling levels of oxygenation. The longitudinal imaging protocol revealed that some aspects of spontaneous fluctuations depend on the stage of the tumour development, such as their oscillatory frequencies, whilst others do not, such as their prevalence. The vasoactive carbogen challenge differentiated between well and poorly perfused tumour types, which is in agreement with histological distributions, and where perfusion status revealed to be a determining factor in the evolution of the carbogen response with the growing tumour. Gas challenge responses that were opposite to those expected were also observed. These effects are challenging to interpret and are probably the result of the chaotic nature of the tumour microenvironment. This chaotic nature constitutes an inherent limitation in tumour studies, being a major source of temporal and spatial variability, which would have also impaired the correlation assessments between spontaneous R_2^* fluctuations and gas challenge responses. Another limitation relates to spatial co-registration issues between histological images and MRI maps due to the considerable difference in resolution, which prevented the quantification of the relationships between their spatial distributions.

Potential future steps to overcome some of these limitations or explore further relationships consist of: implementation of a quantitative MR sequence sensitive to blood flow to shed new light on the gas challenge response heterogeneity, pulse sequence modifications to increase measurement accuracy, assessment of the relationship between glucose consumption/lactate production and cycling hypoxia, and assessment of the influence of the tumour site on the structural and functional properties of the tumour.

Several studies hypothesised that tumour gas challenge responses revealing opposite variations to the *a priori* assumptions could be due to 'vascular steal' effects. These effects consist in a diversion of blood flow from a given tumour region due to increased blood flow in adjacent regions or in the feeding vasculature. Arterial spin labelling (ASL) is an established non-invasive quantitative MR technique that allows the estimation of blood flow and, if applied to tumours, could potentially identify the areas more susceptible of suffering from steal effects. In fact, efforts at our laboratory (the UCL Centre for Advanced Biomedical Imaging (CABI)) already allowed perfusion measurements in colorectal tumour liver metastasis, and discrimination relative to the surrounding liver tissue [201]. Ultimately, these maps would be compared with maps of R_2^* to investigate the relationship between tumour regions presenting opposite R_2^* response and blood flow redistribution.

One additional source of measurement variability is its associated uncertainty. Although resting state and gas challenge maps were thresholded, there might have remained some residual uncertainty that could have affected the R_2^* estimates. One way to decrease measurement uncertainty under noise is to increase the sampling rate (i.e., oversample) by decreasing the repetition time (TR). This would probably improve R_2^* estimation performance and could have a measurable effect in improving the correlations between spontaneous R_2^* fluctuations and gas challenge responses.

An interesting study would be to explore the hypothesis of Gatenby and Gillies [76], that the tumour switch to the glycolytic pathway is an adaptive response to cycling hypoxia. A non-invasive MR method was recently developed at our laboratory which allows the imaging of glucose uptake *in vivo* in tumours, named glucoCEST [202]. A protocol which included glucoCEST and dynamic gradient-echo measurements would allow the assessment of the relationship between glucose uptake and the occurrence of R_2^* spontaneous fluctuations in tumours. Alternatively, monitoring the production of

lactate with proton MR spectroscopy, both with single-voxel and multi-voxel techniques (e.g., chemical shift imaging (CSI)), would allow the assessment of the evolution of the tumour glycolytic activity [203]. A second alternative would consist of using a recent technique, dynamic nuclear polarisation (DNP), which can increase the sensitivity of the MR spectroscopy experiment by 10000 fold, and can assess the tumour metabolism by mapping the flux of hyperpolarised ^{13}C between pyruvate and lactate [204].

Finally, an appropriate alternative tumour site of implantation would probably more accurately mimic the clinical reality. Subcutaneous tumours are a good initial approach because of their reproducibility and relatively simple induction protocol. However, it was shown that the tumour site of implantation affects the vascular properties of the tumour [205]. Orthotopic tumour models are considered more clinically relevant and better predictive of therapeutic efficacy than subcutaneous xenograft models. In orthotopic tumours, the cancerous cells are implanted directly in the organ of origin, so that the tumour microenvironment more closely resembles the original clinical situation.

Chapter 5 described a study aimed to investigate if tumour spontaneous R_2^* fluctuations were influenced by blood oxygen variations in the systemic vasculature. It comprised the implementation of independent component analysis (ICA), a computational blind source separation technique extensively used in brain studies, which was here adapted to tumour data for the first time. Together with concomitant measures of systemic blood oxygenation, ICA applied to R_2^* tumour maps allowed the identification of temporal variations that were due to systemic influence, as well as tumour-specific fluctuations. Importantly, ICA provided the ability to identify tumour regions that were simultaneously suffering from systemic and tumour-specific effects, which is a major advantage in relation to direct correlation approaches. Here, it is important to acknowledge that correlation analyses can represent a rather simplistic approach, and the analysis of multi-echo GE data in this study would merit the (alternative) implementation of a model-based strategy, such as with a General Linear Model (GLM), either on its own or in combination with ICA. Separation between systemic and tumour-specific sources of R_2^* fluctuation revealed links to tumour pathophysiology, namely the tumour size and vascular maturation. The method here described has the potential to be adapted to the human condition, where it could help predict the delivery of systemically applied therapies in individual patients, and therefore help planning the delivery regime accordingly. Limitations of this study include the non-modelling of any possible lag between the systemic and tumour

recordings, which could have impaired the correlations. Also, tumours possibly suffer from a number of systemic influences, and so only by simultaneous measurement of all these systemic variations it would be possible to thoroughly assess the systemic influence in the tumour oxygen fluctuating patterns.

Future work regarding the study presented in Chapter 5 includes a longitudinal study to assess the evolution of the systemic influence and the evolution of tumour feeding vasculature with the growing tumour.

Following on the result of Chapter 4 that SW1222 tumours show more widespread response to carbogen breathing with the growing tumour, suggesting increased susceptibility to systemic variations, and on the result of Chapter 5 that revealed a link between tumour size and systemically-driven fluctuations, it would be interesting to apply the ICA method to a longitudinal study. Simultaneous acquisition of systemic physiological parameters and tumour 'resting state' R_2^* in a longitudinal fashion would allow to confirm if the percentage of the tumour oscillating due to systemic effects does in fact increase with the tumour size.

Related to the above suggestion, a longitudinal study on the evolution of the tumour supplying vasculature would provide valuable insights on the influence of systemic sources of cycling hypoxia in the tumour, which could be through an increase in the number of systemic feeding vessels, an increase in the calibre of such vessels, or both. ASL measurements could additionally be taken to quantify the evolution of blood flow entering the tumour.

Chapter 6 described a therapy study, with the agent imatinib, conducted under the hypothesis of "vascular normalisation", i.e., decrease in the tumour vascular density alongside structural and functional improvement of the remaining capillaries. Histological assessment revealed that imatinib therapy did not promote normalisation of the vasculature. Consequently, the prevalence or amplitude of tumour R_2^* spontaneous fluctuations were not affected by the drug. Similarly, the whole-tumour responsiveness to gas challenges did not improve. However, imatinib promoted increased heterogeneity in the R_2^* response to carbogen breathing, which draws attention to the importance of considering regional effects. A correlation between blood oxygenation (R_2^* estimates) and tissue oxygenation (R_1 estimates) was also attempted. However, no significant associations were observed, which could once again be due to measurement uncertainty,

particularly in R_1 estimates. Limitations include the short length of the study, the non-fractioned drug administration regime, and the uncertainty in measurement estimates.

Future steps to the work presented in Chapter 6 comprise alterations to the therapy regime, employment of alternative methods to estimate tumour tissue oxygenation, or the use of alternative therapies.

A longer lasting regime, possibly 9 or 10 days, in which lower doses of the drug are administered at more regular intervals, so as to allow continued exposure, would help to provide a more accurate estimate of the efficacy of imatinib. Examples of the advantages of a fractioned regime come from different studies [169;173]. This could offer a method to investigate 'windows' in which to apply secondary antitumour therapies.

R_1 estimates were found to be relatively insensitive to tissue oxygenation variations. Alternative methods to measure tissue pO_2 could thus be pursued. In particular, electron parametric resonance imaging (EPRI) looks very promising in providing non-invasive dynamic measurements of tumour pO_2 [12;86;206]. Together with a gradient-echo sequence, EPRI could be used to assess the relationship between variations in tumour pO_2 and R_2^*. In fact, EPRI has already revealed to be sensitive enough to distinguish between tumour regions of chronic and cycling hypoxia [12;86].

Alternative therapies could equally be used to promote vascular normalisation and assess its effect of spontaneous R_2^* fluctuations and gas challenge responsiveness. Inhibitors of a receptor of vascular endothelial growth factor (VEGF) or multi-tyrosine kinase inhibitors, such as sunitinib, have been shown to promote vascular normalisation [173;207]. Sunitinib, in particular, was also shown to suppress tumour pO_2 fluctuations during the vascular normalisation window [207].

Chapter 7 described a pilot clinical study where the feasibility of using spontaneous R_2^* fluctuations as a biomarker of prostate tumour was assessed. Healthy and tumour prostate regions did not reveal significant or discernible differences in the amplitude or frequency of fluctuations. Few acquisition time points and the fact that the prostate suffers from artifactual motion due to rectal peristalsis constitute limitations of this study.

A similar protocol could be applied to a cohort of patients with brain tumours, where motion and susceptibility artifacts should be less limiting. A faster acquisition rate or a

longer imaging protocol would allow more dynamic data points, which would be advantageous in identifying oscillatory patterns and noisy components.

References

1. Dye C, Boerma T, Evans D, Harries A, Lienhardt C, McManus J, Pang T, Terry R, Zachariah R. The world health report 2013: research for universal health coverage. 2013. World Health Organization.

2. Vaupel P, Mayer A. Hypoxia in cancer: significance and impact on clinical outcome. *Cancer Metastasis Rev* 2007; **26:** 225-39.

3. Heldin CH, Rubin K, Pietras K, Ostman A. High interstitial fluid pressure - an obstacle in cancer therapy. *Nat Rev Cancer* 2004; **4:** 806-13.

4. Carmeliet P, Jain RK. Angiogenesis in cancer and other diseases. *Nature* 2000; **407:** 249-57.

5. Hashizume H, Baluk P, Morikawa S *et al.* Openings between defective endothelial cells explain tumor vessel leakiness. *Am J Pathol* 2000; **156:** 1363-80.

6. Morikawa S, Baluk P, Kaidoh T, Haskell A, Jain RK, McDonald DM. Abnormalities in pericytes on blood vessels and endothelial sprouts in tumors. *Am J Pathol* 2002; **160:** 985-1000.

7. Reed RK, Berg A, Gjerde EA, Rubin K. Control of interstitial fluid pressure: role of beta1-integrins. *Semin Nephrol* 2001; **21:** 222-30.

8. Dewhirst MW. Concepts of oxygen transport at the microcirculatory level. *Semin Radiat Oncol* 1998; **8:** 143-50.

9. Dewhirst MW, Cao Y, Moeller B. Cycling hypoxia and free radicals regulate angiogenesis and radiotherapy response. *Nat Rev Cancer* 2008; **8:** 425-37.

10. Dewhirst MW. Relationships between Cycling Hypoxia, HIF-1, Angiogenesis and Oxidative Stress. *Radiat Res* 2009; **172:** 653-65.

11. Bayer C, Vaupel P. Acute versus chronic hypoxia in tumors: Controversial data concerning time frames and biological consequences. *Strahlenther Onkol* 2012; **188:** 616-27.

12. Matsumoto S, Yasui H, Mitchell JB, Krishna MC. Imaging cycling tumor hypoxia. *Cancer Res* 2010; **70:** 10019-23.

13. Kirkpatrick JP, Brizel DM, Dewhirst MW. A mathematical model of tumor oxygen and glucose mass transport and metabolism with complex reaction kinetics. *Radiat Res* 2003; **159:** 336-44.

14. Secomb TW, Hsu R, Ong ET, Gross JF, Dewhirst MW. Analysis of the effects of oxygen supply and demand on hypoxic fraction in tumors. *Acta Oncol* 1995; **34:** 313-6.

15. Secomb TW, Hsu R, Braun RD, Ross JR, Gross JF, Dewhirst MW. Theoretical simulation of oxygen transport to tumors by three-dimensional networks of microvessels. *Adv Exp Med Biol* 1998; **454:** 629-34.

16. Dewhirst MW, Secomb TW, Ong ET, Hsu R, Gross JF. Determination of local oxygen consumption rates in tumors. *Cancer Res* 1994; **54:** 3333-6.

17. Hockel M, Vaupel P. Tumor hypoxia: definitions and current clinical, biologic, and molecular aspects. *J Natl Cancer Inst* 2001; **93:** 266-76.

18. Vaupel P, Kallinowski F, Okunieff P. Blood flow, oxygen and nutrient supply, and metabolic microenvironment of human tumors: a review. *Cancer Res* 1989; **49:** 6449-65.

19. Thomlinson RH, Gray LH. The Histological Structure of Some Human Lung Cancers and the Possible Implications for Radiotherapy. *Br J Cancer* 1955; **9:** 539-49.

20. Dewhirst MW, Ong ET, Braun RD *et al.* Quantification of longitudinal tissue pO(2) gradients in window chamber tumours: impact on tumour hypoxia. *Br J Cancer* 1999; **79:** 1717-22.

21. Kavanagh BD, Coffey BE, Needham D, Hochmuth RM, Dewhirst MW. The effect of flunarizine on erythrocyte suspension viscosity under conditions of extreme hypoxia, low pH, and lactate treatment. *Br J Cancer* 1993; **67:** 734-41.

22. Vaupel P, Harrison L. Tumor hypoxia: causative factors, compensatory mechanisms, and cellular response. *Oncologist* 2004; **9 Suppl 5:** 4-9.

23. Dewhirst MW, Kimura H, Rehmus SWE *et al.* Microvascular studies on the origins of perfusion-limited hypoxia. *Br J Cancer* 1996; **74:** S247-S251.

24. Chaplin DJ, Olive PL, Durand RE. Intermittent Blood-Flow in A Murine Tumor - Radiobiological Effects. *Cancer Res* 1987; **47:** 597-601.

25. Kimura H, Braun RD, Ong ET *et al.* Fluctuations in red cell flux in tumor microvessels can lead to transient hypoxia and reoxygenation in tumor parenchyma. *Cancer Res* 1996; **56:** 5522-8.

26. Lanzen J, Braun RD, Klitzman B, Brizel D, Secomb TW, Dewhirst MW. Direct demonstration of instabilities in oxygen concentrations within the extravascular compartment of an experimental tumor. *Cancer Res* 2006; **66:** 2219-23.

27. Kiani MF, Pries AR, Hsu LL, Sarelius IH, Cokelet GR. Fluctuations in Microvascular Blood-Flow Parameters Caused by Hemodynamic Mechanisms. *Am J Physiol* 1994; **266:** H1822-H1828.

28. Schmid-Schonbein GW, Skalak R, Usami S, Chien S. Cell distribution in capillary networks. *Microvasc Res* 1980; **19:** 18-44.

29. Patan S, Munn LL, Jain RK. Intussusceptive microvascular growth in a human colon adenocarcinoma xenograft: A novel mechanism of tumor angiogenesis. *Microvasc Res* 1996; **51:** 260-72.

30. Boucher Y, Baxter LT, Jain RK. Interstitial pressure gradients in tissue-isolated and subcutaneous tumors: implications for therapy. *Cancer Res* 1990; **50:** 4478-84.

31. Mollica F, Jain RK, Netti PA. A model for temporal heterogeneities of tumor blood flow. *Microvasc Res* 2003; **65:** 56-60.

32. Griffon-Etienne G, Boucher Y, Brekken C, Suit HD, Jain RK. Taxane-induced apoptosis decompresses blood vessels and lowers interstitial fluid pressure in solid tumors: clinical implications. *Cancer Res* 1999; **59:** 3776-82.

33. Padera TP, Stoll BR, Tooredman JB, Capen D, di TE, Jain RK. Pathology: cancer cells compress intratumour vessels. *Nature* 2004; **427:** 695.

34. Baudelet C, Ansiaux R, Jordan BF, Havaux X, Macq B, Gallez B. Physiological noise in murine solid tumours using T2*-weighted gradient-echo imaging: a marker of tumour acute hypoxia? *Phys Med Biol* 2004; **49:** 3389-411.

35. Braun RD, Lanzen JL, Dewhirst MW. Fourier analysis of fluctuations of oxygen tension and blood flow in R3230Ac tumors and muscle in rats. *Am J Physiol Heart Circ Physiol* 1999; **277:** H551-H568.

36. Brown JM. Evidence for Acutely Hypoxic Cells in Mouse-Tumors, and A Possible Mechanism of Re-Oxygenation. *Br J Radiol* 1979; **52:** 650-6.

37. Chaplin DJ, Durand RE, Olive PL. Acute-Hypoxia in Tumors - Implications for Modifiers of Radiation Effects. *Int J Radiat Oncol Biol Phys* 1986; **12:** 1279-82.

38. Bennewith KL, Raleigh JA, Durand RE. Orally administered pimonidazole to label hypoxic tumor cells. *Cancer Res* 2002; **62:** 6827-30.

39. Bennewith KL, Durand RE. Quantifying transient hypoxia in human tumor xenografts by flow cytometry. *Cancer Res* 2004; **64:** 6183-9.

40. Cárdenas-Navia LI, Mace D, Richardson RA, Wilson DF, Shan S, Dewhirst MW. The pervasive presence of fluctuating oxygenation in tumors. *Cancer Res* 2008; **68:** 5812-9.

41. Baudelet C, Cron GO, Ansiaux R *et al.* The role of vessel maturation and vessel functionality in spontaneous fluctuations of T-2*-weighted GRE signal within tumors. *NMR Biomed* 2006; **19:** 69-76.

42. McKeown SR. Defining normoxia, physoxia and hypoxia in tumours-implications for treatment response. *Br J Radiol* 2014; **87:** 20130676.

43. Gray LH, Conger AD, Ebert M, Horsney S, Scott OCA. The concentration of oxygen dissolved in tissues at the time of irradiation as a factor in radiotherapy. *Br J Radiol* 1953; **26:** 638-48.

44. Overgaard J. Sensitization of hypoxic tumour cells - clinical experience. *Int J Radiat Biology* 1989; **56:** 801-11.

45. Arcos JC, Argus MF, Woo Y. Chemical induction of cancer: modulation and combination effects: an inventory of the many factors which influence carcinogenesis. *Birkhauser Boston* 1995, p. 491.

46. Halperin EC, Perez CA, Brady LW. Principles and practice of radiation oncology. *Lippincott Williams & Wilkins* 2008, p. 76.

47. Nias A. An introduction to radiobiology. Second edition edn. *John Wiley & Sons* 1998, pp. 55-62, 156-175.

48. Trowell OA. The effect of environmental factors on the radiosensitivity of lymph nodes cultured in vitro. *Br J Radiol* 1953; **26:** 302-9.

49. Baudelet C. and Gallez B. Current Issues in the Utility of Blood Oxygen Level Dependent MRI for the Assessment of Modulations in Tumour Oxygenation. *Curr Med Imaging Rev* 2005; **1:** 229-243.

50. Vaupel P, Thews O, Hoeckel M. Treatment resistance of solid tumors: role of hypoxia and anemia. *Med Oncol* 2001; **18:** 243-59.

51. Durand RE. Intermittent blood flow in solid tumours - an under-appreciated source of 'drug resistance'. *Cancer Metastasis Rev* 2001; **20:** 57-61.

52. Wilson WR, Hay MP. Targeting hypoxia in cancer therapy. *Nat Rev Cancer* 2011; **11:** 393-410.

53. Cuvier C, Jang A, Hill RP. Exposure to hypoxia, glucose starvation and acidosis: effect on invasive capacity of murine tumor cells and correlation with cathepsin (L + B) secretion. *Clin Exp Metastasis* 1997; **15:** 19-25.

54. De Jaeger K, Kavanagh MC, Hill RP. Relationship of hypoxia to metastatic ability in rodent tumours. *Br J Cancer* 2001; **84:** 1280-5.

55. Moon EJ, Brizel DM, Chi JTA, Dewhirst MW. The potential role of intrinsic hypoxia markers as prognostic variables in cancer. *Antioxid Redox Signal* 2007; **9:** 1237-94.

56. Talmadge JE. Clonal selection of metastasis within the life history of a tumor. *Cancer Res.* 2007; **67:** 11471-5.

57. Hockel M, Schlenger K, Hockel S, Vaupel P. Hypoxic cervical cancers with low apoptotic index are highly aggressive. *Cancer Res* 1999; **59:** 4525-8.

58. Weinmann M, Jendrossek V, Guner D, Goecke B, Belka C. Cyclic exposure to hypoxia and reoxygenation selects for tumor cells with defects in mitochondrial apoptotic pathways. *FASEB J.* 2004; **18:** 1906-8.

59. Ke Q, Costa M. Hypoxia-inducible factor-1 (HIF-1). *Mol Pharmacol* 2006; **70:** 1469-80.

60. Fukuda R, Hirota K, Fan F, Jung YD, Ellis LM, Semenza GL. Insulin-like growth factor 1 induces hypoxia-inducible factor 1-mediated vascular endothelial growth factor expression, which is dependent on MAP kinase and

phosphatidylinositol 3-kinase signaling in colon cancer cells. *J Biol Chem* 2002; **277:** 38205-11.

61. Semenza GL. Targeting HIF-1 for cancer therapy. *Nat Rev Cancer* 2003; **3:** 721-32.

62. Zhong H, De Marzo AM, Laughner E *et al*. Overexpression of hypoxia-inducible factor 1alpha in common human cancers and their metastases. *Cancer Res* 1999; **59:** 5830-5.

63. Durand RE, LePard NE. Contribution of transient blood flow to tumour hypoxia in mice. *Acta Oncol* 1995; **34:** 317-23.

64. Gulliksrud K, Vestvik IK, Galappathi K, Mathiesen B, Rofstad EK. Detection of different hypoxic cell subpopulations in human melanoma xenografts by pimonidazole immunohistochemistry. *Radiat Res* 2008; **170:** 638-50.

65. Rofstad EK, Maseide K. Radiobiological and immunohistochemical assessment of hypoxia in human melanoma xenografts: acute and chronic hypoxia in individual tumours. *Int J Radiat Biol* 1999; **75:** 1377-93.

66. Rofstad EK, Galappathi K, Mathiesen B, Ruud EBM. Fluctuating and diffusion-limited hypoxia in hypoxia-induced metastasis. *Clin Cancer Res* 2007; **13:** 1971-8.

67. Hsieh CH, Lee CH, Liang JA, Yu CY, Shyu WC. Cycling hypoxia increases U87 glioma cell radioresistance via ROS induced higher and long-term HIF-1 signal transduction activity. *Oncol Rep* 2010; **24:** 1629-36.

68. Hsieh CH, Wu CP, Lee HT, Liang JA, Yu CY, Lin YJ. NADPH oxidase subunit 4 mediates cycling hypoxia-promoted radiation resistance in glioblastoma multiforme. *Free Radic Biol Med* 2012; **53:** 649-58.

69. Martinive P, Defresne F, Bouzin C *et al.* Preconditioning of the tumor vasculature and tumor cells by intermittent hypoxia: implications for anticancer therapies. *Cancer Res* 2006; **66:** 11736-44.

70. Chou CW, Wang CC, Wu CP *et al.* Tumor cycling hypoxia induces chemoresistance in glioblastoma multiforme by upregulating the expression and function of ABCB1. *Neuro Oncol* 2012; **14:** 1227-38.

71. Cairns RA, Kalliomaki T, Hill RP. Acute (cyclic) hypoxia enhances spontaneous metastasis of KHT murine tumors. *Cancer Res* 2001; **61:** 8903-8.

72. Cairns RA, Hill RP. Acute hypoxia enhances spontaneous lymph node metastasis in an orthotopic murine model of human cervical carcinoma. *Cancer Res* 2004; **64:** 2054-61.

73. Tellier C, Desmet D, Petit L *et al.* Cycling hypoxia induces a specific amplified inflammatory phenotype in endothelial cells and enhances tumor-promoting inflammation in vivo. *Neoplasia* 2015; **17:** 66-78.

74. Pires IM, Bencokova Z, Milani M *et al.* Effects of acute versus chronic hypoxia on DNA damage responses and genomic instability. *Cancer Res* 2010; **70:** 925-35.

75. Aguilera A, Gomez-Gonzalez B. Genome instability: a mechanistic view of its causes and consequences. *Nat Rev Genet* 2008; **9:** 204-17.

76. Gatenby RA, Gillies RJ. Why do cancers have high aerobic glycolysis? *Nat Rev Cancer* 2004; **4:** 891-9.

77. Harris AL. Hypoxia--a key regulatory factor in tumour growth. *Nat Rev Cancer* 2002; **2:** 38-47.

78. Yasuda S, Fujii H, Nakahara T *et al.* 18F-FDG PET detection of colonic adenomas. *J Nucl Med* 2001; **42:** 989-92.

79. Younes M, Lechago LV, Lechago J. Overexpression of the human erythrocyte glucose transporter occurs as a late event in human colorectal carcinogenesis and is associated with an increased incidence of lymph node metastases. *Clin Cancer Res* 1996; **2:** 1151-4.

80. Brizel DM, Schroeder T, Scher RL *et al.* Elevated tumor lactate concentrations predict for an increased risk of metastases in head-and-neck cancer. *Int J Radiat Oncol Biol Phys* 2001; **51:** 349-53.

81. Walenta S, Wetterling M, Lehrke M *et al.* High lactate levels predict likelihood of metastases, tumor recurrence, and restricted patient survival in human cervical cancers. *Cancer Res* 2000; **60:** 916-21.

82. Chaplin DJ, Hill SA. Temporal heterogeneity in microregional erythrocyte flux in experimental solid tumours. *Br J Cancer* 1995; **71:** 1210-3.

83. Pigott KH, Hill SA, Chaplin DJ, Saunders MI. Microregional fluctuations in perfusion within human tumours detected using laser Doppler flowmetry. *Radiother Oncol* 1996; **40:** 45-50.

84. Cardenas-Navia LI, Yu D, Braun RD, Brizel DM, Secomb TW, Dewhirst MW. Tumor-dependent kinetics of partial pressure of oxygen fluctuations during air and oxygen breathing. *Cancer Res* 2004; **64:** 6010-7.

85. Skala MC, Fontanella A, Hendargo H, Dewhirst MW, Izatt JA. Combined hyperspectral and spectral domain optical coherence tomography microscope for noninvasive hemodynamic imaging. *Opt Lett* 2009; **34:** 289-91.

86. Yasui H, Matsumoto S, Devasahayam N *et al.* Low-field magnetic resonance imaging to visualize chronic and cycling hypoxia in tumor-bearing mice. *Cancer Res* 2010; **70:** 6427-36.

87. Magat J, Jordan BF, Cron GO, Gallez B. Noninvasive mapping of spontaneous fluctuations in tumor oxygenation using 19F MRI. *Med Phys* 2010; **37:** 5434-41.

88. Brurberg KG, Benjaminsen IC, Dorum LM, Rofstad EK. Fluctuations in tumor blood perfusion assessed by dynamic contrast-enhanced MRI. *Magn Reson Med* 2007; **58:** 473-81.

89. Palmer GM, Fontanella AN, Shan S *et al.* In vivo optical molecular imaging and analysis in mice using dorsal window chamber models applied to hypoxia, vasculature and fluorescent reporters. *Nat Protoc* 2011; **6:** 1355-66.

90. Brurberg KG, Gaustad JV, Mollatt CS, Rofstad EK. Temporal heterogeneity in blood supply in human tumor xenografts. *Neoplasia* 2008; **10:** 727-35.

91. Brurberg KG, Graff BA, Rofstad EK. Temporal heterogeneity in oxygen tension in human melanoma xenografts. *Br J Cancer* 2003; **89:** 350-6.

92. Brurberg KG, Graff BA, Olsen DR, Rofstad EK. Tumor-line specific pO(2) fluctuations in human melanoma xenografts. *Int J Radiat Oncol Biol Phys* 2004; **58:** 403-9.

93. Brurberg KG, Skogmo HK, Graff BA, Olsen DR, Rofstad EK. Fluctuations in pO2 in poorly and well-oxygenated spontaneous canine tumors before and during fractionated radiation therapy. *Radiother Oncol* 2005; **77:** 220-6.

94. Nehmeh SA, Lee NY, Schroder H *et al.* Reproducibility of intratumor distribution of (18)F-fluoromisonidazole in head and neck cancer. *Int J Radiat Oncol Biol Phys* 2008; **70:** 235-42.

95. Wang K, Yorke E, Nehmeh SA, Humm JL, Ling CC. Modeling acute and chronic hypoxia using serial images of 18F-FMISO PET. *Med Phys* 2009; **36:** 4400-8.

96. Monnich D, Troost EG, Kaanders JH, Oyen WJ, Alber M, Thorwarth D. Modelling and simulation of the influence of acute and chronic hypoxia on [18F]fluoromisonidazole PET imaging. *Phys Med Biol* 2012; **57:** 1675-84.

97. Thorwarth D, Eschmann SM, Scheiderbauer J, Paulsen F, Alber M. Kinetic analysis of dynamic 18F-fluoromisonidazole PET correlates with radiation treatment outcome in head-and-neck cancer. *BMC Cancer* 2005; **5:** 152.

98. Brown MA, Semelka RC. MRI basic principles and applications. Third edn. *John Wiley & Sons Inc.* 2003.

99. McRobbie DW, Moore EA, Graves MJ, Prince MR. MRI From Picture to Proton. *Cambridge University Press* 2007.

100. Stippich C. Clinical functional MRI - Presurgical functional neuroimaging. *Springer* 2007.

101. Ogawa S, Lee TM. Magnetic-Resonance-Imaging of Blood-Vessels at High Fields - Invivo and Invitro Measurements and Image Simulation. *Magn Reson Med* 1990; **16:** 9-18.

102. Ogawa S, Lee TM, Nayak AS, Glynn P. Oxygenation-Sensitive Contrast in Magnetic-Resonance Image of Rodent Brain at High Magnetic-Fields. *Magn Reson Med* 1990; **14:** 68-78.

103. Jordan BF, Crokart N, Baudelet C, Cron GO, Ansiaux R, Gallez B. Complex relationship between changes in oxygenation status and changes in R-2(*): The

case of insulin and NS-398, two inhibitors of oxygen consumption. *Magn Reson Med* 2006; **56:** 637-43.

104. Robinson SP, Rodrigues LM, Ojugo ASE, McSheehy PMJ, Howe FA, Griffiths JR. The response to carbogen breathing in experimental tumour models monitored by gradient-recalled echo magnetic resonance imaging. *Br J Cancer* 1997; **75:** 1000-6.

105. Tofts P. Quantitative MRI of the brain: measuring changes caused by disease. *John Wiley & Sons Inc.* 2003.

106. Brindle KM, Brown FF, Campbell ID, Grathwohl C, Kuchel PW. Application of spin-echo nuclear magnetic resonance to whole-cell systems. Membrane transport. *Biochem J* 1979; **180:** 37-44.

107. Dobre MC, Ugurbil K, Marjanska M. Determination of blood longitudinal relaxation time (T1) at high magnetic field strengths. *Magn Reson Imaging* 2007; **25:** 733-5.

108. Howe FA, Robinson SP, McIntyre DJ, Stubbs M, Griffiths JR. Issues in flow and oxygenation dependent contrast (FLOOD) imaging of tumours. *NMR Biomed* 2001; **14:** 497-506.

109. Baudelet C, Gallez B. How does blood oxygen level-dependent (BOLD) contrast correlate with oxygen partial pressure (pO2) inside tumors? *Magn Reson Med* 2002; **48:** 980-6.

110. Abramovitch R, Dafni H, Smouha E, Benjamin LE, Neeman M. In vivo prediction of vascular susceptibility to vascular endothelial growth factor withdrawal: Magnetic resonance imaging of C6 rat glioma in nude mice. *Cancer Res* 1999; **59:** 5012-6.

111. Burrell JS, Walker-Samuel S, Baker LC *et al.* Investigating temporal fluctuations in tumor vasculature with combined carbogen and ultrasmall superparamagnetic iron oxide particle (CUSPIO) imaging. *Magn Reson Med* 2011; **66:** 227-34.

112. Griffiths JR, Taylor NJ, Howe FA *et al.* The response of human tumors to carbogen breathing, monitored by Gradient-Recalled Echo Magnetic Resonance Imaging. *Int J Radiat Oncol Biol Phys* 1997; **39:** 697-701.

113. Robinson SP, Howe FA, Griffiths JR. Noninvasive monitoring of carbogen-induced changes in tumor blood flow and oxygenation by functional magnetic resonance imaging. *Int J Radiat Oncol Biol Phys* 1995; **33:** 855-9.

114. Nielsen T, Nielsen NC, Holm TH, Ostergaard L, Horsman MR, Busk M. Ultra-high field 1H magnetic resonance imaging approaches for acute hypoxia. *Acta Oncol* 2013; **52:** 1287-92.

115. Thomas CD, Stern S, Chaplin DJ, Guichard M. Transient perfusion and radiosensitizing effect after nicotinamide, carbogen, and perflubron emulsion administration. *Radiother Oncol* 1996; **39:** 235-41.

116. Workman P, Aboagye EO, Balkwill F *et al.* Guidelines for the welfare and use of animals in cancer research. *Br J Cancer* 2010; **102:** 1555-77.

117. El-Emir E, Boxer GM, Petrie IA *et al.* Tumour parameters affected by combretastatin A-4 phosphate therapy in a human colorectal xenograft model in nude mice. *Eur J Cancer* 2005; **41:** 799-806.

118. El-Emir E, Qureshi U, Dearling JL *et al.* Predicting response to radioimmunotherapy from the tumor microenvironment of colorectal carcinomas. *Cancer Res* 2007; **67:** 11896-905.

119. Folarin AA, Konerding MA, Timonen J, Nagl S, Pedley RB. Three-dimensional analysis of tumour vascular corrosion casts using stereoimaging and micro-computed tomography. *Microvasc Res* 2010; **80:** 89-98.

120. Pedley RB, El-Emir E, Flynn AA *et al.* Synergy between vascular targeting agents and antibody-directed therapy. *Int J Radiat Oncol Biol Phys* 2002; **54:** 1524-31.

121. Landuyt W, Sunaert S, Farina D *et al.* In vivo animal functional MRI: improved image quality with a body-adapted mold. *J Magn Reson Imaging* 2002; **16:** 224-7.

122. Zang YF, He Y, Zhu CZ *et al.* Altered baseline brain activity in children with ADHD revealed by resting-state functional MRI. *Brain Dev* 2007; **29:** 83-91.

123. Zou QH, Zhu CZ, Yang Y *et al.* An improved approach to detection of amplitude of low-frequency fluctuation (ALFF) for resting-state fMRI: fractional ALFF. *J Neurosci Methods* 2008; **172:** 137-41.

124. Walker-Samuel S, Orton M, McPhail LD *et al.* Bayesian estimation of changes in transverse relaxation rates. *Magn Reson Med* 2010; **64:** 914-21.

125. Ashburner J, Friston K, Penny W. Human Brain function, Part Two. Second edn. *Elsevier Science* 2004.

126. Worsley KJ, Evans AC, Marrett S, Neelin P. A three-dimensional statistical analysis for CBF activation studies in human brain. *J Cereb Blood Flow Metab* 1992; **12:** 900-18.

127. Glantz SA. Primer of Biostatistics. *McGraw-Hill* 2012.

128. Press WH, Teukolsky SA, Vetterling WT, Flannery BP. Numerical recipes: the art of scientific computing - third edition. *Cambridge University Press* 2007; pp. 685-689.

129. Scargle JD. Studies in astronomical time series analysis. II. Statistical aspects of spectral analysis of unevenly spaced data. *Astrophys J* 1982; **263:** 835-53.

130. Bohr C, Hasselbalch K, Krogh A. Concerning a biologically important relationship - The influence of the carbon dioxide content of blood on its oxygen binding. *Skand Arch Physiol* 1904; **16:** 401-12.

131. Baudelet C, Cron GO, Gallez B. Determination of the maturity and functionality of tumor vasculature by MRI: correlation between BOLD-MRI and DCE-MRI using P792 in experimental fibrosarcoma tumors. *Magn Reson Med* 2006; **56:** 1041-9.

132. Gilad AA, Israely T, Dafni H, Meir G, Cohen B, Neeman M. Functional and molecular mapping of uncoupling between vascular permeability and loss of vascular maturation in ovarian carcinoma xenografts: the role of stroma cells in tumor angiogenesis. *Int J Cancer* 2005; **117:** 202-11.

133. Gilead A, Meir G, Neeman M. The role of angiogenesis, vascular maturation, regression and stroma infiltration in dormancy and growth of implanted MLS ovarian carcinoma spheroids. *Int J Cancer* 2004; **108:** 524-31.

134. Neeman M, Dafni H, Bukhari O, Braun RD, Dewhirst MW. In vivo BOLD contrast MRI mapping of subcutaneous vascular function and maturation: validation by intravital microscopy. *Magn Reson Med* 2001; **45:** 887-98.

135. Robinson SP, Collingridge DR, Howe FA, Rodrigues LM, Chaplin DJ, Griffiths JR. Tumour response to hypercapnia and hyperoxia monitored by FLOOD magnetic resonance imaging. *NMR Biomed* 1999; **12:** 98-106.

136. Robinson SP, Rijken PF, Howe FA *et al.* Tumor vascular architecture and function evaluated by non-invasive susceptibility MRI methods and immunohistochemistry. *J Magn Reson Imaging* 2003; **17:** 445-54.

137. Abramovitch R, Itzik A, Harel H, Nagler A, Vlodavsky I, Siegal T. Halofuginone inhibits angiogenesis and growth in implanted metastatic rat brain tumor model--an MRI study. *Neoplasia* 2004; **6:** 480-9.

138. Rodrigues LM, Maxwell RJ, McSheehy PM *et al.* In vivo detection of ifosfamide by 31P-MRS in rat tumours: increased uptake and cytotoxicity induced by carbogen breathing in GH3 prolactinomas. *Br J Cancer* 1997; **75:** 62-8.

139. Rodrigues LM, Howe FA, Griffiths JR, Robinson SP. Tumor R2* is a prognostic indicator of acute radiotherapeutic response in rodent tumors. *J Magn Reson Imaging* 2004; **19:** 482-8.

140. Al-Hallaq HA, River JN, Zamora M, Oikawa H, Karczmar GS. Correlation of magnetic resonance and oxygen microelectrode measurements of carbogen-induced changes in tumor oxygenation. *Int J Radiat Oncol Biol Phys* 1998; **41:** 151-9.

141. Karczmar GS, Kuperman VY, Lewis MZ, River JN Lubich L, and Halpern H. Inhalation of 100% Oxygen may decrease oxygenation in some tumour regions; magnetic resonance evidence for an intratumoral steal effect. *Proc Soc Magn Reson* 3. 1995.

142. Karczmar GS, River JN, Li J, Vijayakumar S, Goldman Z, Lewis MZ. Effects of hyperoxia on T2* and resonance frequency weighted magnetic resonance images of rodent tumours. *NMR Biomed* 1994; **7:** 3-11.

143. Hanahan D, Folkman J. Patterns and emerging mechanisms of the angiogenic switch during tumorigenesis. *Cell* 1996; **86:** 353-64.

144. Weissleder R, Ross B, Rehemtulla A, Gambhir S. Molecular imaging: principles and practice. *People's Medical Publishing House* 2010.

145. Goncalves MR, Johnson SP, Ramasawmy R, Pedley RB, Lythgoe MF, Walker-Samuel S. Decomposition of spontaneous fluctuations in tumour oxygenation using BOLD MRI and independent component analysis. *Br J Cancer* 2015; **113:** 1168-77.

146. Beckmann CF, DeLuca M, Devlin JT, Smith SM. Investigations into resting-state connectivity using independent component analysis. *Philos Trans R Soc Lond B Biol Sci* 2005; **360:** 1001-13.

147. Kundu P, Brenowitz ND, Voon V *et al.* Integrated strategy for improving functional connectivity mapping using multiecho fMRI. *Proc Natl Acad Sci USA* 2013; **110:** 16187-92.

148. van de Ven VG, Formisano E, Prvulovic D, Roeder CH, Linden DEJ. Functional connectivity as revealed by spatial independent component analysis of fMRI measurements during rest. *Hum Brain Mapp* 2004; **22:** 165-78.

149. Shlens J. A tutorial on principal component analysis. Cornell University Library. 2014. [Online]. Available: http://arxiv.org/pdf/1404.1100v1.pdf. Accessed 4 Mar 2015.

150. Hyvarinen A. Fast and robust fixed-point algorithms for independent component analysis. *IEEE Trans Neural Netw* 1999; **10:** 626-34.

151. Murakami M. Signaling required for blood vessel maintenance: molecular basis and pathological manifestations. *Int J Vasc Med* 2012; **2012:** 293641.

152. Ellingsen C, Ovrebo KM, Galappathi K, Mathiesen B, Rofstad EK. pO(2) fluctuation pattern and cycling hypoxia in human cervical carcinoma and melanoma xenografts. *Int J Radiat Oncol Biol Phys* 2012; **83:** 1317-23.

153. Druker BJ, Lydon NB. Lessons learned from the development of an abl tyrosine kinase inhibitor for chronic myelogenous leukemia. *J Clin Invest* 2000; **105:** 3-7.

154. De GU, Verweij J. Imatinib and gastrointestinal stromal tumors: Where do we go from here? *Mol Cancer Ther* 2005; **4:** 495-501.

155. Demetri GD, von MM, Blanke CD *et al.* Efficacy and safety of imatinib mesylate in advanced gastrointestinal stromal tumors. *N Engl J Med* 2002; **347:** 472-80.

156. Nilsson B, Sjolund K, Kindblom LG *et al.* Adjuvant imatinib treatment improves recurrence-free survival in patients with high-risk gastrointestinal stromal tumours (GIST). *Br J Cancer* 2007; **96:** 1656-8.

157. FDA Highlights and Prescribing Information for Gleevec (imatinib mesylate). 2001. [Online]. Available:

http://www.accessdata.fda.gov/drugsatfda_docs/label/2008/021588s024lbl.pdf. Accessed 4 Apr 2015.

158. FDA approves Gleevec for children with acute lymphoblastic leukemia. 2013. [Online]. Available: http://www.fda.gov/NewsEvents/Newsroom/PressAnnouncements/ucm336868.htm. Accessed 4 Apr 2015.

159. Buchdunger E, Cioffi CL, Law N *et al.* Abl protein-tyrosine kinase inhibitor STI571 inhibits in vitro signal transduction mediated by c-kit and platelet-derived growth factor receptors. *J Pharmacol Exp Ther* 2000; **295:** 139-45.

160. Buchdunger E, O'Reilly T, Wood J. Pharmacology of imatinib (STI571). *Eur J Cancer* 2002; **38 Suppl 5:** S28-S36.

161. Battegay EJ, Rupp J, Iruela-Arispe L, Sage EH, Pech M. PDGF-BB modulates endothelial proliferation and angiogenesis in vitro via PDGF beta-receptors. *J Cell Biol* 1994; **125:** 917-28.

162. Nissen LJ, Cao R, Hedlund EM *et al.* Angiogenic factors FGF2 and PDGF-BB synergistically promote murine tumor neovascularization and metastasis. *J Clin Invest* 2007; **117:** 2766-77.

163. Sato N, Beitz JG, Kato J *et al.* Platelet-derived growth factor indirectly stimulates angiogenesis in vitro. *Am J Pathol* 1993; **142:** 1119-30.

164. Xue Y, Lim S, Yang Y *et al.* PDGF-BB modulates hematopoiesis and tumor angiogenesis by inducing erythropoietin production in stromal cells. *Nat Med* 2012; **18:** 100-10.

165. Rajkumar VS, Boxer G, Robson M, Muddle J, Papastavrou Y, Pedley RB. A comparative study of PDGFR inhibition with imatinib on radiolabeled antibody targeting and clearance in two pathologically distinct models of colon adenocarcinoma. *Tumour Biol* 2012; **33:** 2019-29.

166. Vlahovic G, Rabbani ZN, Herndon JE, Dewhirst MW, Vujaskovic Z. Treatment with Imatinib in NSCLC is associated with decrease of phosphorylated PDGFR-beta and VEGF expression, decrease in interstitial fluid pressure and improvement of oxygenation. *Br J Cancer* 2006; **95:** 1013-9.

167. Vlahovic G, Ponce AM, Rabbani Z *et al.* Treatment with imatinib improves drug delivery and efficacy in NSCLC xenografts. *Br J Cancer* 2007; **97:** 735-40.

168. Yener U, Avsar T, Akgun E, Seker A, Bayri Y, Kilic T. Assessment of antiangiogenic effect of imatinib mesylate on vestibular schwannoma tumors using in vivo corneal angiogenesis assay. *J Neurosurg* 2012; **117:** 697-704.

169. Baranowska-Kortylewicz J, Abe M, Pietras K *et al.* Effect of platelet-derived growth factor receptor-beta inhibition with STI571 on radioimmunotherapy. *Cancer Res* 2005; **65:** 7824-31.

170. Jain RK. Normalizing tumor vasculature with anti-angiogenic therapy: a new paradigm for combination therapy. *Nat Med* 2001; **7:** 987-9.

171. Le Serve AW, Hellmann K. Metastases and the normalization of tumour blood vessels by ICRF 159: a new type of drug action. *Br Med J* 1972; **1:** 597-601.

172. Dickson PV, Hamner JB, Sims TL *et al.* Bevacizumab-induced transient remodeling of the vasculature in neuroblastoma xenografts results in improved delivery and efficacy of systemically administered chemotherapy. *Clin Cancer Res* 2007; **13:** 3942-50.

173. Huang Y, Yuan J, Righi E *et al.* Vascular normalizing doses of antiangiogenic treatment reprogram the immunosuppressive tumor microenvironment and enhance immunotherapy. *Proc Natl Acad Sci USA* 2012; **109:** 17561-6.

174. Juan TY, Roffler SR, Hou HS *et al.* Antiangiogenesis targeting tumor microenvironment synergizes glucuronide prodrug antitumor activity. *Clin Cancer Res* 2009; **15:** 4600-11.

175. Tong RT, Boucher Y, Kozin SV, Winkler F, Hicklin DJ, Jain RK. Vascular normalization by vascular endothelial growth factor receptor 2 blockade induces a pressure gradient across the vasculature and improves drug penetration in tumors. *Cancer Res* 2004; **64:** 3731-6.

176. Wildiers H, Guetens G, De BG *et al.* Effect of antivascular endothelial growth factor treatment on the intratumoral uptake of CPT-11. *Br J Cancer* 2003; **88:** 1979-86.

177. Inai T, Mancuso M, Hashizume H *et al.* Inhibition of vascular endothelial growth factor (VEGF) signaling in cancer causes loss of endothelial fenestrations, regression of tumor vessels, and appearance of basement membrane ghosts. *Am J Pathol* 2004; **165:** 35-52.

178. Cooke VG, LeBleu VS, Keskin D *et al.* Pericyte depletion results in hypoxia-associated epithelial-to-mesenchymal transition and metastasis mediated by met signaling pathway. *Cancer Cell* 2012; **21:** 66-81.

179. Pietras K, Pahler J, Bergers G, Hanahan D. Functions of paracrine PDGF signaling in the proangiogenic tumor stroma revealed by pharmacological targeting. *PLoS Med* 2008; **5:** e19.

180. Carmeliet P, Jain RK. Molecular mechanisms and clinical applications of angiogenesis. *Nature* 2011; **473:** 298-307.

181. Hellberg C, Ostman A, Heldin CH. PDGF and vessel maturation. *Recent Results Cancer Res* 2010; **180:** 103-14.

182. Pietras K, Rubin K, Sjoblom T *et al.* Inhibition of PDGF receptor signaling in tumor stroma enhances antitumor effect of chemotherapy. *Cancer Res* 2002; **62:** 5476-84.

183. Pietras K, Stumm M, Hubert M *et al.* STI571 enhances the therapeutic index of epothilone B by a tumor-selective increase of drug uptake. *Clin Cancer Res* 2003; **9:** 3779-87.

184. Manning WJ, Pennell DJ. Cardiovascular Magnetic Resonance, second edition. *Saunders Elsevier* 2010, pp. 81-83.

185. Hall AP. Review of the pericyte during angiogenesis and its role in cancer and diabetic retinopathy. *Toxicol Pathol* 2006; **34:** 763-75.

186. Murfee WL, Skalak TC, Peirce SM. Differential arterial/venous expression of NG2 proteoglycan in perivascular cells along microvessels: identifying a venule-specific phenotype. *Microcirculation* 2005; **12:** 151-60.

187. Song S, Ewald AJ, Stallcup W, Werb Z, Bergers G. PDGFRbeta+ perivascular progenitor cells in tumours regulate pericyte differentiation and vascular survival. *Nat Cell Biol* 2005; **7:** 870-9.

188. le Coutre P, Mologni L, Cleris L *et al.* In vivo eradication of human BCR/ABL-positive leukemia cells with an ABL kinase inhibitor. *J Natl Cancer Inst* 1999; **91:** 163-8.

189. Gaengel K, Genove G, Armulik A, Betsholtz C. Endothelial-mural cell signaling in vascular development and angiogenesis. *Arterioscler Thromb Vasc Biol* 2009; **29:** 630-8.

190. Pietras K, Ostman A, Sjoquist M *et al.* Inhibition of platelet-derived growth factor receptors reduces interstitial hypertension and increases transcapillary transport in tumors. *Cancer Res* 2001; **61:** 2929-34.

191. Weiss A, van Beijnum JR, Bonvin D *et al.* Low-dose angiostatic tyrosine kinase inhibitors improve photodynamic therapy for cancer: lack of vascular normalization. *J Cell Mol Med* 2014; **18:** 480-91.

192. Popow-Wozniak A, Wozniakowska A, Kaczmarek L, Malicka-Blaszkiewicz M, Nowak D. Apoptotic effect of imatinib on human colon adenocarcinoma cells: influence on actin cytoskeleton organization and cell migration. *Eur J Pharmacol* 2011; **667:** 66-73.

193. Lahm H, Amstad P, Yilmaz A *et al.* Interleukin 4 down-regulates expression of c-kit and autocrine stem cell factor in human colorectal carcinoma cells. *Cell Growth Differ* 1995; **6:** 1111-8.

194. Goel S, Wong AH, Jain RK. Vascular normalization as a therapeutic strategy for malignant and nonmalignant disease. *Cold Spring Harb Perspect Med* 2012; **2:** a006486.

195. O'Connor JP, Naish JH, Jackson A *et al.* Comparison of normal tissue R1 and R*2 modulation by oxygen and carbogen. *Magn Reson Med* 2009; **61:** 75-83.

196. Prostate cancer key stats - Cancer Research UK. 2014. [Online]. Available: http://publications.cancerresearchuk.org/downloads/Product/CS_KF_PROSTATE.pdf

197. Puech P, Sufana IA, Renard B, Villers A, Lemaitre L. Detecting prostate cancer with MRI - why and how. *Diagn Interv Imaging* 2012; **93:** 268-78.

198. Carter HB, DeMarzo A, Lilja H. Report to the Nation on Prostate Cancer 2004 - Capter 1: Detection, Diagnosis and Prognosis of Prostate Cancer, Medscape CME. 2004.

199. Pondman KM, Futterer JJ, ten HB *et al.* MR-guided biopsy of the prostate: an overview of techniques and a systematic review. *Eur Urol* 2008; **54:** 517-27.

200. Verma S, Turkbey B, Muradyan N *et al.* Overview of dynamic contrast-enhanced MRI in prostate cancer diagnosis and management. *AJR Am J Roentgenol* 2012; **198:** 1277-88.

201. Ramasawmy R, Campbell-Washburn AE, Wells JA *et al.* Hepatic arterial spin labelling MRI: an initial evaluation in mice. *NMR Biomed* 2015; **28:** 272-80.

202. Walker-Samuel S, Ramasawmy R, Torrealdea F *et al.* In vivo imaging of glucose uptake and metabolism in tumors. *Nat Med* 2013; **19:** 1067-72.

203. Horska A, Barker PB. Imaging of brain tumors: MR spectroscopy and metabolic imaging. *Neuroimaging Clin N Am* 2010; **20:** 293-310.

204. Day SE, Kettunen MI, Gallagher FA *et al.* Detecting tumor response to treatment using hyperpolarized 13C magnetic resonance imaging and spectroscopy. *Nat Med* 2007; **13:** 1382-7.

205. Vakoc BJ, Lanning RM, Tyrrell JA *et al.* Three-dimensional microscopy of the tumor microenvironment in vivo using optical frequency domain imaging. *Nat Med* 2009; **15:** 1219-23.

206. Matsumoto S, Hyodo F, Subramanian S *et al.* Low-field paramagnetic resonance imaging of tumor oxygenation and glycolytic activity in mice. *J Clin Invest* 2008; **118:** 1965-73.

207. Matsumoto S, Batra S, Saito K *et al.* Antiangiogenic agent sunitinib transiently increases tumor oxygenation and suppresses cycling hypoxia. *Cancer Res* 2011; **71:** 6350-9.

Supplementary data

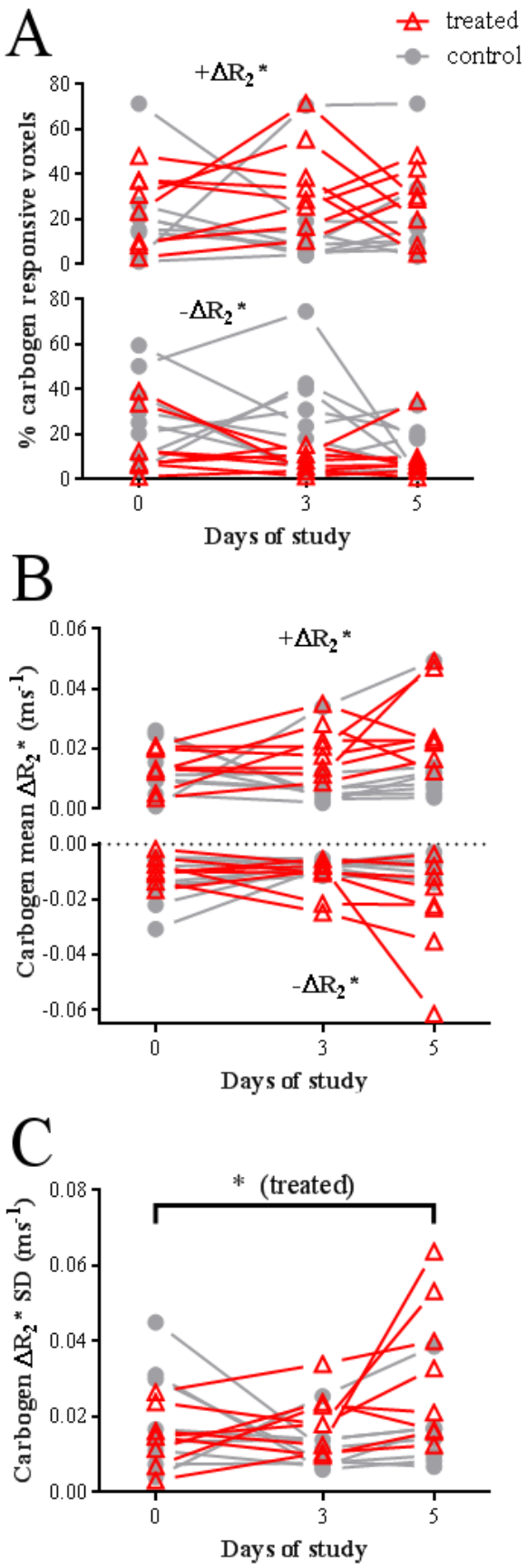

Figure S6.4 – Treated (imatinib) and control (saline) tumour response to carbogen at days 0 (baseline), 3 and 5. Significance between days of study was tested with a one-way ANOVA followed by Holm-Šídák's multiple comparisons test. **A:** Percentage of tumour voxels showing a positive ($+\Delta R_2^*$) or negative ($-\Delta R_2^*$) response to carbogen. **B:** Corresponding mean ΔR_2^* values for each treated or control tumour. **C:** Standard deviation of the magnitude values represented in **B**, depicting a significant increase in the heterogeneity of the carbogen response between days 0 and 5 in the treated group, but not in the control group.

Table S7.1 – Age, PSA level and biopsy results for the cohort of patients.

Patient #	Age	PSA (ng/ml)	Prostate biopsy	
			Site	Gleason score
1	66	5.26	left mid anterior base	3+3
2	60	2.00	mid apex	3+3
			right medial anterior apex	3+3
			left lateral	3+3
			right lateral	3+3
			right para posterior apex	3+3
			right medial posterior apex	3+3
3	58	1.40	left para anterior apex	3+3
			right medial anterior base	3+3
4	74	9.30	left medial posterior apex	3+3
6	65	6.60	left parasagittal anterior apex	3+4
			left parasagittal anterior base	3+4
			right parasagittal anterior apex	3+3
			right medial anterior apex	3+3
			right lateral	3+3
			right parasagittal posterior apex	3+3
			right medial posterior apex	3+3
			right medial posterior base	3+3
7	73	12.10	No tumour	
8	63	11.00	left para anterior apex	3+3
			right para anterior apex	3+3
			mid base	3+3
			left lateral	3+3
			right lateral	3+3
			left para posterior apex	3+3
			left medial posterior apex	3+3
			left medial posterior base	3+3
			right medial posterior base	3+3
9	79	11.80	left para anterior apex	3+3
			mid apex	3+3
			left mid anterior apex	3+3
			right lateral	4+3
			right para posterior apex	3+3
			right medial posterior apex	4+3
			right medial posterior base	3+3
10	71	5.54	left para anterior apex	3+3
			left medial anterior apex	3+4
			left medial anterior base	3+4
			right medial anterior apex	3+4

			right medial anterior base	3+4
			left para posterior base	3+3
			left para posterior base	3+3
11	67	15.00 & 11.00	left para anterior apex	3+3
			left medial anterior base	3+3
			right para anterior base	3+4
			right para anterior apex	3+3
			left mid anterior apex	3+3
			right medial anterior base	3+4
			right medial anterior apex	3+3
			right medial posterior base	3+4
12	63	6.92	left para anterior base	3+3
			mid apex	3+4
			mid base	3+4
			left mid anterior apex	3+4
			left mid anterior base	3+4
			left lateral	3+3
			left para posterior apex	3+4
			left para posterior base	3+4
			right para posterior apex	3+4
			right para posterior apex	3+4
			right para posterior base	3+3
			left medial posterior base	3+4
13	68	11.35	left para anterior base	3+3
			right para anterior apex	3+3
			right para anterior base	3+3
			left medial anterior base	3+3
			right medial anterior apex	3+3
			right medial anterior base	3+4
			left lateral	3+3
			right lateral	3+4
			left para posterior apex	3+3
			right para posterior apex	3+3
			left medial posterior apex	3+4
			left medial posterior base	3+3
			right medial posterior base	3+3
14	59	3.68	left mid anterior apex	3+3
			left para posterior apex	3+4
			left medial posterior apex	3+4
15	70	4.21	No tumour	
16	61	4.06	No tumour	
17	63	3.80	left mid anterior apex	3+3
			right medial anterior apex	3+3
			left lateral	3+3
			left para posterior apex	3+3
			right para posterior apex	3+3

			left medial posterior apex	3+4
19	68	3.90	right para anterior base	3+3
			left lateral	3+4
			left medial posterior apex	3+4
			right medial posterior apex	3+4
20	60	4.74	No tumour	
21	69	10.32	mid apex	3+4
			right lateral	3+4
			right medial posterior apex	3+4
			right medial posterior base	3+4
22	60	9.66	left para anterior apex	3+3
			left mid anterior apex	3+4
			left lateral	4+3
			left medial posterior apex	3+3